

This dissertation has been  
microfilmed exactly as received 68-15,604

BURCH, James Leo, 1942-  
HIGH-LATITUDE SATELLITE OBSERVATIONS OF  
ELECTRONS AND PROTONS AT 4000 KM.

Rice University, Ph.D., 1968  
Physics, general

University Microfilms, Inc., Ann Arbor, Michigan

RICE UNIVERSITY

HIGH-LATITUDE SATELLITE OBSERVATIONS OF ELECTRONS

AND PROTONS AT 4000 KM

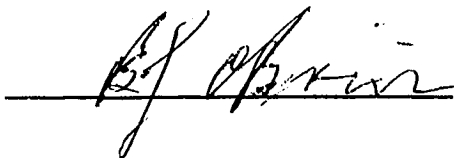
by

JAMES LEO BURCH

A THESIS SUBMITTED  
IN PARTIAL FULFILLMENT OF THE  
REQUIREMENTS FOR THE DEGREE OF

DOCTOR OF PHILOSOPHY

Thesis Director's Signature:



Houston, Texas

May, 1968

## TABLE OF CONTENTS

	PAGE
I. INTRODUCTION.....	1
A. Geophysical Significance of Polar Regions.....	1
B. Effects of Solar Wind - Magnetosphere Inter- action on the High-Latitude Magnetic Field Configuration.....	3
C. Charged Particle and Magnetic Field Measure- ments in the Geomagnetic Tail.....	9
D. Measurements of High-Latitude Charged Parti- cles at Low Altitudes.....	12
E. Summary of the Principal Results of This Experiment.....	25
II. DESCRIPTION OF THE EXPERIMENT.....	28
A. Satellite Description.....	28
B. Telemetry.....	30
C. Magnetic Orientation.....	31
D. The SPECS Charged Particle Detector .....	37
1. Channel Multiplier Characteristics.....	38
2. Physical Analyzer and Associated Electronics.....	50
3. SPECS Calibration.....	52
III. EXPERIMENTAL RESULTS.....	66
A. Satellite Performance.....	66
B. Data Acquisition and Reduction.....	67

	PAGE
C. Typical Characteristics of Electrons Observed at High Latitudes.....	69
1. Response of Channel 6 in the Polar Regions.....	69
2. Diurnal Variation of Northern Hemisphere Particle Fluxes.....	72
3. Dependence of Northern Hemisphere Particle Fluxes on Magnetic Activity.....	74
4. Spectral Characteristics of Precipitated Electrons in the Polar Regions.....	75
5. Spectral Characteristics of Precipitated Protons in the Night-Side Polar Regions...	78
6. Poleward Movement of Auroral Electron and Proton Precipitation During an Auroral Zone Bay Disturbance.....	80
7. Discussion of Possible Errors Due to Channel Multiplier Efficiency Measurements.....	83
IV. DISCUSSION.....	84
A. Relationship of Aurora 1 Data to Previous High-Latitude Charged Particle Measurements at Low Altitudes.....	84
B. Relationship of the Various Particle Domains to the Magnetosphere and to Auroral Phenomena.	93
C. Neutral Sheet Instability as a Possible Cause of the Expansive Phase of the Auroral Substorm.....	105
D. Summary and Conclusions.....	117

	PAGE
APPENDIX I.....	123
APPENDIX II.....	125
BIBLIOGRAPHY.....	129
FIGURE CAPTIONS.....	141
FIGURES.....	148

## I. INTRODUCTION

A knowledge of the high-latitude charged particle population that is as accurate and comprehensive as possible is necessary for a proper assessment of auroral and related magnetospheric phenomena. The purpose of this thesis is to present and discuss electron and proton measurements in the energy range  $50 \text{ ev} \leq E \leq 100 \text{ kev}$ , made at high latitudes and at an altitude of 4000 km aboard the polar-orbiting satellite Aurora 1. These measurements have added to our knowledge of the dependence of the intensities and spectra of these particles on latitude, local time, and polar and worldwide magnetic activity.

In this section, we will discuss some basic features of what is presently known theoretically and experimentally about the solar wind - magnetosphere interaction and the resulting high-latitude charged particle effects in order to lay a foundation for discussion of the Aurora 1 measurements.

### A. Geophysical Significance of the Polar Regions.

Some of the most spectacular but least understood of geophysical phenomena occur in that region permeated by geomagnetic lines of force which intersect the earth's surface at magnetic latitudes greater than  $60^\circ$ . This region, which maps geomagnetically into the auroral zones and polar caps, must be understood if the myriad polar phenomena such as the aurora, polar magnetic disturbances, and the related ionospheric and magnetospheric currents and

electric fields are to be organized into anything more than a morphological catalog of related fact. Ground-based observations, many of which were performed long before the complex interaction with the solar corona was even suspected, provide valuable points of departure for attempts at a self-consistent model. These observations have been reviewed extensively (Chamberlain, 1961; Davis, 1965; O'Brien, 1965). Two of the most important of these are: (1) The aurora statistically occurs in belts around the north and south geomagnetic poles, and (2) Auroral activity increases sharply one to two days following a period of intense solar activity, indicating some coupling mechanism other than purely electromagnetic waves.

Subsequent sounding rocket measurements demonstrated a simultaneity of auroral light and the precipitation of electrons of 5 to 10 kev energy (Davis et al., 1960; McIlwain, 1960); a definite relationship between the high-latitude boundary of trapping of electrons ( $\geq 40$  kev) and the onset of auroral activity as deduced from the 3914 Å nitrogen emission (O'Brien, 1964); and the existence of the solar corona at the earth's orbit (Gringauz, 1959). It is still not known if the boundary of trapping of electrons of energy greater than 40 kev delineates the auroral oval, that is, if particles can be stably trapped on "auroral" magnetic field lines, or indeed if these field lines are connected at all to the conjugate auroral zone. However, it is clear that whatever the actual configuration, its chief determining factor is the interaction between the expanding solar corona and the geomagnetic field. In the following section

we will discuss the extent to which the high-latitude magnetic field configuration can be determined by a simple model of this interaction.

B. Effects of the Solar Wind - Magnetosphere Interaction on the High-Latitude Magnetic Field Configuration.

The effect of a stream of solar ions and electrons on the geomagnetic field was calculated by Chapman and Ferraro, 1931, to explain the initial phase of magnetic storms in terms of an interaction with a burst of plasma "occasionally" emitted by the sun. Plasma detectors and magnetometers aboard the spacecraft Lunik 1, Explorer 10, Mariner 2, and IMP 1 among others have since verified that such a stream exists continuously and furthermore that the effect on the leading edge of the geomagnetic obstacle is essentially as estimated by Chapman and Ferraro. However, the perturbation felt by the solar wind itself as a result of the encounter as well as the configuration of the magnetospheric cavity downstream of the earth are to a large extent unexplained.

Owing to solar rotation, the plasma emitted radially by the sun traces out an Archimedes spiral in interplanetary space (see Chapman and Bartels, 1940). The flow is oriented approximately in the ecliptic plane and at 1 A. U. is inclined to the earth-sun line at an angle that depends on the solar wind velocity, but is about  $45^{\circ}$ . The hot ( $\sim 10^6$  K) corona, expanding in the presence of solar gravity, reaches a velocity which is supersonic as well as



superalfvenic (see Dessler, 1967). That is, the particle streaming velocity is greater than the propagation velocity of sound waves and hydromagnetic waves in the solar plasma. It has been noted that at middle solar latitudes the surface magnetic field is chiefly that due to sunspots, that is, with lines of force directed either radially inward or outward, while at high latitudes the field is dipolar. The sunspot magnetic fields are drawn out into interplanetary space by the solar wind because the charged particle kinetic energy density is greater than the magnetic field energy density. If this were not the case, the solar wind would simply be trapped in the sun's magnetic field. A measure of the success of a plasma in controlling a magnetic field is given by the ratio of the kinetic energy density to the magnetic energy density,

$$\beta = \frac{\frac{1}{2} \rho_m v_s^2 + 3nkT}{B^2/8\pi} \quad (1)$$

where,  $\rho_m$  = mass density of the plasma,  
 $n$  = number density of the plasma,  
 $k$  = Boltzmann's constant,  
 $T$  = kinetic temperature,  
 $B$  = magnetic induction in gauss,  
 $v_s$  = solar wind streaming velocity,

so that, roughly speaking,  $\beta > 1$  implies plasma control. Except for regions very near the sun, the solar wind streaming energy is much greater than its thermal energy. At 1 A. U. characteristic values are,  $n = 5$  ion pairs  $\text{cm}^{-3}$ ,  $B = 6 \times 10^{-5}$  gauss,  $T = 10^5 \text{ }^\circ\text{K}$ ,  $v_s = 500$  km/sec, giving a  $\beta$  of about 1. (Neugebauer and Snyder; 1966, 1967).

The configuration of the interplanetary magnetic field is further determined by the fact that the solar corona is very tenuous and therefore essentially collisionless so that the magnetic flux should under most circumstances be frozen in to the plasma (Alfven and Falthammer, 1963).

The above ideas have proved valuable in the assessment of solar wind interactions. Moreover, it has been shown that the deformation of the magnetosphere is well represented by a zero-temperature, field-free solar wind interacting with the dipole geomagnetic field and this fact has made possible extensive theoretical treatments of the problem (see Beard; 1960, 1964; Mead, 1964). As pointed out by Beard, 1964, in its simplest approximation the problem reduces to the solution of the force equation,

$$\rho_m \frac{d\bar{v}}{dt} = -\nabla (p_s + B^2/8\pi), \quad (2)$$

where,  $p_s$  is the solar wind streaming pressure and  $\bar{v}$  the plasma velocity. The condition for equilibrium is  $\rho_m \frac{d\bar{v}}{dt} = 0$ , or  $p_s + B^2/8\pi = \text{constant}$ . An important point arises here. In a zero-temperature plasma there is no isotropic pressure and furthermore the effective pressure is given by the pressure of the particles perpendicular to the local magnetic field vector. There are two boundary conditions which must be applied along the surface of the resulting magnetopause. First, the normal component of  $\bar{B}$  must be continuous across the boundary. Let  $R_s(\lambda_M, \varphi_M)$  denote the geocentric distance to the boundary as a function of geomagnetic latitude and longitude. Then, since  $\bar{B} = 0$  for  $R_s(\lambda_M, \varphi_M) + \epsilon$  and  $\bar{B} \neq 0$  for  $R_s(\lambda_M, \varphi_M) - \epsilon$  for vanishing

$\epsilon$ , the magnetic field just inside the surface must be tangential to the boundary. Secondly, the particle pressure must vanish inside the boundary, so that the condition for equilibrium becomes,

$$p_{s\perp} = B^2/8\pi . \quad (3)$$

Then, if specular reflection is assumed at the boundary (Beard, 1964), and the effect of electrons is neglected due to the small value of their momentum, the total momentum change of a reflected ion is  $2m_i v \cos \theta$ , while the number of ions striking the surface per unit area per second is  $nv \cos \theta$ , where  $n$  is the density of ion pairs and  $\theta$  is the angle of incidence. The resulting kinetic pressure normal to  $\bar{B}$  and hence to the surface is (Beard, 1964),

$$p_{s\perp} = 2nm_i v^2 \cos^2 \theta . \quad (4)$$

Thus, the surface is determined by the equilibrium condition,

$$B = (16\pi nm_i v^2 \cos^2 \theta)^{1/2} , \quad (5)$$

where  $B$  is the magnetic induction just inside the boundary, which is produced by the geomagnetic dipole and the currents which flow in the surface of the magnetosphere due to the particle reflections. The surface currents must cancel the field outside the boundary and hence will add to the field inside (Mead and Beard, 1964), resulting in an approximate doubling of the dipole field near the subsolar point. At higher latitudes the surface currents have a much more pronounced effect. At a geomagnetic latitude of approximately

$80^{\circ}$  the field due to the surface currents exactly cancels the dipole field, producing two neutral points as shown in Figure 1. At latitudes above about  $80^{\circ}$ , the resulting field lines are projected back in the antisolar direction, forming the geomagnetic tail. The night side field lines are affected to a somewhat lesser degree as shown in Figure 1. Calculations of the leading edge configuration using a solar wind model as outlined above have been quite satisfactory. However, the transverse solar wind pressure is important in determining the downstream boundary so the zero-temperature approximation breaks down. Also, there are factors such as plasma pressure and hydromagnetic waves which tend to inflate the tail region and these are difficult to estimate (Dessler, 1964). Moreover, the above model erringly predicts that the flow of solar wind around the geomagnetic obstacle will just be the combined motions of the individual particles resulting from their specular reflection at the boundary. The latter problem can be overcome to some extent by considering the interaction in the framework of the gas dynamical analogy.

According to the gas dynamical analogy, the perturbed solar wind (which is collisionless) should react much like a collision-dominated neutral gas which has encountered a solid object. In the usual gas dynamical case, the sudden compression caused by the solid object is propagated upstream by a longitudinal wave at the sonic velocity and it is this wave which deflects the oncoming gas around the obstacle. A supersonic flow velocity requires the existence of a shock front upstream of the object if deflection is to occur. An analogous situation is found to exist in

the case of the solar wind, in which the presence of the earth's magnetic field perturbs both the particles and the solar magnetic field, resulting in the upstream propagation of sound waves and hydromagnetic waves. The supersonic and superalfvenic solar wind velocity leads to the formation of a shock wave just as in the gas dynamical case. Since the solar wind must still be considered collisionless in the usual sense in view of the frozen-in magnetic flux, the ordered flow must result from particle-wave or particle-field interactions. A popular viewpoint is that the interplanetary magnetic field organizes the flow in the sense that a deflected particle is returned to an average streaming velocity within one cyclotron period (Gold, 1959; Michel, 1965). In any case, the gas dynamical analogy has lead to values of the stand-off distance and the thickness of the shock as well as estimates of the bulk flow around the magnetosphere which compare favorably with the observations as outlined below.

Magnetometers aboard the spacecraft Pioneer 1 and 5 (Sonett et al., 1960; Coleman et al., 1960) and Explorer 12 (Cahill and Amazeen, 1963) among others detected a region of randomly oscillating magnetic field strength between the magnetopause and the streaming solar wind. Plasma detectors on Pioneer 4 (Van Allen, 1959), IMP 1 (Bridge et al., 1965), IMP 2 and OGO 1 (Wolfe et al., 1966), and Vela 2 (Gosling et al., 1967) have indicated that a highly disordered plasma flow is also characteristic of this region and furthermore that the sharp transition at the solar wind boundary indicates a thin shock with a somewhat thicker magnetosheath between the shock and the

magnetopause.

It therefore is evident that a thermalization process not unlike that predicted by the aerodynamic analogy occurs at the shock. Moreover, the presence of a nonthermal high energy tail comprising from 10% - 25% of the total ion flux (Wolfe et al., 1966), the detection of a hard ( $>30$  kev) electron component just at the shock boundary (Fan et al., 1964), and the occurrence of  $\sim 1$  kev electrons throughout the magnetosheath (Freeman et al., 1963) suggest that the unknown entropy-increasing process necessitated by the gas dynamical analogy may be accompanied by an appreciable acceleration of individual ions and electrons.

The straightforward analogies discussed above are quite successful, then, in predicting the shape of the day side magnetopause as well as the existence of thermalized solar wind and a disordered magnetic field in the magnetosheath. However, in view of the difficulty of predicting by a simple model the configuration of magnetic field lines which are swept back into the geomagnetic tail, recent measurements of the magnetic fields and particle populations in that region are quite important and worthy of mention.

#### C. Charged Particle and Magnetic Field Measurements in the Geomagnetic Tail.

A salient feature of the tail region particle population is the existence of a plasma sheet near the equatorial plane. Magnetometers aboard IMP 1 (Ness, 1965) detected a region of field reversal near the equatorial plane such

that north of the reversal the field pointed inward while south of the reversal it pointed outward, that is, in the antisolar direction. The region of reversal at geocentric distances of  $9 R_E$  to  $30 R_E$  was observed by Ness to have a north-south thickness of about 600 km or approximately the cyclotron radius of a 1 kev proton in the tail field ( $\sim 20\gamma$ ). As noted by Axford et al., 1965, a plasma is expected to exist in this "neutral sheet" to prevent the collapse of the field configuration. The associated plasma is observed to be much thicker ( $4-6 R_E$ ) than the region of field reversal and to extend from the dawn to dusk boundaries of the magnetosphere (Bame et al., 1967). Moreover, plasma kinetic energy densities are found to be comparable to the magnetic field energy density inside the neutral sheet but much lower outside the sheet. Only background counting rates were observed by the Vela electrostatic analyzers in other regions of the tail, indicating that either the particle energies were less than the 190 ev detector thresholds or fluxes were less than the  $10^7 \text{ cm}^{-2} \text{ sec}^{-1}$  minimum detectable omnidirectional flux. It was noted that electron and proton densities and energy spectra were similar in the neutral sheet region. Therefore, since the slower-moving protons yielded lower counting rates and poor statistics, the Vela analyzers were operated in the electron mode most of the time. Many examples of data obtained in this region are given by Bame et al., 1967, the electron spectra being generally harder than those measured by the same spacecraft in the magnetosheath, with average energies between 200 ev and omnidirectional fluxes up to  $10^9 \text{ cm}^{-2} \text{ sec}^{-1}$  (see Figure 2).

Energetic electron "island" fluxes in the same general region have been reported by Anderson, 1965, Montgomery et al., 1965, and Konradi, 1966. Omnidirectional electron fluxes up to  $10^7 \text{ cm}^{-2} \text{ sec}^{-1}$  were detected in a zone beyond the boundary of trapping and generally between the  $\pm 30^\circ$  meridians of geomagnetic latitude. Building up typically in tens to hundreds of seconds, these fluxes die away with a gradual softening in energy (e-folding energy dropping from about 10 kev to 5 kev) within a few hours and are interpreted as temporal changes at fixed locations. Anderson and Ness, 1966, have noted that the fluxes are associated with broad regions of magnetic field depression. It is not known if these depressions are accompanied by large densities of low energy particles, but it has been suggested that the magnetic field decrease is caused by charged particle diamagnetism. Alternatively, and this would preclude the simultaneous increase of low and high energy fluxes, Axford et al., 1965, and O'Brien, 1967, have conjectured that magnetic merging in the tail might result in the decrease in field intensity and an associated transfer of magnetic energy to particle kinetic energy.

Although we have defined experimentally several charged particle domains which contain particles of "auroral" energies and can approximate theoretically the various possible configurations for high-latitude magnetic field lines, we are not as yet able in this framework to define an auroral field line or an auroral particle source. As we will discuss further in the final section, the processes of auroral particle injection and acceleration are basic to the interaction of the solar wind with the rotating magnetized earth



and there is a need for more accurate theoretical treatments including second-order effects (Axford, 1967). However, just as essential to the solution of these problems are extensive and accurate measurements of the polar charged particle population at low altitudes. As outlined below, our knowledge of these particles is lacking in most respects.

D. Measurements of High-Latitude Charged Particles at Low Altitudes.

In this section, we will outline the general status of low altitude particle measurements in the polar regions.

Considering first the electron data, we recall that the initial observations of electrons precipitating into the auroral zone were made with geiger tubes launched aboard rockoons (Van Allen, 1957) and X-ray scintillators carried aloft on balloons (Anderson, 1960; Winckler, 1961). However, the electrons which are detected by geiger tubes and which cause the bremsstrahlung that is detectable at balloon altitudes ( $E \geq 30$  kev) are not the particles responsible for most auroral light.

Early rocket flights into visible auroras (Davis et al., 1960; McIlwain, 1960) revealed that most of the auroral light could be explained by the observed influx of electrons in the energy range 5 - 10 kev. More recent night-time sounding rocket observations above auroral arcs indicate that the bulk of the incoming electron energy resides in a "near-monoenergetic beam" in the range 4 - 10 kev, with a

peak intensity of about  $10^5 - 10^6 \text{ cm}^{-2} \text{ ster}^{-1} \text{ ev}^{-1} \text{ sec}^{-1}$ . Most of these experiments were conducted during auroral substorms (Evans, 1967a; Albert, 1976a; Westerlund, 1968) with the peak differential flux occurring at 6 - 10 kev. In addition, there have been two such measurements above quiet auroral forms, with Evans, 1967b, noting a peak at 3.8 kev, and Chase, 1967, a peak at 10 kev. Westerlund, 1968, has shown that the auroral electron spectrum is actually double-peaked, exhibiting a further rise in intensity below 1 kev with a second peak near 100 ev, and in addition that between the arcs the 6 - 10 kev peak disappears from the spectrum. Such behavior is interpreted as resulting from a background continuum electron flux upon which the primary auroral beam is superimposed.

Albert, 1967a, noted that the peak energy of the nearly monoenergetic beam which he detected during a 500  $\gamma$  negative bay increased from 10 kev to 14 kev as the rocket traversed about 70 km toward lower magnetic latitudes. He suggests that a 55 mv/meter northward electric field could produce this effect. We should note, however, that a clear latitudinal dependence of the peak energy has not generally been detected. The only day side measurement of such a spectrum was obtained by Chase, 1967, who found a peak in the range 2 - 5 kev in two rocket flights during X-ray events at local times 1100 - 1200.

Sounding rocket pitch angle measurements of downward-moving low and high energy electrons indicate a general tendency to peak normal to B, but becoming more isotropic with increasing intensity (see, e. g., McDiarmid et al.,

1967; McDiarmid and Budzinski, 1964). It is usually found that for both low and high energies the upward-moving flux is about 10% of the downward-moving flux (see, e. g., Westerlund, 1968).

Another generally accepted result of sounding rocket auroral investigations is that the higher energy ( $\geq 20$  kev) electrons are more variable in space and time than the electrons in the  $\leq 10$  kev range (see, e. g., Evans, 1967a; Chase, 1967). Although the higher energy electrons are fairly well correlated with auroral fluctuations and other auroral phenomena such as absorption of cosmic radio noise, they are considered by many investigators to be by-products of the primary auroral precipitation. That is, sporadic bursts of high energy electrons in auroras may be produced in the interaction of the kev electrons with the ionosphere.

Since the limited operating time of a sounding rocket payload dictates to the practical investigator the presence of some type of "event" as a prerequisite for launch, satellites are better suited to the study of normal conditions. The initial observation that the high-latitude trapping boundary of electrons ( $\geq 40$  kev) undergoes a diurnal variation which agrees well with that of the visual auroral zone (O'Brien, 1962) was the basis for continuing speculation concerning the nature of the relationship between auroral electrons and trapped electrons. The trapping boundary for these electrons was found at an average invariant latitude of  $75^\circ$  in the local day and  $69^\circ$  in the local night and was noted to move to lower latitudes with increasing magnetic activity (Maehlum and O'Brien, 1963),

a behavior which had previously been observed in visual auroral observations. Subsequent measurements at higher energies ( $E \geq 280$  kev) by Williams and Palmer, 1965, demonstrated that the night-side trapping boundary latitude is slightly lower for higher energies and that the diurnal variation for these energies is only  $\sim 2.4^\circ$ . Williams and Mead, 1965, have noted that this diurnal variation could be explained by solar wind distortion of the geomagnetic cavity while invoking a day-side source mechanism to explain the larger diurnal variation of 40 kev electrons. This conclusion is quite possibly incorrect since Dessler, 1965, has noted that the diurnal variation of the boundary of trapping should be larger in the summer hemisphere and larger in general for smaller values of the angle between the earth's dipole axis and the earth-sun line. Dessler has shown further that the observations of Williams and Palmer, 1965, and others could be explained on a gross scale by such considerations. Injun 3 simultaneous observations of electrons ( $\geq 40$  kev) and auroral light (3914 A) attached an even greater significance to the position of the 40 kev boundary (O'Brien, 1964). In that experiment, many passes through the night-side trapping boundary revealed a simultaneous increase in trapped and precipitated particles, resulting in a nearly isotropic pitch angle distribution of downward-moving electrons and an accompanying increase of auroral light. The question of the exact position of the auroral zone with respect to the trapping boundary was not answered, however, since the maximum 3914 A emission frequently occurred just outside the 40 kev boundary and since intensity spikes of lower

energy electrons ( $\geq 10$  kev) were detected above the boundary during local night by an electron multiplier aboard the same spacecraft (Fritz and Gurnett, 1965).

Geiger tube data from the topside sounder Alouette 1 as reported by McDiarmid and Burrows, 1965, indicates energetic ( $\geq 40$  kev) electron precipitation generally narrow in latitudinal extent ( $\sim 2^\circ$ ) and grouped strongly on the night side of the earth. Most events occurred between L values of 8 and 20 with precipitation observed at times up to  $L > 50$ . Similar spikes were observed by O'Brien et al., 1962, who showed that their energy spectra were somewhat softer than that typical of outer zone electrons. It has been speculated (see, e. g., O'Brien, 1967) that these spikes represent a geomagnetic mapping to low altitudes of the "island" fluxes in the tail which were discussed above. This viewpoint has recently been supported by the observations of Reid and Parthasarathy, 1966, who have shown the spikes to be temporally associated with high latitude riometer absorption. Lin et al., 1968, reporting on further Alouette 1 data, observed during an auroral substorm the continuous occurrence of energetic ( $\geq 40$  kev) electrons for many degrees north of the normal trapping boundary. These electron fluxes are more intense and more isotropic than those observed below the usual boundary of trapping and are detected in the latitude region where "spikes" are seen to occur in normal passes. Such considerations have led those experimenters to conclude that these electrons come from a source outside the trapping region and probably originate in the magnetospheric tail.

Prior to the experiment described herein, the only high-latitude satellite measurements of electrons of "auroral" energies have been made by the Lockheed group aboard polar-orbiting satellites in the altitude range 150 - 300 km. These satellites were earth-center oriented and had rather short orbital lifetimes (3 - 5 days). Their extensive investigations into the average properties of high-latitude electron precipitation above 80 ev have been summarized recently by Evans et al., 1967, Sharp and Johnson, 1967, and Sharp and Johnson, 1968. Some of the principal features of their results are:

(1) The day side region of electron precipitation was observed to consist of two zones -- a low-latitude zone in which both the 80 ev and the 21 kev threshold detectors responded above background and a higher latitude zone in which only the 80 ev threshold detector so responded (see Figure 3). The pitch angle distributions in both regions tended to peak normal to the local geomagnetic vector, becoming more isotropic with increasing intensity. The soft region was more anisotropic in pitch angle as well as at a given pitch angle along the satellite trajectory.

(2) The total precipitated electron energy (combining the two day-side zones) was found to be approximately five times as high on the night side as on the day side. In addition, electron fluxes were on the average somewhat harder and more isotropic on the day side. It is important to realize that this spectral information is based on the ratio of the count rate in the 21 kev threshold detector to that in the 80 ev threshold detector, with pitch angle distributions obtained from two 80 ev threshold detectors which sampled approximate pitch angles of  $0^{\circ}$  and  $56^{\circ}$ .

(3) Electron precipitation occurred generally along the auroral oval with total energy flux showing a maximum for southern hemisphere passes at 7 - 9 hours auroral time (a local time referenced to the center of the auroral zone). The distribution in invariant colatitude of the centers of the night-side region and the two day-side regions is shown in Figure 3.

(4) The total energy of electrons ( $>80$  ev) precipitated into the auroral zone showed a strong dependence on geomagnetic activity. For example, for night-side passes the average precipitated energy varied from  $20 \text{ ergs cm}^{-2}$  to  $200 \text{ ergs cm}^{-2}$  as  $K_p$  increased from 1 to 3.

(5) Electron spectra during a given pass became systematically harder with increasing intensity.

(6) Several integral spectra have been presented by Evans et al., 1967, for the hard electron regions, indicating that most of the energy was carried by electrons of energies less than 10 kev. A few differential spectra obtained with channel multiplier detectors with center energies at 1, 2, and 5 kev have been published by Sharp and Johnson, 1967, for the day-side soft region. These spectra, which will be considered in more detail in the final section, are such that most of the energy is in the form of electrons with energies somewhat below 5 kev.

There is as yet very little knowledge of the characteristics of auroral protons. The detection of a doppler-shifted Balmer ( $H_\beta$ ) line in auroral spectra and its interpretation by Vegard, 1948, as due to neutralized protons streaming toward the observer was the first indication of

proton precipitation in visible auroras. Although incoming protons can excite other characteristic auroral wavelengths such as 3914 Å and 5577 Å, the doppler-shifted Balmer emissions have been most valuable in ground-based studies of proton precipitation patterns. A proton auroral zone has been generated through such observations (Eather, 1967) and is found to lie on the average equatorward of the visual auroral zone.

Early rocket flights into visual auroras during periods of relatively high magnetic activity (Davis et al., 1960; McIlwain, 1960) indicated that auroral protons ( $\geq 100$  keV) undergo more gradual variations than do the high energy electrons. Rocket flights during intense auroral activity established that the integral precipitated proton energy is a small fraction, perhaps 1/100 (Albert, 1967b) or 1/1000 (McIlwain, 1960) that carried by the electrons. However, a recent rocket measurement in a quiet  $H_p$  aurora (Whalen et al., 1967) revealed large proton fluxes ( $\sim 10^6 \text{ cm}^{-2} \text{ ster}^{-1} \text{ sec}^{-1}$  above 30 keV) in the presence of very weak electron fluxes ( $< 3 \times 10^3 \text{ cm}^{-2} \text{ ster}^{-1} \text{ sec}^{-1}$  above 20 keV) for most of the flight. This result indicates that protons may be responsible for most of the energy precipitated into the auroral zone during quiet periods.

The results of the sounding rocket measurements of auroral proton spectra in the 10 - 100 keV energy range (see, e. g., Whalen et al., 1967; Albert, 1967b) may be represented by exponential-type integral spectra with e-folding energies of 10 - 20 keV. Chase and Anderson, 1967, operating in the energy range below 10 keV in a



visible aurora, found a proton flux at  $90^\circ$  pitch angle which peaked between 750 ev and 1500 ev at  $2 \times 10^3 \text{ cm}^{-2} \text{ ster}^{-1} \text{ ev}^{-1} \text{ sec}^{-1}$  and decreased out to the maximum observed energy of 20 kev.

The only rocket measurements of proton pitch angle distributions have been obtained by Whalen et al., 1967, Mozer, 1965, and Mozer and Bruston, 1966. The pitch angle distributions reported by Whalen et al., 1967, in the energy range 20 - 200 kev were isotropic for downward-moving protons, but dropped sharply for pitch angles greater than  $90^\circ$ , until at  $120^\circ$  the intensity was about 1/100 that near  $0^\circ$ . In contrast, the observations of Mozer, 1965, indicated pitch angle distributions which were peaked at  $90^\circ$  for 160 kev protons but isotropic for higher energies ( $\sim 750$  kev). More recent pitch angle determinations were made from a rocket fired into a breakup phase aurora (Mozer and Bruston, 1966). For energies between 140 and 250 kev, the distribution was peaked at  $90^\circ$  but was isotropic within a factor of two for pitch angles less than  $90^\circ$ . However, the distribution of upward-moving protons was even more isotropic, indicating an excess of these protons. For higher energies (250 - 450 kev), the upward flux never exceeded the downward flux but remained constant while the downward flux varied over a factor of two. The lower energy observation is interpreted by Mozer and Bruston, 1966, as requiring the existence of a low-altitude ( $< 300$  km) acceleration mechanism which can accelerate protons by some tens of kilovolts.

This interpretation is very much in doubt, especially in view of the sampled pitch angle range of  $50^{\circ}$  to  $130^{\circ}$ . That is, at rocket altitudes the loss cone is about  $50^{\circ}$  wide, so that Mozer and Bruston's proton detector did not actually sample the loss cone, in which atmospheric loss processes should reduce the upward proton flux considerably. It is quite possible that if all pitch angles had been sampled the total number of reflected protons would not have outnumbered the downward-moving protons. If this were the case, the problem of explaining their observations in the sampled range would be reduced to understanding a mechanism which can cause a proton which is moving downward at rocket altitude at a pitch angle less than  $50^{\circ}$  to be reflected in some way and reappear at the rocket altitude at a pitch angle less than  $130^{\circ}$ . It is possible that some type of pitch angle scattering, perhaps by charge exchange collisions, could cause such behavior. Low-altitude proton acceleration has also been contradicted by Reasoner, 1968, who found the auroral proton to alpha ratio to be the same as that in the solar wind.

Satellite proton measurements at high latitudes are also very few in number, having been conducted only by the Lockheed group, whose findings are summarized by Sharp et al., 1967, Evans et al., 1967, and Sharp and Johnson, 1967. We should note that in the altitude range sampled by their polar-orbiting satellites (150 - 300 km) most of the detected "protons" were actually energetic neutralized hydrogen atoms. For example, reference to the calculations of Eather, 1967, reveal that at these altitudes at least 75% of the incident 10 kev protons will be in the form of

neutralized hydrogen due to charge exchange collisions. Although the detection of neutralized protons is still possible with threshold detectors, the zone of precipitation will be spread out since the hydrogen atoms are free to move across magnetic field lines. This point also applies to most of the rocket experiments discussed above except for energies greater than 200 kev, for which charge exchange collisions are unimportant (Eather, 1967).

Nevertheless, the average properties of the precipitation patterns of protons with energies greater than 4 kev have been investigated in detail by the Lockheed experimenters mentioned above. Their reported measurements were conducted on two orbital flights. The first, conducted during a relatively quiet ( $K_p \leq 5$ ) five-day period in October - November of 1963, made measurements of the total precipitated proton energy above 4 kev.

Proton precipitation for this flight, which sampled auroral times of 0000-0300 and 1130-1500, was observed to be distributed fairly uniformly along the proton auroral zone mentioned above except for a conspicuous absence of precipitation during the hours just before auroral noon. There was also noted a tendency for total precipitated energy during auroral times 1300-1500 to increase as the tilt of the geomagnetic axis with respect to the earth-sun line decreased due to the earth's rotation. The locations of proton precipitation were mainly between L values of 5 and 10 on the night side and between L values of 8 and 20 on the day side. The day-side region frequently extended down to L=4 during the more disturbed times

( $K_p \geq 3$ ). The total energy precipitated in these zones by protons of energies above 4 kev averaged about  $4 \text{ ergs cm}^{-2} \text{ ster}^{-1}$  during local night and  $3 \text{ ergs cm}^{-2} \text{ ster}^{-1}$  during local day. These values are for the northern hemisphere and it is interesting to note that for that flight, which occurred during October - November, the total energy was higher for the southern hemisphere, being closer to  $5 \text{ ergs cm}^{-2} \text{ ster}^{-1}$  during local night. Evans et al., 1967, have calculated the ratio of total precipitated proton energy (above 4 kev) to total precipitated electron energy (above 80 ev) for each zone crossing and have found a median value of .14 for night time crossings with relatively little variation with auroral time or universal time. On the other hand, for day-time crossings this ratio was nearly unity (except before noon when no protons were observed) with a strong dependence on auroral time and universal time. This ratio reached a maximum for 1330 auroral time when the universal time was near 0700, but dropped to zero for the same auroral time when the universal time was near 1800.

A more recent flight near local times 1100 and 2300 during an exceptionally quiet  $2\frac{1}{2}$  day period in November, 1965, resulted in some spectral information as well as precipitation patterns which were significantly different than those discussed above (Sharp et al., 1967). The lowest energy sampled during this flight was 10 kev, integral spectra being obtained with scintillator detectors with thresholds at 10 kev and 57 kev and channel multiplier detectors with thresholds at 21 kev, 38 kev, and 56 kev. All channel multiplier detectors were oriented at  $55^\circ$  to

the zenith, so pitch angle distributions were obtained only with the scintillator detectors which were oriented at  $0^\circ$  and  $55^\circ$  to the zenith. Their findings on this flight may be summarized as follows:

(1) Although magnetic activity was at an unusually low level ( $K_p > 1$  for only two three-hour periods during the  $2\frac{1}{2}$  day experiment) precipitating protons were observed during 65 of the 80 auroral zone crossings. The total precipitated proton energy showed only a weak tendency to decrease with decreasing  $K_p$  for the limited range of magnetic activity encountered.

(2) The night-side zone of proton precipitation was centered at  $68^\circ$  invariant latitude while the day-side precipitation was separated into two zones centered at invariant latitudes of  $70^\circ$  and  $77^\circ$ . No spectral or total energy differences were noted in the two zones and for a given pass the proton precipitation was found to lie in one or both of the zones. The zones of proton precipitation are shown in Figure 3. In contrast to the 1963 flight, proton precipitation was observed in both morning and afternoon auroral times.

(3) The total precipitated energy above 10 kev was found to be approximately five times as high on the night side as on the day side. In addition, an upper limit of  $.006 \text{ ergs cm}^{-2} \text{ ster}^{-1} \text{ sec}^{-1}$  for proton energies above 10 kev was set for the polar cap region.

(4) The integral energy spectra above 10 kev could be approximated by exponentials with e-folding energies of 10 - 20 kev. No significant diurnal variation in spectral hardness was observed.

(5) Pitch angle distributions obtained from 21 kev and 57 kev threshold detectors at  $0^\circ$  and  $55^\circ$  from the zenith were generally peaked toward the higher pitch angles but were isotropic within a factor of two.

#### E. Summary of the Principal Results of this Experiment.

Before proceeding with the presentation and discussion of the charged particle measurements which have been obtained in the Aurora 1 experiment, we will summarize briefly some of the more important results.

Considering first the electron data, it will be shown that:

(1) During periods of slight to moderate geomagnetic activity ( $1 \leq K_p \leq 4$ ) and for the magnetic local times sampled (within two hours of magnetic noon and midnight), high-latitude electron precipitation is found to occur in two regions of latitude. In the lower latitude region "auroral" type electron spectra are observed nearly isotropically over the upper hemisphere. These spectra are relatively flat or in some cases peaked in the energy range 1 - 10 kev. In addition, they exhibit a rising intensity below a few hundred ev and a very sharp intensity decrease for energies above  $\sim 10$  kev. Immediately adjacent to and poleward of this region, a zone of much softer electrons is observed. The spectra in this region tend to peak near 100 ev and fall off rather sharply with increasing energy so that nearly all the electrons have energies less than a few kev. Large spatial and/or temporal anisotropies are noted in this region.

(2) The boundary between these two regions is several degrees higher on the day side than on the night side, undergoing a diurnal variation for magnetic local times within two hours of noon and midnight which approximates that of the average electron ( $\geq 40$  kev) boundary of trapping. This boundary tends to lie at lower latitudes during periods of greater magnetic activity. The high-latitude boundary of the soft electron region shows no such systematic variation with magnetic activity but instead has been shown by Maehlum, 1968, to lie at lower latitudes for larger values of the angle between the earth's magnetic axis and the earth-sun line.

(3) The night-side soft electron region is observed to contain localized "auroral" type electron fluxes during an auroral substorm, whereas no such behavior is noted in the day-side zone.

(4) During very quiet periods ( $K_p \sim 0$ ) (at least for the night side) the "auroral" type fluxes are below the level of detectability of this experiment, whereas the soft electron region is still evident.

The proton measurements, which are fewer in number and which are presented only for the night side, show the following behavior:

(1) A region of proton precipitation a few degrees wide is present either just below, or straddling the boundary between the hard and soft electron regions. During moderately active periods, the proton spectra in this zone peak near 10 kev and are much harder than the electron spectra in the range above this energy. During a very quiet period ( $K_p \sim 0$ ) when the hard electron zone is not detected, this hard

proton region remains but with energy spectra peaking closer to 1 kev.

(2) To the north of this zone, softer proton spectra are observed in a region corresponding roughly, but not exactly, to the soft electron region.

(3) During an auroral substorm, the hard proton fluxes expand into the night-side soft proton zone.



## II. DESCRIPTION OF THE EXPERIMENT

### A. Satellite Description.

The Rice University/Office of Naval Research satellite 1967-65B (Aurora 1) was launched from Vandenberg AFB at 2101 U. T., June 29, 1967, into a nearly circular orbit (perigee altitude 3808 km, apogee altitude 3928 km) at an inclination of  $89.82^{\circ}$ . The satellite measures 24 by 14 by 10 inches and weighs 47.2 pounds in its final launch configuration. It was launched together with an Army Corps of Engineers SECOR satellite by a Thor/Burner 2 combination. Injection into the nearly circular orbit was accomplished with a specially developed Boeing solid propellant 1400 pound thrust injection stage. The SECOR-Aurora-injection stage combination, which had been spun to 90 rpm prior to Burner 2 separation, was despun to a nominal zero rpm by a yo-yo despin device 1.5 hours after injection. The payloads were then spring ejected.

Electrical power for the satellite is supplied by 22 nickel-cadmium batteries which are trickle-charged by approximately 1700 solar cells mounted in circular arrays on the surface of the satellite (see Figure 4). At the time of launch an average power of about six watts was thus made available to the satellite system, which operates on 3.5 watts. The duty cycle of the payload is continuous except when the batteries discharge below 80% of capacity, at which time a low-voltage cutoff is actuated and the satellite is turned off until sufficient power is restored.

Scientific instrumentation aboard the satellite includes: (1) An ultraviolet photometer sensitive to the wavelengths 1450 A to 1750 A, (2) A quadrant photometer consisting of a single string of dynodes and a photocathode divided into four electrically and optically distinct parts which are activated sequentially, measuring incident light at the visible wavelengths, 3914 A, 5577 A, and 6300 A, and dark current (Criswell and O'Brien, 1967), and (3) A charged particle detector code-named SPECS (O'Brien et al., 1967), which utilizes an electrostatic analyzer to deflect incoming particles of one polarity into an array of five  $270^\circ$  Bendix channel multipliers and those of opposite polarity toward a helical funnel channel multiplier. The SPECS detector will be described in detail in Section II.D.

Transmitted housekeeping information includes: (1) Various temperatures, measured by thermistors located on a solar panel and inside each photometer electronics module, (2) Relevant voltages, monitored at the battery pack and at the 28 V and 7 V regulated power supplies, (3) The nominal voltage applied to the SPECS deflection plates, (4) Magnetic aspect, as measured by a single flux-gate magnetometer oriented parallel to the detectors, and (5) The output of a channel multiplier lifetime monitor consisting of a  $\text{Ni}^{63}$   $\beta$ -source (1 microcurie) mounted in front of a helical funnel channel multiplier. The location of the various sensors is shown in Figure 5.

## B. Telemetry.

The satellite telemetry consists of an FM/FM FSK analog system utilizing standard IRIG channels 5 through 9. A block diagram of a typical channel is shown in Figure 6. The housekeeping information listed above is subcommutated and transmitted on Channel 5 with a cycle time of 16 seconds, of which 12 seconds are used in continuously transmitting the SPECS deflection voltage. Channel 6 was designed to transmit continuous magnetometer information for the first 16 days of orbit, after which it was to sample continuously the output of the ultraviolet photometer. However, at some time between launch and satellite turn-on, the magnetic latching relay switched prematurely to the photometer so that magnetometer information is obtainable only on Channel 5, i. e., for a period of .2 seconds every 16 seconds.

The inputs to channels 6 through 9 are detector outputs which have been processed in the following manner. The outputs of all three detectors described above are in the form of voltage pulses which in each case are fed into a scaling circuit consisting of a series of bistable flip-flop circuits. The input to the subcarrier oscillator is produced by superimposing the outputs of three taps along the scaler trains. The higher frequency transitions are filtered out at the scaler output. Channel designations and scaler taps for the four channels are as follows:

<u>Channel</u>	<u>Center Frequency</u>	<u>Detector</u>	<u>Scaler Taps</u>
6	1.7 kHz	U. V. Photometer	$2^2, 2^6, 2^{10}$
7	2.3 kHz	SPECS ( $270^\circ$ multipliers)	$2^1, 2^5, 2^{10}$
8	3.0 kHz	Quadrant Photometer	$2^1, 2^5, 2^9$
9	3.9 kHz	SPECS (Funnel)	$2^4, 2^9, 2^{14}$

The frequency modulated subcarriers are then combined in a mixer amplifier and transmitted on a carrier frequency of 137.14 MHz. The transmitter, which was built by Space Craft Inc., delivers 670mw to the antenna terminals. The antenna system consists of a turnstile array of four quarter wavelength monopoles, each of which is fed  $90^\circ$  out of phase with its adjacent element. Predicted maximum subcarrier slant range is approximately 4500 nautical miles.

### C. Magnetic Orientation.

As indicated in Figure 5, an Alnico V bar magnet is mounted parallel to the detectors for the purpose of orienting them with respect to the earth's magnetic field. The alignment is such that in the northern hemisphere the photometers view downward along the field line while the SPECS entrance aperture is pointed up the field line, that is, to sample precipitated particles. The bar magnet experiences a torque due to the geomagnetic field, thereby imparting angular kinetic energy to the satellite. This rotation, in the presence of the earth's magnetic field, results in a time-varying magnetic field which is experienced by ferromagnetic permalloy rods mounted on the satellite. Hysteresis losses in these rods dissipate

energy from the source of the magnetic field variation (the satellite's rotation) so that the angular kinetic energy is decreased. Therefore, the maximum potential energy attainable by the system is also decreased, hence restricting the amplitude of the motion about  $\bar{B}$ . For one complete revolution, the angular kinetic energy is decreased by an amount given by,

$$\Delta E = \oint \bar{H} \cdot d\bar{B} , \quad (6)$$

which is equivalent to the area enclosed by the hysteresis curve of the permalloy rods for the experienced magnetic field variation. Therefore, as time progresses and the maximum angular deviation of the magnet from the geomagnetic vector is decreased, magnetic orientation is approached, but the energy dissipated per cycle is diminished. This effect is shown in Figure 7, where the maximum deviation is plotted as a function of time. This figure indicates that the method is an effective one (see also O'Brien et al., 1964).

Before orientation, the particle detector was able to sample a large range of pitch angles. However, measurement of the distribution in pitch angle of the counted particles requires magnetic aspect information. As noted above, magnetometer readings are available but once every 16 seconds and possible extrapolations between these measured values are many. Indeed, if the period is shorter than the 16-second sampling interval, such extrapolation would be very difficult. For this reason an analysis of the expected motion of the satellite and the period of its oscillation

about the geomagnetic vector is presented.

The principal axes of the satellite are as designated in Figure 5. Measurements of the center of gravity indicate that all products of inertia are less than  $1 \text{ lb ft}^2$  ( $\pm 20\%$ ). The principal moments of inertia were measured by suspending the payload on two wires of length  $l$  with distance  $w$  between them and rotating it through a small angle. The period of oscillation which resulted upon its release is related to the moment of inertia about the axis parallel to the wires and the other known parameters as follows,

$$T = 4\pi \left[ \frac{I_i l^2}{Mgw^2} \right]^{\frac{1}{2}}, \quad (7)$$

or,

$$I_i = \frac{Mgw^2 T^2}{16 \pi^2 l^2}, \quad (8)$$

where,

$T$  = period of oscillation,  
 $g$  = acceleration due to gravity,  
 $M$  = total mass of satellite,  
 $l$  = length of wires,  
 $i$  = principal axis,  $x$ ,  $y$ , or  $z$ .

This equation is approximately correct for small amplitudes and negligible torsion in the wires. A derivation of this relation is given in Appendix I. The measured values are:

$$\begin{aligned} I_x &= 19.8 \text{ ft}^2 \text{ lb} \pm 10\% \\ I_y &= 20.0 \text{ ft}^2 \text{ lb} \pm 10\% \\ I_z &= 10.0 \text{ ft}^2 \text{ lb} \pm 10\% \end{aligned}$$

Due to the small values of the products of inertia, we will

consider the inertia tensor diagonal in this treatment.

The orientation of the satellite will be specified by defining a space set of axes such that  $\bar{B}$  is directed toward the vertical and the position of the three principal axes are given by the Euler angles  $\varphi$ ,  $\theta$ , and  $\psi$ , as defined by Goldstein, 1950, (see Figure 8). Note that we have fixed one point (the center of mass) at the origin of coordinates. To simplify the calculations, we will assume that the satellite was despun completely so that initially,

$$\dot{\varphi} = \dot{\theta} = \dot{\psi} = 0. \quad (9)$$

Since the bar magnet is oriented parallel to the x-axis, the only torque involved is directed along the line of nodes. Thus,  $\dot{\varphi}$  and  $\dot{\psi}$  are constant in time and hence always zero, so that the consequence of the above assumption will be the elimination of precession and nutation about B.

The Lagrangian for the described system is,

$$L = \frac{1}{2}I_x\omega_x^2 + \frac{1}{2}I_y\omega_y^2 + \frac{1}{2}I_z\omega_z^2 + MB \cos \theta, \quad (10)$$

where,

$\omega_i$  = angular velocity about i-axis,

M = magnetic moment of bar magnet,

B = magnetic field in gauss,

and the angle  $\theta$  is as shown in Figure 8. The angular velocities about the body axes can be written in terms of the Euler angles as,

$$\begin{aligned}\omega_x &= \dot{\varphi} \cos \theta + \dot{\psi} \\ \omega_y &= \dot{\varphi} \sin \theta \cos \psi - \dot{\theta} \sin \psi \\ \omega_{-z} &= \dot{\varphi} \sin \theta \sin \psi + \dot{\theta} \cos \psi ,\end{aligned}\tag{11}$$

or, since  $\dot{\varphi} = \dot{\psi} = 0$ ,

$$\begin{aligned}\omega_x &= 0 \\ \omega_y &= -\dot{\theta} \sin \psi \\ \omega_{-z} &= \dot{\theta} \cos \psi.\end{aligned}\tag{12}$$

Inserting these values into the Lagrangian, the equation, of motion for  $\theta$  becomes,

$$\frac{d}{dt} \frac{\partial L}{\partial \dot{\theta}} - \frac{\partial L}{\partial \theta} = 0,\tag{13}$$

or,

$$(I_y \sin^2 \psi + I_z \cos^2 \psi) \ddot{\theta} = -MB \sin \theta.\tag{14}$$

This equation is of the same form as that for the simple pendulum, and therefore will have the general solution (see, e. g., Synge and Griffith, 1959),

$$\theta = 2\sin^{-1} \left[ (\sin \frac{1}{2}\Theta) \operatorname{sn} \left\{ \left( \frac{MB}{(I_y \sin^2 \psi + I_z \cos^2 \psi)} \right)^{\frac{1}{2}} (t - t_o) \right\} \right],\tag{15}$$

where,

$\Theta$  = maximum value of  $\theta$ ,

$t_o$  = initial time,

$\operatorname{sn}(\ )$  = Jacobian elliptic function.

Due to the presence of the damping rods,  $\Theta$  will be a decreasing function of time. However, we can assume that  $\Theta$  is constant for short time intervals. The function  $\operatorname{sn}$  has the property,



$$\text{sn}(x + 4K) = \text{sn}(x), \quad (16)$$

where  $K$  is the complete elliptic integral of the first kind,

$$K = \int_0^{\pi/2} \frac{d\alpha}{(1 - k^2 \sin^2 \alpha)^{1/2}}, \quad (17)$$

in which  $k$  is the modulus of the elliptic function, in this case,  $k = \sin(\frac{1}{2}\Theta)$ . The angle  $\theta$  will have the same periodicity as  $\text{sn}()$ , that is,

$$T_\theta = 4K \frac{(I_y \sin^2 \psi + I_z \cos^2 \psi)^{1/2}}{(MB)^{1/2}}. \quad (18)$$

Inserting the value of the definite integral  $K$  given by Dwight, 1961, we obtain,

$$T_\theta = 2\pi \left( \frac{(I_y \sin^2 \psi + I_z \cos^2 \psi)}{MB} \right)^{1/2}. \quad (19)$$

$$\cdot \left\{ 1 + \frac{1}{22} \sin^2(\Theta/2) + \frac{3^2}{22.42} \sin^4(\Theta/2) + \dots \right\} \text{ sec.}$$

Note that, since the moments of inertia about the  $y$  and  $z$  axes are not equal, the period will depend not only on the local magnetic field strength and the amplitude but on the orientation of the satellite with respect to  $\bar{B}$  as well. Therefore, since we have no way of determining the value of  $\psi$ , we can only set upper and lower limits on the period at a given time. Also, since  $\Theta$  is approximately constant for a given orbit, we can estimate the latitudinal dependence of the period by replacing  $B$  with  $B(\lambda)$ , where  $\lambda$  is the magnetic latitude. Approximating the earth's field by a centered dipole with magnetic moment,

$M_E = 8 \times 10^{25}$  gauss  $\text{cm}^3$ , and assuming a constant satellite altitude of 3900 km, we have,

$$\begin{aligned} B &= (M_E/r^3)(3 \sin^2 \lambda + 1)^{\frac{1}{2}} \\ &= 7.2 \times 10^{-2} (3 \sin^2 \lambda + 1)^{\frac{1}{2}} \text{ gauss.} \end{aligned} \quad (20)$$

The magnetic moment of the satellite was measured to be  $1.2 \times 10^5$  gauss  $\text{cm}^3$ , so the approximate period should be,

$$\begin{aligned} T &= 6.8 \times 10^{-2} (3 \sin^2 \lambda + 1)^{-\frac{1}{4}} \cdot \\ &\cdot (8.4 \times 10^6 \sin^2 \psi + 4.2 \times 10^6 \cos^2 \psi)^{\frac{1}{2}} \cdot \\ &\cdot \left\{ 1 + \frac{1}{22} \sin^2(\Theta/2) + \frac{3^2}{22.42} \sin^4(\Theta/2) + \dots \right\} \text{ sec.} \end{aligned} \quad (21)$$

For example, if  $\lambda = 75^\circ$ ,  $\psi = 45^\circ$ , and  $\Theta = 150^\circ$ , we will have  $T \approx 160$  seconds. Although for large amplitudes, the motion is described by an elliptic function, when the motion is damped to an extent that  $\Theta$  is small, e. g.,  $\Theta \sim 20^\circ$ , the oscillations will become more nearly sinusoidal. Also, the period will decrease with increasing time until  $\Theta$  becomes comparable to  $\sin \Theta$ , after which the period will be independent of further amplitude decrease. These predictions will be compared with observed values in the section on experimental results.

#### D. The SPECS Charged Particle Detector.

The charged particle detector code-named SPECS, for Switched Proton Electron Channeltron Spectrometer, was designed to detect electrons and protons in eighteen energy intervals in the range  $30 \text{ ev} \leq E \leq 100 \text{ kev}$  (O'Brien et al.,

1967). The particle sensors employed are Bendix continuous dynode secondary emission electron multipliers. We will begin our discussion of the SPECS instrument by outlining the principles of channel multiplier operation and the motivation for their use in this application.

#### D.1. Channel Multiplier Characteristics.

The channel multiplier consists of a hollow glass tube on whose inner surface is coated a material of an unnamed chemical nature which may be classified as a semiconductor (as deduced from its observed resistivity) and as an emitter of secondary electrons, the latter property being held in common with all substances. Whereas the idea of such a device is not new (Farnsworth, 1930), the preparation of a surface of the proper resistivity has only recently become technologically feasible. That is, the conductivity must be somewhat greater than that of an insulator, which may have favorable secondary emission properties but would acquire a semi-permanent surface charge upon operation, but less than that of a conductor, across which the necessary applied potential, as described below, would result in a nearly infinite current flow. These devices are available in a variety of configurations of which we have selected two -- the Bendix Model CEM-4010, in which the 1 mm inner diameter tube has the shape of a  $270^{\circ}$  circular sector, and the CEM-4028, in which the 1 mm inner diameter tube has a helical shape, with a conical funnel affixed at the entrance end to increase the sensitive diameter to 8 mm (see Figures 9 and 10). In this application, the entrance end of each channel multiplier is at ground potential, granting

accessibility to particles of all charges and energies, while at the collecting end a potential of +3500 V is maintained. Thus an axial electric field is set up, resulting in the acceleration of any secondaries which may be formed within the channel multiplier. During its axial acceleration, a secondary will drift across the tube in a manner dictated by the velocity and direction of its ejection, subsequently striking the wall with some probability of producing one or more tertiary electrons. If the acceleration between encounters with the wall is such that on the average more than one electron will be emitted for each incident electron, a cascade will result, causing a large number of electrons to appear at the output in a time of a few tens of nanoseconds. Therefore, it is apparent that both the initiating process and the cascade mechanism will be dependent on the secondary emission properties of the coating material for the type and energy of the incident quanta and for the average energy attained by the secondary electrons before striking the wall. The latter property depends chiefly on the operating voltage and any space charge effects which occur as a result of the multiplication. Therefore, we will review briefly the pertinent theoretical and experimental aspects of secondary emission in general and the sparse amount of work which has been done on the channel multiplier itself.

The phenomenon of secondary emission involves two main processes: (1) the conversion of kinetic or potential energy of the primary particle into kinetic energy of an electron of the bombarded material, and (2) escape from the material, in which the secondary electron must survive internal

scattering and overcome the surface potential barrier. The nature of the first process is determined chiefly by the mass, charge and energy of the primary particle.

In the case of electrons, the energy transfer most probably occurs as a result of coulomb collisions with the outer shell, or valence, electrons of the target material atoms. No theoretical model proposed to date predicts satisfactorily all the features of secondary emission by electron impact. However, the predictions of certain theoretical models compare favorably with experimental results in many respects. The most successful of these are generally of two types: (1) a quantum mechanical model of the collision of a single primary electron with a single metal electron using the Bloch model for metals (see, e. g., Woolridge, 1939), or (2) a classical treatment of the interaction of primary electrons with the conduction electrons using the Sommerfeld free electron model for metals (see, e. g., Baroody, 1950). We should note, however, that ejection of a conduction electron by a single primary cannot be made consistent with conservation of both energy and momentum, so that in a strict sense the secondary electron must be considered as initially bound to an atom which can recoil, thereby absorbing the excess momentum. Nevertheless, such theories can predict approximately the secondary emission coefficient as a function of primary electron energy for a given material. Typical of such relationships is the graph shown in Figure 11. At very low energies  $\delta$ , the number of emitted secondaries per incident primary, is seen to increase with increasing primary energy,  $E_p$ . For these energies, the secondaries are produced very near the surface

so that appreciable scattering is not encountered, and the limiting mechanism is probably the work function of the solid, the more energetic primaries producing more secondaries of higher average energy, resulting in a greater probability of overcoming the surface barrier. This concept has been substantiated for very low energies (a few tens of ev) for which  $\delta$  is found to be greater for materials with low work functions than for those with higher work functions. The yield continues to increase with primary energy until the latter exceeds a few hundred ev, after which the depth of penetration exceeds the mean free path of the secondaries and progressively more are lost by internal scattering as the primary energy is increased further. The maximum emission,  $\delta_{\max}$ , varies approximately as the square root of the material density. Additionally, the secondary yield is found to vary with angle of incidence, being greater for larger angles, for which the penetration depth decreases.

Another important effect is the reflection of primary electrons, As predicted by the quantum mechanical treatment of a free particle, there is a finite probability of reflection whenever a particle encounters a change in potential such as presented by the surface barrier of the emitting material. This is true even though the height of the potential is determined by the work function and is hence much lower than particle energies of interest. A typical experimental secondary electron energy distribution is shown in Figure 12, in which the narrow peak at the primary energy results from this type of reflection. Such

a curve does not discriminate between true secondaries and backscattered primaries. However, most of the true secondaries lie in the energy range 0 - 20 ev, while the higher energy electrons are mainly primaries which have rediffused after experiencing multiple scatterings within the target.

Ejection of an electron by an incident ion, as with an incident electron, occurs when an electron is excited into the kinetic energy continuum lying above the surface barrier potential. In the case of positive ions, the source of the excitational energy can be either the kinetic or the potential energy of the ion. The latter source (potential ejection) dominates for the very low ion energies while kinetic ejection becomes important for higher energies ( $E \geq 100$  ev). Kinetic ejection is most efficient for energies of about one kev and above since, due to the unfavorable mass ratio, a low velocity ion is unable to transfer significant kinetic energy to an electron.

For many ions (including  $H^+$ ) potential ejection will occur by direct Auger neutralization when the ion approaches within a few angstroms of the surface. This process will occur only when there are some free electrons in the material. Although we do not know the composition of the channel multiplier emitting surface, we note that the main difference between a semiconductor and a metal in this respect is that the filled valence band and the conduction band overlap in the case of a metal conductor whereas there is an energy gap between the two bands in the semiconductor. The result is that fewer electrons are energetically able

to occupy the conduction band in the semiconductor. Nevertheless, those that can will behave just as metallic conduction electrons, so we will consider the surface as a metal for this discussion. Figure 13, taken from McDaniel, 1964, shows, (a) the potential barrier and the conduction electron energy levels when the ion is at infinity, and (b) the resulting potential energy diagram when the ion is within a few angstroms of the metallic surface. Noted on the diagram are the work function ( $\phi$ ), the conduction band depth ( $\epsilon_0$ ), the ionization potential of the ion ( $V_i$ ), the distance of the ion from the surface ( $S$ ), and the energy levels of electron 1 ( $\alpha$ ) and electron 2 ( $\beta$ ). There is a probability that an electron will tunnel through the potential barrier directly to the ground state of the ion, giving its excess energy to another conduction electron. If electron 1 were to neutralize the ion in this way, giving its excess energy to electron 2, the resulting kinetic energy of electron 2 outside the metal would be given by  $V_i - \alpha - \beta$ . The maximum kinetic energy thus obtained, occurring for both electrons very near the Fermi energy, would be  $V_i - 2\phi$ . Therefore, the process is energetically possible only when  $V_i > 2\phi$ . For lower ionization potentials, neutralization could occur but without the associated secondary ejection. It has been noted by Angel et al., 1961, that the relative photoelectric spectral response of the Bendix channel multiplier material is similar to that of tungsten, implying a work function of about 4.5 volts. The hydrogen ionization potential being 13.6 volts, we conclude that the requirement ( $V_i > 2\phi$ ) for secondary emission by direct Auger neutralization is probably satisfied for



protons incident on the channel multiplier surface. As the ion kinetic energy is increased, the resulting potential barrier will on the average be narrower, enhancing the possibility of potential ejection. However, as the velocity is further increased, the ion will spend less time near the surface, decreasing the probability that a conduction electron will tunnel through the potential barrier in a given encounter, thereby accounting for the confinement of this effect to the lower ion energies.

At higher ionic kinetic energies, kinetic ejection occurs with a large probability, the main process being ionization of target atoms. The maximum depth from which secondaries can escape is on the order of  $10^{-6}$  cm, which is only a small fraction of the penetration depth of energetic (several kev) incident ions. Therefore, one can consider the interaction due to ions with their full primary energy. Using Bethe's formula for the ionization cross section in the energy range 1 kev to 100 kev (Mott and Massey, 1965), Sternglass, 1957, arrived at an expression for the secondary yield,  $\delta$ , of the form,

$$\delta \propto \frac{z_i^2}{E_o} \left\{ \frac{ZM}{E_i} \ln \left( \frac{4 m_o E_i}{\bar{I} M} \right) \right\}, \quad (22)$$

where,

$M$  = ionic mass,

$m_o$  = electron mass,

$E_i$  = incident ion energy,

$Z$  = atomic number of target atoms,

$E_o$  = mean energy loss per collision,

$\bar{I}$  = mean excitation potential.

$\bar{I}$  is defined by,

$$Z \ln \bar{I} = \sum_{n,l} Z_{nl} \ln I_{nl} \quad (23)$$

where  $Z_{nl}$  is the number of electrons in the (nl) shell and  $I_{nl}$  is their binding energy. The atomic shells which participate depend on the ion's velocity, the lower velocity ions interacting only with outer shell electrons. The threshold for the kinetic process is roughly proportional to the ionic mass, being about 100 ev for the lighter ions. The secondary yield will have a peak at an ionic energy which is proportional to the ionic mass and is on the order of some kilovolts for the lighter ions. If the yield is expressed as a function of ion velocity, it becomes independent of ion mass for a given charge state and material.

Finally, secondary emission due to photon impact is a source of background in the present experiment. The quantum efficiency of Bendix channel multipliers for photons has been determined experimentally by Johnson and Svenson, 1965. The chief process in the energy range of channel multiplier sensitivity is photoelectric emission for which the work function, as noted above, is similar to that of tungsten.

For most materials the maximum secondary yield for incident electrons will have a value from slightly less than one to about ten secondaries per incident primary (see Bruining, 1954). Concerning the channel multiplier emitting surface, we can only assert that  $\delta_{\max}$  must be greater than unity for the observed multiplication process to occur. Furthermore, since the channel multiplier will function over a wide range of operating voltages, the secondary

emission yield must be greater than unity over a fairly large interval of electron energies. An estimated value of 5 secondaries per primary for  $\delta_{\max}$  should not, therefore, be too much in error. Further evidence for this approximate value is suggested by the following simple approach. Typical current gains of  $5 \times 10^7$  have been measured by us at an operating voltage of about 3500 V. If the average energy gained by the secondaries between encounters with the wall is near that for the estimated maximum yield of 5, then the observed gain would require that the channel multiplier be equivalent to eleven stages of multiplication. Since the 3500 V potential should be distributed uniformly along the length of the channel, the average energy attained by each secondary should be in the neighborhood of 350 ev. Experimental measurements by Frank, 1965, of the channel multiplier counting efficiency as a function of primary electron energy indicates a maximum near this energy. Therefore, to a first approximation, channel multiplier gain is determined by the operating voltage, reaching a maximum when the average energy attained by the secondaries corresponds to that for which  $\delta = \delta_{\max}$  for the emitting material.

The actual operation is, however, somewhat more complicated, especially near the maximum gain. It was first noted by Evans, 1965, that the channel multiplier could be operated in a saturated gain mode. That is, while operating voltages of 1000 - 2000 V result in a pulse height distribution which is very broad and rising toward lower pulse heights, when the operating voltage is increased to 3000 - 4000 V with gains of more than  $10^7$ , the

pulse height distribution becomes sharply peaked. This behavior is attributed to a gain limiting process occurring as a result of the electron cascade. As discussed by Schmidt and Hendee, 1966, the saturation effect is probably caused by the electron space charge which exists inside the channel during a cascade. Due to such a space charge, an electron emitted from the channel multiplier wall will experience a radial repulsive force tending to shorten its time of flight, thereby decreasing the energy which it attains between encounters. Eventually this average acceleration will decrease to the point that the incident energy corresponds to a  $\delta$  of unity. Thereafter no further multiplication can occur and the magnitude of the cascade becomes saturated. This effect is fortuitous for experiments employing a pulse counting method in which there will always be a minimum pulse height such that a pulse of lower amplitude will go unrecorded. In principle then, the discrimination level can be set somewhat below the sharply peaked pulse height distribution, avoiding significant loss of pulses. If the count rate is low enough such that another cascade is not initiated until the space charge of the previous count has cleared the channel and the emitting surface has recovered from the net positive charging which it has experienced, very accurate pulse counting is possible. However, for higher count rates the effect of residual space and surface charge will be to limit the gain at a lower level. For example, there will be more space charge present after a given amount of multiplication. Therefore, if the count rate is constant but high enough so that these effects occur, we should still expect a peaked pulse height distribution

but a lower average pulse height. Moreover, if the count rate is rapidly varying we should then expect a broadening of the pulse height distribution. These effects may be accounted for by simply assigning a dead time to the channel multiplier - amplifier combination which is approximately equal to the average time between pulses at which the mean pulse height falls below the amplifier threshold. The experimental determination of this dead time will be discussed in the section on SPECS calibration. Theoretical calculation of the count rate at which dead time effects become important is complicated by the phenomenon of ion feedback, which occurs for high channel multiplier operating voltages. The large electron cascade near the collection end will ionize any residual gas and the positive ions will drift up the tube due to the axial electric field with some probability of striking the wall and initiating other cascades. This effect is known to occur at laboratory pressures as low as  $10^{-6}$  mm Hg. Ion feedback contributes to the gain but also tends to lengthen the rise and decay times of the output pulse. Such feedback is not important at the Aurora 1 altitude, where pressures are on the order of  $10^{-10}$  mm Hg.

To a first approximation, the channel multiplier counting efficiency as a function of primary energy for low input fluxes should closely resemble the secondary yield curve for the emitting material. However, the gain saturation effect should tend to flatten the response curve in the region  $\delta > 1$ . As mentioned above, Frank, 1965, has experimentally determined the counting efficiency of the Bendix channel multiplier as a function of primary energy

for electrons and  $\text{Li}^+$  ions. We will adopt the electron curve as reported by Frank (see Figure 14). However, in the absence of experimental data on proton efficiency, we must attempt to correct the  $\text{Li}^+$  relation for the ionic mass difference. It has been determined theoretically (Stern-glass, 1957) and experimentally (Ploch, 1951) that secondary emission by kinetic ejection for a given material depends only on the ion charge and velocity. Since the ionization potential of  $\text{Li}^+$  is only 5.39 V and the estimated work function of the channel multiplier emitting material is 4.5 V, the criterion for potential ejection ( $V_i > 2\phi$ ) is not satisfied. Therefore,  $\text{Li}^+$  can produce secondaries in the channel multiplier only by kinetic ejection. There are two difficulties in attempting a straightforward correction of the  $\text{Li}^+$  efficiency curve to protons. First, the ionization potential of  $\text{H}^+$  (13.6 V) does satisfy the potential ejection criterion. However, experimental work on potential ejection has only been performed for noble gas ions, which have the largest ionization potentials, incident on metals, which have many conduction band electrons (Hagstrum, 1954). We would expect the process to be much less efficient in the case of  $\text{H}^+$  incident on a semiconductor. Therefore, in the absence of experimental data and with the above justifications, we shall assume that the contribution of potential ejection in the present experiment is negligible. The second problem arises since the Bethe formula for the ionization cross section is strictly valid only for energies  $\geq 1$  kev. However, the kinetic ejection process, when energetically possible, should depend only on ionic charge and velocity. Therefore, we will correct Frank's

curve for channel multiplier counting efficiency for  $\text{Li}^+$  to protons, as shown in Figure 15, by correcting the proton energy axis for the mass difference ( $M_{\text{H}^+} = \frac{1.008}{6.940} M_{\text{Li}^+}$ ).

#### D.2. Physical Analyzer and Associated Electronics.

In the SPECS instrument, energy analysis of an incoming beam of charged particles is accomplished by electrostatic deflection. The analyzer geometry is shown in schematic form in Figure 16. A particle incident on the SPECS aperture from a direction lying within the look angle defined by the three collimating baffles will enter the region between the deflection plates. The plate nearest the funnel channel multiplier is maintained at ground potential while the voltage on the other plate is switched once every 0.5 second through the following succession of voltages: +35 V, +350 V, +3500 V, +350 V, +35 V, -35 V, -350 V, -3500 V, -350 V, -35 V. At a given plate voltage, particles of one polarity will be directed toward the funnel channel multiplier while those of opposite polarity will be deflected into the array of five  $270^\circ$  channel multipliers. The angle through which each particle is deflected will depend on its energy per unit charge. In a complete cycle of plate voltage nominal energy per unit charge passbands as shown in Figure 17 are sampled, thus generating an eighteen-point spectrum for electrons and protons (ignoring the contributions of other ions). The exact passbands for the Aurora 1 instrument will be given in the section on SPECS calibration. Note that certain internal consistency checks are made available by the chosen geometry. For example, comparable energy ranges are sampled by Channel 6 and channels 2 - 4

for plate voltages of opposite polarity, and by Channel 5 and channels 1 - 3 at successive voltages of the same polarity. These nominal energy passbands are the result of approximate calculations, neglecting fringing fields, and preliminary experimental tests with a breadboard of adjustable geometry. The essential characteristics of these passbands, as regards total energy range and internal consistency checks, are achieved by the SPECS flight model.

The combination channel multiplier constant power supply and switching deflection plate supply for the Aurora 1 SPECS was built by Analog Technology Corporation. Having a weight of 820 gm and a volume of  $525 \text{ cm}^3$ , this supply dissipates an average power of 505 mw. The switching time for each level is less than 8 msec with a peak to peak ripple of less than one volt appearing at the deflection plate. A constant 3500 V (positive) is delivered to the channel multiplier array with a ripple of 50 mV. The power supply is driven externally by a 2 cps payload clock, so the deflection plate voltage level is changed once every 0.5 second. See O'Brien et al., 1967 for a more complete description of its operation.

The channel multipliers are operated in the gain saturated mode, as described above, resulting in an approximately equal charge output for each particle counted. The charge pulses are ac-coupled into charge sensitive preamplifiers which effect their conversion to voltage pulses appearing at the input to a differential amplifier discriminator. The charge level which the channel multiplier outputs must exceed for a pulse to be counted is determined by



the feedback capacitance of the charge sensitive preamplifier and the biasing of the differential amplifier. A Complementary driver at the discriminator output completes the conversion of the charge pulse to a 7 V - 0 V negative going pulse with rise and fall time less than 200 nanosec and pulse width of about 2 microsec. This output pulse is delivered directly to the scaler circuitry and thence on to the satellite telemetry. Whereas the funnel channel multiplier (Channel 6) is sampled continuously, due to telemetry limitations channels 1 through 5 are subcommutated. The switching logic is driven by a 10 cps payload clock, resulting in a sample time of 0.1 second per channel. The subcommutation is accomplished by disabling the inputs to four of the discriminators and summing all five outputs. A block diagram of the SPECS electronics is shown in Figure 18.

#### D.3. SPECS Calibration.

A laboratory calibration that is accurate and as extensive as time and other limitations allow is essential for the interpretation of the output of a space-borne particle detector such as SPECS. The charged particle information which we hope to gain with such an experiment includes their number, velocity, and angular distribution with respect to the local geomagnetic vector. Ideally, one should like to place the detector in every type of radiation environment which might be encountered during its useful lifetime in orbit, thereby identifying each particular response with a given set of conditions. Such a procedure is, of course, impractical, the usual approach being a selective one by

which the most germane aspects of the instrument's operation are tested explicitly, laying a solid empirical basis for generalizations concerning its other functional details. Following this general philosophy, our basic calibration procedure involved a determination of sensitivity as a function of particle energy and incidence angle.

A uniform, four-inch diameter, monoenergetic electron beam of adjustable energy and intensity was used for the measurement of the energy passbands and angular response of the Aurora SPECS in its final flight configuration. The electron beam is generated by accelerating photoelectrons ejected from a twelve-inch diameter aluminum plate which is illuminated with ultraviolet light mainly at the 2537 Å line of mercury. The accelerating potential is applied between the aluminum plate and a four-inch diameter grounded screen which serves as the exit aperture. Between the grounded screen and the aluminum plate, and connected at equal voltage intervals along a resistive divider, are eleven concentric aluminum rings with inside diameters of ten inches. The resulting electron beam is uniform within a factor of two over its diameter and is nearly monoenergetic with energy variable up to 30 keV. An experimental verification of the narrow energy spread is shown in Figure 19, where relative beam current is plotted versus retarding voltage for a retarding grid oriented perpendicular to the beam. No magnetic shielding is employed, so the low-energy limit to the usefulness of the beam is determined mainly by the perturbation due to the earth's magnetic field, becoming more important below about 200 eV.

The usual procedure was to maintain a constant beam energy while varying the angle of incidence with a motor-driven angular sweep fixture to which the SPECS was mounted. The pivot for this angular variation was at the front SPECS aperture, hence the same portion of the beam was sampled during the entire angular sweep. The angular response was measured chiefly in the plane of the channel multiplier array, that is, over the smaller acceptance angle. Several measurements over the larger angle revealed a nearly constant (within a factor of two) response over the  $20^\circ$  acceptance angle at a given beam energy. Moreover, for a given channel the relative response over this larger angle was almost identical for all energies within the energy passband. Subsequent changes in beam energy resulted in a set of angular response curves such as shown in Figure 20. Due to the uniform count rate over the large acceptance angle, the total response to an isotropic monoenergetic beam will be approximately proportional to the integrated response over the smaller acceptance angle. We have assumed that this proportionality is exact and have numerically integrated the angular response curves for the applied beam energies, thus generating the experimental curves of relative response to an isotropic beam as a function of electron energy shown in Figure 21. We define the minimum and maximum of the energy passband for each channel as the energy for which the integrated response is 10% of maximum. Similarly, the acceptance angle limits are defined as those angles at which the peak response occurred for the minimum and maximum energies. These calibrations were carried out at fairly low count rates of a few thousand counts per second, thereby avoiding significant saturation effects. The

energy passband and angular response calibration is potentially very accurate and hence affords us our best knowledge of the SPECS operation. However, we should note that the 10% energy passbands were measured with a flat input spectrum, that is, with equal intensity at all energies. Actually, the effective passbands will depend on the input spectrum, a steep spectrum rising toward lower energies resulting in a passband which is likewise shifted toward lower energies. This effect is, of course, of greatest import for the wider passbands of channels 5 and 6.

Whereas, the above calibration procedure has yielded fairly accurate information concerning the range of energies and incident angles which are sampled by each SPECS channel, we should like to know as accurately as possible the absolute number of impinging particles within the energy bands and angular sectors sampled. An absolute calibration is made very difficult by the rather complicated geometrical configuration of the SPECS analyzer and compounded by the variation of channel multiplier response as a function of electron and proton energy. We should note at this point that the latter problem has been ignored in the determination of the energy passbands since for a given channel the variation in efficiency is automatically accounted for in the calibration procedure while the variation over the total range has been nullified by the normalization process. We have approached the problem of absolute calibration in two ways, each of which is beset by several uncertainties. The first of these involves an approximate calculation of the total geometric factor in light of the available calibration data, while the second

was conducted by introducing an isotropic electron beam from a  $\text{Ni}^{63}$   $\beta$ -source about which the theoretical energy spectrum and the total intensity are known.

The first method is based on the fact that the geometric factor (the number which, when divided into the detector output in counts/sec will give the total number of particles in a unit energy interval which are incident on a  $1 \text{ cm}^2$  area through a solid angle of 1 steradian) is determined chiefly by the solid angle which is viewed, the effective area of the counting device, and its efficiency for counting the particles of interest. The geometric factor is a function of particle energy, but if it can be found for a given energy in a certain channel, a total geometric factor for that channel can be arrived at through the previous measurement of relative response versus energy. Since we have fairly accurate measurements of solid angle response at our disposal and we know the channel multiplier efficiency as discussed in the previous section, it remains only to determine the effective sensitive area for each channel.

In this treatment, we wish to find the expected geometric factor for each channel by considering a certain energy, in particular the energy of maximum response. Whereas, the acceptance angle for a beam composed of all energies within the measured passband of the channel is somewhat larger than that for the energy of maximum response, it is the latter which should concern us in this calculation. The angular response thus defined is typically about  $3^\circ$  in the plane of the channel multiplier array for one

of the  $270^\circ$  channels (Channel 6 will be considered later). Concentrating for the moment on the configuration in this plane, one can show geometrically that if the divergence of the beam throughout the deflection is determined only by the spread in incidence angle, at the distance of the channel multiplier array all particles entering within  $3^\circ$  of the axis through the area defined by the smallest aperture can be counted by a 1 mm diameter sensor. We have assumed of course a constant deflection angle for all incidence angles. Therefore, in this plane the geometric factor will be determined by the acceptance angle and the width of the rear aperture. In the plane perpendicular to the channel multiplier array, the angular part of the geometric factor will again depend on the measured acceptance angle but the pertinent distance will be the channel multiplier inner diameter. Thus, for the energy of maximum sensitivity, each  $270^\circ$  channel will have a geometric factor given by,

$$g = \epsilon A \Omega \text{ cm}^2 \text{ ster},$$

where,  $\epsilon$  is the counting efficiency at the energy of peak response as deduced from Figures 14 and 15,  $\Omega$  is the acceptance solid angle, given approximately by,

$$\Omega \approx \int_{\theta=0^\circ}^{3^\circ} \int_{\varphi=70^\circ}^{90^\circ} \sin \varphi \, d\varphi \, d\theta = .018 \text{ ster.}, \quad (24)$$

where,  $\theta$  is the small angle and  $\varphi$  the large angle, while  $A$  is the sensitive area,

$$\begin{aligned} A &= (\text{width of rear aperture}) \cdot \\ &\quad \cdot (\text{channel multiplier diameter}) \\ &= 4.3 \times 10^{-3} \text{ cm}^2. \end{aligned} \quad (25)$$

Hence,  $g \approx \epsilon(7.74 \times 10^{-5}) \text{ cm}^2 \text{ ster}$ . In order to calculate the total geometric factor for a given channel, an energy factor must be included. We will accomplish this by simply finding the average value,  $\eta$ , of the normalized response curves of Figure 21, multiplying  $g$  by this factor and the energy passband in ev. The resulting total geometric factor will thus be given by,

$$G = \eta \epsilon A \Omega(\Delta E) \text{ cm}^2 \text{ ster ev.} \quad (26)$$

The results of this calculation for each of the five 1 mm diameter channels are given in Figure 22.

For the case of Channel 6, the principal area limitation in the plane of the sensor array is again the width of the smallest aperture, but the acceptance angle at the energy of maximum sensitivity is slightly larger, being limited mainly by aperture vignetting rather than channel multiplier edge effects as in the case of the smaller channels. In the other plane, the limiting area dimension is the 8 mm cone diameter, the acceptance angle remaining about  $20^\circ$ . Calculations of the Channel 6 geometric factor resulted in the values given in Figure 22.

The other method, that is, using an isotropic continuous  $\beta$ -source, was also performed but an accurate interpretation of the results must await experimental measurement of the  $\text{Ni}^{63}$  energy spectrum. While the theoretical energy spectrum of the source is known, the effects of scattering within the source have not been assessed completely. Therefore, we consider the calculated absolute geometric factors to be the most reliable at this time.

As mentioned in Section D.1., there is an inherent channel multiplier - amplifier dead time during which successive pulses will not be counted. The effect of this finite resolving time is an apparent count rate that is lower than the true count rate except where the interval between all pulses is greater than the dead time. The channel multiplier and its amplifier comprise a system of the paralyzable type. That is, only those intervals longer than the dead time,  $\rho$ , can be counted. Hence, for sufficiently high count rates the output will be decreased to zero, or be "paralyzed". If the statistical fluctuations of the true counting rate are describable by a Poisson distribution, and if the average true count rate is  $N$ , then the probability that no counts will be observed during a time interval  $t$  is given by,

$$P_0 = \frac{(Nt)^0}{0!} e^{-Nt} = e^{-Nt}. \quad (27)$$

The probability that a given interval between counts will be in the range  $t$  to  $t + dt$  is,

$$dP = N e^{-Nt} dt. \quad (28)$$

Therefore, the probability that a given interval will be longer than the dead time,  $\rho$ , is given by,

$$\begin{aligned} P_{\Delta t > \rho} &= \int_{\rho}^{\infty} N e^{-Nt} dt \\ &= e^{-N\rho}. \end{aligned} \quad (29)$$

The observed count rate for a true count rate of  $n$  counts per second should then be,



$$n = N e^{-N\rho}. \quad (30)$$

Differentiating eq. (30) with respect to  $N$  indicates a maximum to the observed counting rate,  $n$ , when  $N\rho = 1$ , that is,

$$n_{\max} = \frac{1}{e\rho}. \quad (31)$$

If we can establish that the SPECS channels do, indeed, obey such a law, and further that  $\rho$  for our counters is independent of  $N$ , then a measurement of the maximum attainable count rate for each channel is all that is required to determine the relation between true and apparent count rate. Note that the function of eq. (30) is double-valued in  $N$ , so that we must decide in each case whether  $N$  is greater or less than  $1/\rho$ .

Using the electron beam described in the previous section, we were able to achieve the maximum count rates in channels 1, 2, 3, and 6. Additionally, we performed an experimental measurement of true vs. apparent count rate for all channels up to the maximum beam currents attainable. Using the dead time obtained by inserting the observed  $n_{\max}$  into eq. (31) for channels 1, 2, 3, and 6, the predicted relationship of eq. (30) can then be compared with that found experimentally over the sampled range. If the predicted and observed relations coincide, we should, with some confidence, be able to apply the relation of eq. (30) to the entire range of count rates encountered in the flight. The value of such a theoretical relationship is emphasized by the fact that channel multiplier gain is

somewhat dependent on operating pressure and total accumulated counts. Any change in gain will tend to change  $\rho$  by altering the fraction of pulses which fall below the amplifier discrimination level. However, if the relation of eq. (30) is found to be satisfied, then a determination of  $n_{\max}$  from the flight data is all that will be required to correct the true versus apparent count rate relation for the current conditions.

The experimental true versus apparent count rate curves were measured by the following procedure. The electron beam was directed at normal incidence into the front SPECS aperture. Initially, a low beam current was generated and for a given channel an electron energy close to one edge of the energy passband was applied. Varying the energy up to the energy of maximum sensitivity resulted in a response curve similar to the lower curve of Figure 23. The beam current was subsequently increased to its maximum value (approximately a factor of ten more intense than that of the first run) and a similar procedure followed. A curve such as the upper one in Figure 23 resulted. We made the initial assumption that there are no saturation effects below a given level, noted by  $n_{21}$  on the upper curve, i. e.,  $n_{21} = N_{21}$  (see Figure 23). Necessarily then, we have  $n_{11} = N_{11}$  and the ratio of the beam intensities for the two trials should be given by  $n_{21}/n_{11}$ . Therefore, at each energy we should have,

$$N_{2i} = \frac{n_{21}}{n_{11}} N_{1i}. \quad (32)$$

Using this relation, we correct the apparent count rates of the upper curve ( $n_{2i}$ ) up to that value of  $i$  for which  $n_{1i} = n_{21}$ . The partial true versus apparent count rate curve which has been generated is then used to correct the next section of the lower curve. The same procedure is followed again until the entire upper curve has been corrected to true count rates. In practice, however, there is a background effect such that a number of the initial counts will not be multiplied by the beam increase factor, but instead will remain constant. Because of this, a correction was necessary to satisfy the requirement  $n \leq N$ . This correction was small compared to the count rates considered.

An example of the results of this procedure are shown in Figure 24 for the case of Channel 1. The background correction was introduced by initially subtracting a constant 200 counts/sec from both curves. Taking a value for  $n_{21}$  of 5400 counts/sec ( $\sim 0.1 n_{\max}$ ), the values plotted in Figure 24 were obtained. The solid line is the theoretical curve obtained by inserting the value of  $\rho$  obtained from  $n_{\max} = \frac{1}{e\rho}$  into eq. (30). Comparable agreement was obtained for channels 2, 3, and 6. The relations between  $n$  and  $N$  for channels 4 and 5, which were not driven to  $n_{\max}$  by the available beam current, were obtained in a slightly different manner. After introducing a background correction as described above, the dead time was determined by approximating the exponential term in eq. (30) by the first two terms in the infinite series, i. e.,

$$n \approx N(1 - N\rho), \quad N\rho \ll 1, \quad (33)$$

which is valid within 10% for  $N\rho < 0.4$ . Using the ratios of beam intensities,  $n_{21}/n_{11}$ , and inverting eq. (33), we should have,

$$N_{1i}(1 + n_{21}/n_{11}) = n_{2i}(1 + n_{2i}\rho). \quad (34)$$

The value of  $\rho$  thus obtained is used in eq. (30), which is compared again to the experimental points. The theoretical  $n$  versus  $N$  relations which we will use to correct for dead time are given for all channels in Figure 25. An unfortunate yet important point arises here. Eq. (30) is non-linear in  $N$  and cannot be solved analytically for  $N$ . Therefore, when it is necessary to correct count rates in the flight data, we shall make use of the approximation,

$$N \approx n(1 + n\rho), \quad (35)$$

whenever  $N\rho < 0.4$  (guaranteeing 10% accuracy). For higher count rates, an iterative process, employing the above approximation as a starting point, will be used.

In addition to the particles which the SPECS instrument is designed to detect, there are other sources of counts which may be classified as background. The two most obvious causes of spurious counts are contamination by ultraviolet radiation and penetrating particles.

Measurements of the SPECS ultraviolet rejection ratio have been conducted at Rice and at Bendix Research Laboratories. The results are still in preliminary form, but indicate a rejection factor of about  $10^{-6}$  for Channel 6, representing the worst case. The most important ultraviolet

radiation encountered by the satellite is the 1216 A Lyman Alpha line of hydrogen produced by the sun and resonantly backscattered by the hydrogen in the earth's atmosphere. Virtually all the backscattered Lyman Alpha, or geocorona, will originate below the satellite altitude, so that after orientation, in the northern hemisphere, the only important source of ultraviolet contamination should be the sun. Bendix has measured the quantum efficiency of their channel multipliers to be about 1.8% at 1216 A. The average solar output of  $L_{\alpha}$  being about  $5 \text{ ergs cm}^{-2} \text{ sec}^{-1}$  or  $3 \times 10^{11}$  photons  $\text{cm}^{-2} \text{ sec}^{-1}$ , maximum counting rates of about 5000 counts/sec should result when the detector is pointed directly at the sun. On the other hand, the geocorona should cause less than  $\sim 1$  count/sec of background.

Energetic primary particles will cause background counts by either producing bremsstrahlung X-rays in the detector or satellite walls or penetrating directly through to the channel multipliers. In an effort to reduce this effect, the shielding afforded by the lightweight magnesium of the detector and satellite structures was supplemented by a .100" thickness of lead which was affixed to the top and sides of the SPECS analyzer section. Thus, a total shielding of about  $3 \text{ gm cm}^{-2}$  was effected. Background due to cosmic rays and other sources present in the laboratory was measured to be less than 0.1 count/sec for channels 1 - 5 and less than 0.5 count/sec for Channel 6. A more thorough analysis of the actual problems caused by these background sources will be given when they affect the flight data presented herein.

Before proceeding, we should mention that Arnoldy (see Hoffman and Evans, 1967) has measured the absolute counting efficiency of the Bendix channel multiplier in a limited energy range (~100 ev to 2 kev) with results somewhat at variance with those of Frank, 1965, which we have chosen to use due to their wider energy range of applicability. Arnoldy's curve is shown in Figure 26. In the section on experimental results, we will discuss this source of potential error as it applies to our reported observations.

### III. EXPERIMENTAL RESULTS

#### A. Satellite Performance.

All satellite systems operated satisfactorily in a real-time mode from launch on June 29, 1967, until August 11, 1967, with periodic cutoffs for recharging initiated by the battery voltage monitor. The extended charging period which began on August 11 may have been caused by radiation damage to the solar cells during transit through the inner Van Allen zone. Data transmission resumed for one day on October 11, 1967, when the earth's motion about the sun had resulted in a maximum sunlight, dawn-dusk orbit. The operation of the satellite at this time was much the same as that at time of cutoff, indicating that the battery charge level was probably the only factor contributing to the extended data gap.

As discussed in Section II.C., magnetic orientation was successfully achieved in about two weeks, the maximum deviation of the bar magnet from the geomagnetic vector being less than  $\sim 15^\circ$  after that time. We note, however, in Figure 7 that there was a three-day data gap during the period of most rapid orientation. Examination of the output of the quadrant photometer, which is sensitive to the sun and the sunlit earth, verifies that orientation did in fact occur. The predicted spin period (Section II.C.), assuming complete despin after launch, was longer by approximately a factor of two than the observed period. However, a clear latitude dependence of spin period was observed as predicted as well as an initial decrease of

period with time until the maximum deviation from the geomagnetic vector became consistent with that required for sinusoidal motion. The spin period as deduced from the subcommutated magnetometer output and the ultraviolet and visible photometer periodicities was initially about 70 seconds, decreasing to about 40 seconds as orientation was approached.

Data from the SPECS charged particle detector were available throughout all periods of satellite transmission. Channel 6, which experienced relatively high counting rates (up to 100 kc/sec) produced useful data for the first eight orbits. Its short lifetime is attributed to channel multiplier gain loss as a function of total accumulated counts. Channels 1 - 3 were active for approximately 100 orbits, while channels 4 and 5 produced good data for all periods of satellite transmission, that is, through the 864th orbit. The failure of these channels, while being of some concern in the design of future payloads, did not seriously affect the usefulness of the subsequent data as related to this thesis. Channels 4 and 5 with the six deflection voltages provide six-point spectra for both electrons and protons.

#### B. Data Acquisition and Reduction.

Aurora 1 orbit information is provided by the U. S. Navy Space Surveillance Systems while data reception was conducted by NASA STADAN stations at the following locations: College, Alaska; Ororal, Australia; Winkfield, England; Madagascar; Rosman, N. C.; Quito, Ecuador; Ft. Meyers, Fla.; Johannesburg, S. Africa; and Santiago, Chile.



Private receiving stations at Tromso, Norway and at Rice University also participated. The most extensive coverage was that by the College STADAN station, with the Winkfield and Tromso stations providing valuable data near  $0^{\circ}$  longitude. All stations recorded the satellite's data transmission as well as the NASA 36-bit time code, with the STADAN stations recording in addition a Serial Coded Digital Time code. The orbital information is available for each minute of Universal Time, thereby providing a convenient conversion from the recorded time to the satellite location in terms of altitude and the longitude and latitude of the subsatellite point.

The charged particle data presented herein are referenced to the satellite position in the geomagnetic field by specifying the L parameter each minute and the magnetic local time each five minutes. The L values are obtained from McIlwain's computer program (McIlwain, 1961) which is based on the Jensen and Cain 48-term expansion of the earth's quiet field. The magnetic local time is defined by the angle between the magnetic meridians passing through the subsatellite point and the subsolar point, magnetic noon (MLT = 12.0) occurring when this angle is zero (Vegard, 1912).

A sample of the Aurora 1 analog data is shown in Figure 27. Whereas, in principle this type of data can be digitized with an appropriate multiplexing system, the frequent noise spikes and ripple which appear on the data tapes render the cost of the analog to digital conversion system impractical. Therefore, the data are read

manually from strip charts and punched onto computer cards. Further data manipulation, plotting, etc., is accomplished with the Rice University IBM 7040 computer, along with an SDS 92 computer and a California Computer Products Automatic Plotter.

### C. Typical Characteristics of Electron Fluxes Observed at High Latitudes.

During the first few days of orbit, the Aurora 1 SPECS was sampling a large range of pitch angles due to satellite tumble and was thus suitable for determining the typical charged particle energy spectra and pitch angle distributions as functions of position along the orbit. We will herein confine our attention to the high-latitude ( $L > 4$ ) portions of the flight, for which the observed charged particles will be considered as more or less directly connected with some type of auroral phenomena.

#### C.1. Response of Channel 6 in the Polar Regions.

The properties of the observed high-latitude particle radiation that persist on the average for all orbits analyzed to date are in fact represented quite well by the output of Channel 6 during the first few orbits. Certain special cases will be considered later, but the data presented in this section are to be taken as typical of the average properties of the polar charged particle population. We have chosen Channel 6 because its output is transmitted continuously, thereby avoiding complicated decommutation procedures, and because its relatively wide passbands allow

more complete coverage of the energy range of interest with a three-point spectrum. Of course, such a sample is apt to disguise some of the spectral details, but these will be resolved for the areas of interest in a succeeding section. Moreover, in each case, channels 1 - 5 are investigated for the internal consistency checks which they afford. That is, the sum of the outputs of these five channels at a given deflection voltage is compared to the Channel 6 output at a deflection voltage of the same magnitude but of opposite polarity as a test for instrument malfunction or inadequate performance.

In figures 28, 29, and 30 the response of Channel 6 during typical passes through the polar regions is plotted versus Universal Time and L, with magnetic local time indicated periodically (see Burch, 1968). Counting rates plotted are 0.5-second averages obtained at 5-second intervals. Also shown are pitch angle ranges based on the subcommutated magnetometer output which was transmitted once every 16 seconds.

Above  $L \sim 4.5$  there typically are three distinct zones of electron precipitation:

- (1) An "auroral zone,"
- (2) A "soft zone,"
- (3) The "polar cap."

The spatial coincidence of the first zone with the region of most frequent auroral activity and the appreciable fluxes of electrons in the energy range 6200 ev - 25,000 ev (see Evans, 1967a; Westerlund, 1968) are the motivations for using the name "auroral zone". This region is

characterized by (a) relatively hard electron spectra, and (b) a tendency toward isotropy except near  $\alpha = 180^\circ$  (northern hemisphere) or  $\alpha = 0^\circ$  (southern hemisphere) where an intensity decrease is usually observed in the two higher energy channels due to atmospheric scattering and absorption.

The soft zone noted in figures 28, 29, and 30 is typified by (a) much softer electron spectra, and (b) rapid variations in intensity which are most evident in the lowest energy channel. We note that due to limited time resolution and rapid motion across L shells, it is difficult to distinguish between spatial, temporal and pitch angle anisotropies, so that it is impossible to conclude from these figures whether the soft zone pitch angle distribution differs from that of the auroral zone. The soft zone extends from the point of spectral softening at the auroral zone boundary poleward to the latitude at which the count rate in the highest energy band falls below threshold (8 counts/sec) and those of the other two bands decrease to the levels which persist across the geomagnetic pole. Analysis of approximately 30 passes indicates that whereas the very sharp high-latitude termination of electron fluxes seen in Figure 30 does not occur on every pass, it is a typical feature, especially near the midnight meridian.

The segment labeled polar cap in Figure 30 shows the typical response of Channel 6 between the soft zone and the geomagnetic pole. Electron fluxes in the two lower energy bands are relatively uniform in this region, remaining a factor of 10 to 100 below those in the soft zone. The

response in the highest energy segment is below threshold over the polar cap except for statistical variations and occasional contamination by solar ultraviolet radiation (see Section II.D.). We will not consider the polar cap region further except in noting the very weak fluxes which are encountered there, since due to much smaller geometric factors, count rates of statistical significance are not obtained in channels 1 - 5 in the polar cap region and data are not available for Channel 6 beyond the eighth orbit. We should note, however, that the characteristics of the particle radiation that does exist over the polar cap are of great importance and future experiments should be designed in view of the approximate fluxes indicated in Figure 30 with the vertical axis divided by the Channel 6 physical geometric factor ( $\sim 10^{-4} \text{ cm}^2 \text{ ster}$ ).

### C.2. Diurnal Variation of Northern Hemisphere Particle Fluxes.

Due to unfavorable receiving station locations, southern hemisphere coverage does not usually include the complete soft zone. Therefore, we use only northern hemisphere passes in Figure 31. In this figure a few northern hemisphere passes which occurred on June 30, 1967, are plotted as functions of magnetic local time and the invariant latitude at which the magnetic field line passing through the satellite would ideally intersect the earth's surface. That is,  $\Lambda = \cos^{-1}(L^{-\frac{1}{2}})$  (O'Brien et al., 1962), where L is given in earth radii. Since the motion of the earth about the sun is only about  $1^\circ$  during a single day, all these passes occurred at essentially the same geographic

local time with the tilt of the earth's equivalent dipole being responsible for the magnetic local time spread. The dotted lines represent those regions where auroral type electron spectra were observed while the solid lines indicate the presence of electron fluxes characteristic of the soft zone as described above. These passes occurred during times for which the three-hour  $K_p$  values ranged between 2 and 4 with a daily sum for June 30, 1967, of 22. During such a moderately disturbed period, greatest auroral activity usually occurs near the spatial center of the average auroral oval (Akasofu, 1965). In Figure 31, the shaded area represents the region of 70% probability of occurrence of visual auroras near zenith during a thirty-minute interval based on observations over a two-year period (Feldstein, 1966). The dashed line in Figure 31 indicates the average location at which fluxes of electrons at pitch angles close to  $90^\circ$  and energies above 35 kev dropped to cosmic ray background over 300 passes of Alouette 2 from December, 1965, to July, 1966 (McDiarmid and Burrows, 1968). The Alouette observations are averaged over seasonal variations and a wide range of  $K_p$  values.

We should emphasize that the dotted line in Figure 31 is not to be viewed as the boundary of stable trapping, in the sense that electrons of energies higher than 35 kev can bounce from hemisphere to hemisphere and drift around the earth for invariant latitudes below this line. This is especially so for the day side in view of the large diurnal variation of the "trapping boundary" (see Section I.D.). It should instead be considered as the boundary below which electrons can attain such energies, with the stable trapping

boundary occurring at a somewhat lower latitude (see McDiarmid and Burrows, 1968). This is not to say that electrons in the 1 - 10 kev range cannot be stably trapped above this boundary. We can only state that the average location of this boundary coincides approximately with that of the boundary between the hard and soft electron regions.

### C.3. Dependence of Northern Hemisphere Particle Fluxes on Magnetic Activity.

It has been established (Maehlum and O'Brien, 1963) that the 40 kev trapping boundary moves to lower latitudes during times of high geomagnetic activity. It should therefore be of some interest to determine if the boundaries which we have described undergo any systematic variation with  $K_p$ , a parameter (having values from 0 to 9 as magnetic activity increases) which is logarithmically related to the level of worldwide geomagnetic activity during a three-hour period.

We will designate the invariant latitude of the boundary between the hard and soft electron fluxes by  $\Lambda_1$  and that between the soft zone and the polar cap by  $\Lambda_2$ . After analyzing many passes, it became apparent that during certain passes, especially on the night side, the position of  $\Lambda_1$  was quite difficult to determine (see Figure 30). This behavior will be discussed at length in a succeeding section. We have, however, ignored such passes in considering the movement of  $\Lambda_1$  with magnetic activity. In Figure 32 we have plotted  $\Lambda_1$  versus magnetic local time for various ranges of  $K_p$  for cases where the boundary between the two

zones is easily recognizable. It is evident in that figure that this boundary tends to lie at somewhat lower invariant latitudes during magnetically disturbed periods.

During most passes the boundary designated by  $\Lambda_2$  is fairly abrupt and easily recognizable. However, while this boundary definitely lies at higher latitudes on the day side than on the night side, it is evident from Figure 33 that it undergoes no apparent systematic variation with  $K_p$ . It has been shown by Maehlum, 1968, that  $\Lambda_2$  is well correlated with universal time, attaining its highest values in the northern hemisphere when the earth's dipole axis is tilted toward the sun and its lowest values when the dipole axis is tilted away from the sun (see Figure 34, taken from Maehlum, 1968).

#### C.4. Spectral Characteristics of Precipitated Electrons in the Polar Regions.

Whereas, the three-point electron spectra presented in the preceding section are indicative of the typical characteristics of the fluxes found in the polar regions, examination of the spectral details reveals a somewhat more complicated behavior.

In Figure 35 we have plotted the response in four of the energy bands sampled by channels 4 and 5 during a daytime northern hemisphere pass when  $K_p$  and  $K_c$  (the local College, Alaska K index, which we will use as a measure of high latitude magnetic activity) both had a value of 1. Also given are six-point spectra taken at



two positions along the satellite trajectory. In this and the other similar plots which will be presented in this section, the data points refer to .1-second average fluxes obtained every 5 seconds, while the base lines are threshold fluxes, corresponding to count rates of 10 counts/sec. The six-point differential spectra are actually zero-order approximations, since we have plotted the passbands defined by 10% response to a "flat" laboratory spectrum (see Section II.D.3.). In actuality, the passbands are dependent on the input spectrum, for example, shifting to lower energies for a steep spectrum which decreases toward higher energies. However, due to the discontinuous nature of the spectra encountered in the hard electron region and the "monoenergetic beams" which may be present, little is gained by higher order approximations. We note that the satellite was oriented within  $\sim 20^\circ$  of the local geomagnetic vector during this period (see Section II.C.) so that only those electrons with pitch angles between  $0^\circ$  and  $30^\circ$  are sampled. Since particles with pitch angles less than  $\sim 30^\circ$  at the satellite altitude will mirror below 100 km, and hence be lost to the atmosphere, we conclude that these measurements are of precipitated electrons.

Observations of precipitated electrons during two night side passes are presented in figures 36 and 37. These passes occurred during moderately disturbed geomagnetic conditions ( $K_p, K_c = 2 - 3$ ). The sharp high-latitude cutoff is evident in both passes, being at a somewhat higher latitude in the pass of Figure 36, which corresponds to a time when the earth's dipole was tilted toward the sun, than in that of Figure 37, which occurred near the opposite

configuration. The rapidly varying fluxes in the two lowest energy bands above the apparent high latitude cutoff in Figure 37 are not typical, but are further evidence that the simple picture described in the preceding section does not occur in every pass.

As demonstrated in Figures 35, 36, and 37, the electron spectra characteristic of these regions are somewhat more complex than indicated by the three-channel responses presented in the preceding section. In each of these cases, the spectra in the regions L~5-8 during local night and L~8-20 during local day are relatively flat or slightly peaked at energies of several kev. They are also characterized by a rising intensity below a few hundred ev and a sharp decrease in intensity above ~10 kev. These spectra are similar to those which have been observed from sounding rockets directly above visual auroras (see Section I.D.). Such spectra are typically observed by the Aurora 1 SPECS near the low latitude boundary of precipitated electrons during moderately disturbed periods. The velocity of the satellite projected to 100 km altitude is about 4 km/sec, so the spatial resolution obtainable even when the satellite is not moving perpendicular to the auroral oval is not sufficient to resolve individual arcs. However, the presence of these "auroral" type spectra during periods of high latitude magnetic activity, especially in view of the much softer spectrums observed to the north and the very weak fluxes observed to the south, is suggestive of a direct connection between these electrons and auroral

phenomena. To support the contention that these electron spectra are directly associated with auroral activity, the data in Figure 38, for a pass which occurred when  $K_p = 0+ - 1$  and  $K_c = 0$ , are presented. We note that for this pass the high-latitude cutoff is still apparent as is a quite intense soft zone. However, electron fluxes are largely below threshold for the region where the "auroral" spectra occurred in the disturbed passes, with very weak fluxes noted at lower L values.

#### C.5. Spectral Characteristics of Precipitated Protons in the Night-Side Polar Regions.

In figures 39 and 40 are plotted the response to protons in four energy bands during revolutions 156 and 147, corresponding to the electron data of figures 37 and 38. The SPECS proton geometric factors are not known as accurately as those for electrons due to the indirect means which were necessary in deriving them (see Section II.D.). This fact, coupled with lower counting rates, and hence poorer statistical accuracy obtained in the proton measurements, should be borne in mind when assessing the proton spectra presented in this section. Therefore, we shall be concerned chiefly with the general aspects of the proton spectra and their relative spatial and temporal variations.

In comparing figures 37 and 39 it is evident that the precipitating protons for this moderately disturbed period exhibit a spectral duality similar to that displayed by the electrons. Within the region where the peaked auroral type electron spectrum is observed, the protons possess a

very hard energy spectrum which shows some tendency to peak in the 10 - 15 kev range, in contrast to the electron spectrum which falls off rapidly for energies in excess of 10 kev. Points D and E, for which six-point proton energy spectrums are given in Figure 39, correspond to the similarly designated points in Figure 37. As the satellite moves poleward, there is a rapid transition to much softer spectra in both electrons and protons. Note that the lowest energy proton channel responds appreciably above threshold only in the electron soft zone, while no protons above 10 kev are detected in this region. It is also significant that responses in all proton energy bands are at or below threshold poleward of the sharp electron cutoff (at  $L \sim 8$ ) despite intense low energy electron fluxes which occur sporadically up to  $L \sim 17$ .

In Figure 40 proton data is presented for revolution 147, when  $K_p = 0+ - 1$  and  $K_c = 0$ . In contrast to the electron pattern shown in Figure 38, the protons behave much as they did for the moderately disturbed case considered above. That is, both a hard and a soft proton zone are in evidence, but with somewhat softer proton spectra than in the more disturbed case of Figure 39. Note that in this pass the hard proton zone straddles the low-latitude boundary of the soft electron zone, extending about 3 sample periods ( $\sim 100$  km or 100 cyclotron radii for a 10 kev proton at the satellite altitude) to either side of that boundary. Therefore, appreciable proton fluxes are present in the region where electron response was below threshold (10 counts/sec). In this quiet case,

no significant fluxes of electrons or protons are recorded above the sharp boundary at  $L \sim 11$ .

C.6. Poleward Movement of Auroral Electron and Proton Precipitation During an Auroral Zone Bay Disturbance.

From the data thus far presented, one might conclude that the general particle precipitation pattern is as follows:

(1) During periods of quiet to moderate planetary and high-latitude magnetic activity ( $0 < K_p, K_c \leq 4$ ) there exists, within a few hours of local magnetic noon and midnight, two zones of electron precipitation. The lower latitude zone is characterized by "auroral" type electron spectra similar to those measured by sounding rocket experiments above visual auroras (see Section I.D.). However, for very quiet periods (at least on the night side) electron fluxes in this region are very weak, indicating a strong dependence of intensity on  $K_p$  and  $K_c$ . The other zone, contiguous to and poleward of the hard electron zone, exhibits very soft electron spectra with rapid spatial and/or temporal variations. In addition, narrow "spikes" with somewhat harder spectra, occur sporadically in this region and are probably the "spikes" observed at energies above 40 kev by McDiarmid and Burrows, 1965, and others (see Section I.D.).

(2) During this same period, on the night side, proton precipitation occurs in two zones which coincide roughly, but not exactly, to the electron zones. The proton spectra in the lower latitude zone peak in the energy range 1 - 10 kev and are somewhat harder above 10 kev than are the

electron spectra. The peak shows some tendency to occur at lower energies during the more quiet periods. During very quiet periods, for latitudes below the soft electron region, the ratio of proton flux to electron flux is much higher than during the more disturbed periods, and could be greater than unity.

This general pattern does seem to hold for the majority of cases investigated. However, an important exception has been noted during periods of moderate auroral zone bay activity. In this section, we will consider such a case and its probable relationship to the expansive phase of the auroral substorm (see Figure 41, and Akasofu, 1964).

The electron and proton data presented in figures 42 and 43 are for revolution 157, which occurred subsequent to and during the same period of auroral zone bay activity as revolution 156 (see figures 37 and 39). A magnetogram from College, Alaska (about  $75^{\circ}$  of longitude to the east of the subsatellite point) is shown for this period in Figure 44. The electron fluxes in only three energy bands are presented to simplify the plot. Note in Figure 42 that, whereas a peaked "auroral" type electron spectrum is evident for  $L \sim 5 - 6$ , a similar, but much more intense spectrum is observed sporadically all the way to the sharp cutoff at  $L \sim 9$ . We note in Figure 42 that, while in the lower latitude region the peaked spectrum persists in space and time, the rapid spatial and/or temporal variations which are usual characteristics of the "soft zone" are also noted in the higher latitude peaked spectrum. As shown by the spectra presented in Figure 42, the rapid intensity

variations are accompanied by gross spectral changes, such that the peaked electron spectrum (see point I) is frequently replaced by the much softer spectrum indicated at point H. Again, no electron fluxes are detected poleward of the sharp boundary,  $\Lambda_2$ .

Reference to Figure 43 reveals that the lower latitude portion of the hard electron region is not accompanied by any detectable proton fluxes during this pass. However, relatively hard proton precipitation does begin abruptly at a latitude somewhat ( $\sim 200$  km) below that at which the onset of rapid variations in the 1075 ev - 1910 ev electron channel occurs. Moreover, a change in the character of the proton precipitation toward greater anisotropy is observed about 100 km poleward of the latter point. Therefore, we note that the relatively stable hard proton region is found to straddle the low latitude boundary of the soft electron zone and that the proton energy spectra in the usual soft proton zone are also much harder for this pass.

It is evident then, that at least for the night side, the region described as a "soft zone" for average conditions has the potentiality to take on quite different characteristics during an auroral zone bay event and, as we will discuss in the following section, probably defines the post-breakup "auroral zone".

### C.7. Discussion of Possible Errors Due to Channel Multiplier Efficiency Measurements.

Before proceeding to the next section, we should make the following clarification. The electron fluxes presented in this section are based on the channel multiplier electron efficiency measurements of Frank, 1965. In Section II.D. we noted that Frank's measurements differ considerably from those of Arnoldy (Hoffman and Evans, 1967) in the limited energy range of Arnoldy's observations (~100 ev to 2 kev). Therefore, in Figure 45 we have plotted several of the typical spectra presented in this section using both efficiency curves (noting that Arnoldy's measurements apply to only four of the six energy passbands). The solid lines are obtained with Frank's efficiency curve, while the dotted lines are based on Arnoldy's measurements. For a smoothly decreasing spectrum, the only effect is that Arnoldy's efficiencies result in a somewhat steeper slope, while for the "auroral" type spectra, the effect is to flatten out the relative peak in the 1 - 10 kev region. However, the qualitative features of the spectral shapes as pertain to this discussion are seen to be independent of the efficiency curve used. The proton efficiencies are based on the only known ion measurements, those by Frank, 1965.

In the following sections the observations presented herein will be examined in the light of other experimental results and an assessment will be made of current theoretical explanations.



#### IV. DISCUSSION

The statistical auroral oval (see, e. g., Feldstein, 1966) is the dominant characteristic of the morphology of auroral phenomena at low altitudes. It can be said that if the particles which produce most of these phenomena and the static and oscillatory electric and magnetic fields which cause them to precipitate along the auroral oval are excluded from consideration, then the spatial characteristics of auroral morphology, if not understood, are known to some degree of statistical accuracy. However, as noted in Section I, the auroral particle and field domains have not to date become well-defined. The uncertainties are a result of the difficulty in obtaining an exact theoretical solution of the solar wind - magnetosphere interaction on the one hand and a great lack of experimental particle and field data on the other.

The auroral particle and field problem will not, then, be solved by this or any other single experiment. The present experiment does, however, illuminate some of the more interesting facets of polar charged particle phenomena. This section is meant to place our newly obtained information in its proper perspective and to serve as a vehicle for conjecture on the auroral problem as a whole.

##### A. Relationship of Aurora 1 Data to Previous High-Latitude Charged Particle Measurements at Low Altitudes.

In this section, we will review the results of this experiment in the light of what is presently known about

high-latitude charged particles at low altitudes. In particular, we will discuss the areas in which Aurora 1 data agree with, disagree with, and add to the present body of knowledge as summarized in Section I.D.

Considering first the electron measurements, in Section III.C.1., we noted that on typical passes through the high-latitude regions electron precipitation occurs in three reasonably well-defined regions of latitude, which we referred to as the "auroral zone," the "soft zone," and the "polar cap." Due to the very low count rates observed over the polar cap, we did not obtain statistically significant measurements in that region and therefore could not elaborate further on its properties. However, we were able to establish several characteristics of the other two zones. That is, during moderately disturbed periods ( $K_p \sim 3$ ) on both the day and night sides the "auroral zone" is characterized by appreciable electron fluxes in the range 1 - 10 keV and these fluxes are detected nearly isotropically over the upper hemisphere, but with the upflux amounting to only about 10% of the downflux (see Figure 28). These observations are consistent with satellite and sounding rocket measurements at much lower altitudes (see Section I.D.). In addition, the fact that, at the Aurora 1 altitude (4000 km) electrons in this energy range are detected and that the greater number of them are moving downward, indicates that the 1 - 10 keV electrons are probably energized at altitudes above 4000 km.

We have shown further that the high-latitude limit of these "auroral" type fluxes undergoes a diurnal variation,

for magnetic local times within two hours of noon and midnight, which approximates that of the average boundary above which electron fluxes at pitch angles close to  $90^\circ$  and energies above 35 kev decreased to cosmic ray background as measured by the Alouette 2 satellite (McDiarmid and Burrows, 1968). As shown in Figure 31, this boundary also agrees with the high-latitude edge of the statistical visual auroral zone (Feldstein, 1966). This result is consistent with the Injun 3 observations that the region of maximum auroral light output is closely related to (and perhaps controlled by) the 40 kev trapping boundary. In addition, the regions over which these fluxes are detected are centered near  $68^\circ$  invariant latitude during local night and near  $70^\circ$  invariant latitude during local day, in agreement with the hard electron zones found by the Lockheed group (see Figure 3).

The soft zone, which is characterized by a much softer electron flux and rapid variations along the satellite trajectory is shown in Figure 31 to lie poleward of Feldstein's visual auroral zone and well above the Alouette trapping boundary. The location of the day-side soft zone agrees well with the soft electron region reported by Johnson et al., 1967, that is,  $\sim 74^\circ$ - $80^\circ$  invariant latitude. However, they did not detect such a region on the night side and inspection of Figure 3 shows that their zone of night-side precipitation was confined to invariant latitudes near and just below  $70^\circ$ . In considering this discrepancy, we note that their criterion for the existence of a "soft zone" was the presence of detectable fluxes in an 80 ev threshold detector in the absence of same in a

21 kev threshold detector and that the colatitudes plotted by them in Figure 3 herein are "centers of gravity" of the total electron energy precipitated across the zone (Sharp and Johnson, 1967). With reference to the first point we note that the night side "soft zone" can contain higher energy electrons during auroral substorms and further that it is possible, even during normal periods, that the average "soft zone" spectra are harder for the night side. If this were the case, their criterion that the 21 kev threshold detector not respond above background may not have been generally satisfied in the night-side zone. Furthermore, since it is clear from the Aurora 1 data that under normal conditions the "center of gravity" of total precipitated electron energy lies nearer the low latitude edge of the complete zone of precipitation (including the soft zone), their night-side distributions shown in Figure 3 could be made qualitatively consistent with our observations. Since the "soft zone" variations are too rapid to allow a measurement of pitch angle distribution during the early tumbling stages of the Aurora 1 orbit, it could be argued that the night-side "soft zone" electrons were mirroring above the 150 - 300 km altitude of the Lockheed satellite. However, the data presented in Section III.C.4. shows appreciable fluxes of precipitated electrons, i. e., electrons which will mirror below 100 km.

In Section III.C.3. we defined two boundaries. The invariant latitude of the boundary separating the regions of hard and soft electron fluxes was denoted by  $\Lambda_1$  and this boundary was shown in Figure 32 to have a tendency to lie

at lower latitudes during periods of greater magnetic activity. In view of the spatial relationship between this boundary and an arbitrarily defined "boundary of trapping" (see Figure 31), and since the harder fluxes are expected to cause more auroral light emissions, this conclusion is consistent with the magnetic activity variations noted in visual observations of the auroral zone and the trapping boundary observations of Maehlum and O'Brien, 1963. The invariant latitude ( $\Lambda_2$ ) of the other boundary, above which fluxes in all energy channels are near or below threshold, shows no systematic variation with magnetic activity but, as noted by Maehlum, 1968, tends toward lower latitudes as the angle between the earth's dipole axis and the earth-sun line increases. This boundary is quite abrupt on most cases, especially in the local night, and, as discussed below, is thought to limit the poleward extent of the auroral substorm expansive phase (see Figure 41, taken from Akasofu, 1964).

The investigation of six of the SPECS energy channels further revealed that the electron energy spectra in the day and night side "auroral zones" are relatively flat or in some cases peaked in the energy range 1 - 10 kev. In addition, they exhibit a rising intensity below a few hundred ev and a very sharp intensity decrease for energies above 10 kev. As mentioned above, the shape of the spectra in the range 1 - 10 kev is somewhat in doubt due to the conflicting measurements in that range of channel multiplier counting efficiency. However, the general features of the spectra are independent of these considerations (see Figure 45). Such spectra are consistent with the sounding rocket

differential spectra and the Lockheed "hard zone" integral spectra discussed in Section I.D., although the presence of a "monoenergetic beam" cannot accurately be tested due to the fairly wide passbands of channels 4 and 5. It is especially interesting to note the relatively stable appearance of these fluxes in the latitudinal regions of maximum frequency of auroral occurrence, i. e.,  $L \sim 5 - 8$  near midnight and  $L \sim 8 - 20$  near noon, and that they are generally present for  $K_p \geq 1$ . It is also significant that during very quiet periods ( $K_p \sim 0$ ), at least on the night side, these fluxes are not detectable by the Aurora 1 SPECS, whereas a fairly intense "soft zone" remains. This behavior is consistent with, but more definitive than the Lockheed result that the total precipitated electron energy is strongly correlated with magnetic activity (see Section I.D.).

In Figure 46 we have plotted a typical day-side "soft zone" spectrum along with a differential spectrum measured during the Lockheed 1965 flight. It is apparent in both spectra that most of the energy is contained in electrons with energies less than a few kev.

In Section III.C.5. we have shown that during an auroral zone bay disturbance electron fluxes with spectra similar to, but intensities much higher than those detected in the "auroral zone" are detected in localized regions throughout the night-side "soft zone." In adjacent portions of this zone, electron fluxes are intense but have a spectral shape much like that found in the normal night-side "soft zone." Therefore, we have concluded that the

night-side "soft zone" is also the "post-breakup auroral zone." It is further suggested by the Aurora 1 data that the existing high-latitude boundary of the night-side "soft zone" will limit the poleward extent of auroral motions during the expansive phase of the substorm (see Figure 41). Since this high-latitude boundary ( $\Lambda_2$ ) shows marked dependence on the tilt of the earth's dipole axis, and since auroral substorms usually occur near local midnight, there should be a longitudinal, as well as a seasonal dependence of the poleward extent of the substorm. To our knowledge, no such tendency has been investigated to date. The post-breakup electron spectra mentioned above are in agreement with the rocket observations of Westerlund, 1968, who, using a SPECS detector, found a double-peaked spectrum above auroral arcs and a continuum spectrum between the arcs (see Section I.D.). Also, in Figure 47 we have plotted a spectrum measured by Evans, 1967a, in a post-breakup aurora and a typical Aurora 1 electron spectrum observed in the "post-breakup auroral zone" during revolution 157, and note that they are similar. Finally, the presence of electrons of "auroral" energies at higher latitudes during a polar substorm is consistent with the observations of Lin et al., 1968, that electrons of energies greater than 40 kev are present during such disturbances at much higher latitudes than usual, that is, generally filling the region in which high-latitude "spikes" are observed during normal passes. In the single example presented by Lin et al., 1968, the intensity of electrons ( $\geq 40$  kev) was fairly uniform across this zone. However, the large variations noted in Figure 42 occurred mainly for energies  $< 10$  kev, with

the portion above 40 kev remaining constant within an order of magnitude.

With reference to the proton measurements which have been presented in figures 39, 40, and 43 for three passes through the polar regions, the following comparisons with previous experiments can be made: First, for each of these cases, the proton precipitation is found to occur in the range  $L \approx 5 - 10$ , with essentially no response above threshold outside this region. This is in agreement with the measurements of the Lockheed group on the night side (see Figure 3). However, we have shown in addition that the proton precipitation occurs in two zones with the lower latitude zone exhibiting somewhat harder spectra during normal periods (see figures 39 and 40). The fact that only one night-side proton zone was observed by the Lockheed group can probably be explained as follows. Their 1963 measurements (see Section I.D.) were made with a single 4 kev threshold detector, so that no spectral information was obtained, while in the 1965 flight proton measurements were obtained only for energies above 10 kev. Reference to our Figure 39 indicates that at point E, the two highest energy bands are below threshold (as they are for nearly the entire proton soft region). If we extrapolate the spectrum at point E in the manner shown, the spectrum in the range 10 - 100 kev can be approximated by  $J = (8 \times 10^3) E^{-2.2}$  protons  $\text{cm}^{-2} \text{ster}^{-1} \text{ev}^{-1} \text{sec}^{-1}$ , which represents a total energy between 10 and 100 kev of about  $.006 \text{ ergs cm}^{-2} \text{ster}^{-1} \text{sec}^{-1}$ , which is the upper limit set by the Lockheed group for electrons above 10 kev over the polar cap. The soft proton fluxes shown in Figure 40 for a very quiet pass are markedly



softer than those in Figure 39 so, even allowing for considerable experimental error, it is quite possible that the fluxes in this region during the very quiet period of the Lockheed experiment were below the limit of detectability by the 10 kev threshold detector.

We also note in figures 39 and 40 that, while the hard and soft proton regions coincide roughly with the hard and soft electron regions, they do not coincide exactly. For example, in Figure 40, when  $K_p \sim 0$  and the hard electron zone is not detectable, the onset of the hard proton zone occurs about three sample periods (or about 100 km or 100 cyclotron radii for a 10 kev proton at the satellite altitude) before the abrupt electron soft zone boundary and extends about the same distance into that zone.

The fact that both proton zones are detected in the absence of the hard electron zone during this quiet pass is in agreement with the Lockheed observation that protons are generally present even when  $K_p \sim 0$  and that the correlation between magnetic activity and total precipitated energy is very much weaker for protons than for electrons (see Section I.D.). This is also in agreement with the high proton/electron flux ratio found by Whalen et al., 1967, in a quiet  $H_\beta$  aurora.

The proton energy spectra are generally consistent with previous sounding rocket and satellite measurements as discussed in Section I.D. In Figure 46 we reproduce the proton spectrum which is given for point J in Figure 40 together with a two-point differential spectrum which we have obtained from a three-point integral spectrum (exponential,

with e-folding energy of 19 kev) published by Sharp and Johnson, 1967. Both of these spectra were taken during a very quiet period ( $K_p \sim 0$ ) and are found to be in fairly good quantitative agreement. This same spectrum also compares very favorably with Chase and Anderson's (1967) measurements in which they noted a peak between 750 ev and 1500 ev at  $2 \times 10^3 \text{ cm}^{-2} \text{ ster}^{-1} \text{ ev}^{-1} \text{ sec}^{-1}$  in a visible aurora.

In Figure 43 we have shown that the hard proton zone can expand into the soft proton zone during an auroral zone bay disturbance. This behavior has been suggested from ground-based observations (Eather, 1967), but to our knowledge has not previously been directly observed.

#### B. Relationship of the Various Particle Domains to the Magnetosphere and to Auroral Phenomena.

Examination of a statistical plot of auroral intensity as a function of geomagnetic latitude and magnetic local time (see, e. g., Stringer and Belon, 1967) reveals two maxima, one just before midnight and the other in the early morning (0600 - 0900 hr). The early morning sector has been noted by Sandford, 1964, to be characterized by mantle aurora, which are thought to be produced by electrons a few tens of kev in energy, while discrete auroral forms and particles of a few kev energy are more typical of the midnight maximum region. Whereas, along most of the auroral oval the averaged intensity varies rather smoothly in space and local time, the region near magnetic midnight is a confused maze of isolated maxima. However, we should expect that, based on discussions by Akasofu, 1964, if observations

during auroral substorms were omitted, the region around midnight would take on a more well-defined and stable appearance.

In considering the nature of auroral particle energization it is simplest to begin by ignoring times when auroral substorms are in progress and to identify the quiet auroral zone as a single entity with the harder electron spectra in the early morning hours being a characteristic of the acceleration and/or precipitation mechanism(s). In this vein, steady-state models of magnetospheric convection, such as first proposed by Axford and Hines, 1961, have been successful in predicting the approximate electron energies and precipitation patterns, including the morning maximum. Whether the convection is driven by viscous interaction at the magnetosphere boundary (Axford and Hines, 1961) or by merging between the geomagnetic field lines and a southward component of the solar field (Dungey, 1961; Brice, 1967) or by some other mechanism (Fejer, 1964), the models may all be represented to first order by a closed field line magnetospheric model extended in the antisolar direction in some type of teardrop configuration, with two static electric fields. Both of these electric fields are induced by plasma flow with respect to a magnetic field. The first is the radial electric field produced by corotation of the ionosphere (Alfven and Fälthammer, 1963). The other, directed across the magnetosphere from dawn to dusk, is caused by convection of plasma and field lines due to the solar wind - magnetosphere interaction. The resulting potential drop across the magnetosphere due to this field is estimated by various methods at a few tens of kev during disturbed conditions

(Brice, 1967; Carpenter and Stone, 1967; Vasyliunas, 1967; Taylor and Hones, 1965). If we consider the solar plasma to be injected into the magnetosphere either at some neutral line or by some diffusive mechanism and the resulting magnetospheric plasma to have a significant spread in energy, the following picture results.

Each particle will experience three drift velocities (see, e. g., Norhtrop, 1966),

$$(1) \quad \bar{v}_E = \frac{c\bar{E} \times \bar{B}}{B^2} \quad (\text{Electric field drift}) \quad (36)$$

$$(2) \quad \bar{v}_g = \frac{cW_{\perp}\bar{B} \times \nabla\bar{B}}{eB^3} \quad (\text{Gradient drift}) \quad (37)$$

$$(3) \quad \bar{v}_c = \frac{2cW_{\parallel}\bar{B} \times \bar{R}}{eR^2B^2} \quad (\text{Curvature drift}) \quad (38)$$

where,  $W_{\perp}$  and  $W_{\parallel}$  are the kinetic energies perpendicular and parallel to the magnetic vector  $\bar{B}$  respectively and  $\bar{R}$  the radius of curvature of the field line. For particles with sufficiently low energy, we will have  $v_E \gg v_g, v_c$  and the particles will follow the equipotential lines, the flow pattern being identical for electrons and protons. However, for higher energies, such that the gradient and curvature drifts dominate, the particles will drift across equipotential lines (electrons drifting eastward, protons drifting westward) thereby becoming energized. A given particle, which initially follows equipotential lines, may at some radial distance experience a dominating magnetic drift and begin to drift parallel to the electric field. This will occur at larger radial distances (weaker  $\bar{B}$  values) for the higher energy particles and at smaller distances, or not at all,

as particle energy decreases. Such theories (see Nishida, 1966) also predict a region near the earth, within which the closed equipotentials of the corotation field dominate, to which the convecting solar plasma cannot penetrate, and the boundary of this region conforms well to the observed plasmopause (Carpenter, 1963). Typical flow patterns are given by Brice, 1967. The dawn-dusk direction of the electric field is in accord with an electron energy maximum in the morning hours, although electron energies of tens of kev will require stable trapping for two or three drift revolutions (Brice, 1967).

We can not, however, expect such theories to account for all the details of auroral particle precipitation as observed in this experiment until second-order effects have been included. For example, relative motions of electrons and protons in the simple electric fields described above will give rise to charge-separation electric fields which will act to modify the particle flow. Also, the possibility of acceleration of ionospheric ions and electrons must be considered.

An attempt at accounting for many of these second-order effects was made by Taylor and Hones, 1965. Their work was based on two main assumptions: (1) That, in view of the rarity of particle collisions in the magnetosphere, the geomagnetic field lines may be considered as equipotentials, and (2) That high-latitude magnetic bays are caused by a Hall plus direct current system which flows completely within the ionosphere. They employed an image dipole plus a tail current sheet to simulate the magnetospheric distortion

and assumed that the ionospheric electric fields which drive the polar current systems are mapped throughout the magnetosphere by the "equipotential" magnetic field lines. They then examined the patterns of particles mirroring at low altitudes that resulted from the gradient and curvature magnetic drifts of electrons and protons in the presence of these electric fields.

The problems with this model are many. For example, the assumption of infinite conductivity along magnetic field lines has been questioned by Swift, 1965, who suggested dissipation by interactions of particles and waves. Regarding the second assumption, Bostrom, 1967, noted that while Taylor and Hones derived their electric fields only from those currents which produce disturbances observable on the ground, there may be other systems, such as field-aligned currents, which may not produce such a detectable disturbance. Indeed, the identification of that part of the disturbance which is observed on the ground as due to an ionospheric Hall current is currently very much in doubt. Moreover, even if the Taylor and Hones model can still be viewed as approximately correct, their result that the regions of electron and proton precipitation are separated with the entire proton zone lying equatorward of the electron zone is not compatible with the Aurora 1 observations outlined in the preceding section.

Nevertheless, in view of the stable appearance of auroral particle fluxes in the region  $L \sim 5-8$  (near midnight) and  $L \sim 8-20$  (near noon), it is our belief that the general class of steady-state electrostatic field models discussed above

best explains the existence of quiet auroral forms.

There are, in addition, several features of the Aurora 1 data which must be explained by these theories. First, in accordance with visual observations, the region of stable auroral fluxes moves to lower latitudes with increasing  $K_p$  (see Figure 32) and this is accounted for in the convective models but has been predicted as well by many other models (see, e. g., Dessler and Juday, 1965). Next, even though very weak precipitation of electrons ( $\geq 40$  kev) has been observed by O'Brien, 1964, for  $K_p \sim 0$ , it is clear from the Aurora 1 data that while "auroral" electron fluxes (1 - 10 kev) are quite intense for  $K_p \sim 1$ , they are essentially absent for  $K_p \sim 0$ . This has not been predicted explicitly, since the solar wind, while more uniform and not as intense during these periods, does not stop blowing. There are two possible explanations: (1) The convection may be damped out by dissipation in the ionosphere. It has been estimated (Walbridge, 1967) that the convective driving force must be able to overcome  $\sim 2 \times 10^{18}$  ergs/sec of ionospheric joule plus viscous dissipation. Walbridge and others have estimated that the solar wind can bring a maximum of  $\sim 10^{20}$  ergs/sec to the frontal area of the magnetosphere. The efficiency of the coupling mechanism is not known, but it is possible that, for a weak and steady solar wind flow, the total energy as well as the coupling efficiency of the solar wind could decrease below the level necessary to drive convection. (2) Alternatively, the convection could still proceed but without particle precipitation (note that during these times the SPECS instrument was sampling only those particles with pitch angles less than about  $15^\circ$ ). One of

the difficulties involved with this type of model is the production of a pitch angle distribution that is observed to be isotropic over the upper hemisphere (see Figure 28). According to such models, particle mirror points are lowered by the perpendicular electric fields with a simultaneous increase in  $W_{\perp}$ , with  $W_{\parallel}$  increasing to conserve the second, or longitudinal, invariant. It has not been shown whether the simple model can produce an isotropic pitch angle distribution, but if we must invoke some type of pitch angle scattering, for example by right-circularly polarized waves (Brice, 1964; Kennel and Petschek, 1966), then precipitation may not occur in a very quiet magnetosphere for which particle fluxes may be too low for appreciable wave growth to occur. Also, the presence of protons during these quiet periods could necessitate separate criteria for their acceleration or precipitation. Finally, the shape of the "auroral" electron spectrum has not been predicted by any model to date. This type of spectrum has been observed in visual auroras around midnight and during X-ray events near noon (see Section I.D.), but is shown by the present data to persist generally at 4000 km for  $K_p > 0$ . If the double-peaked spectrum is interpreted as resulting from the superposition of two discrete particle populations with the more energetic portion explained by one of the electric field models, then the data for  $K_p \sim 0$  indicates that during these times the low energy component must disappear as well.

It has been observed that the magnetic field configuration is not satisfactory for particle drifting beyond  $\sim 11 R_E$  (Ness, 1965; Heppner et al., 1967) but instead is



characterized by field lines directed in the solar direction above the equatorial plane and in the antisolar direction below it. These two regions of oppositely directed field are separated by a  $\sim 600$  km thick region of field reversal. This configuration is attributed to a sheet current flowing from dawn to dusk across the magnetosphere. Plasma has been detected (as discussed in Section I) extending to about  $6 R_E$  above and below the neutral sheet, with much higher density and average energy in the field reversal region (Bame et al., 1967). The flow velocity across the tail, being lower than the observed thermal velocities, has not been detected as yet. This configuration limits the radial distance, hence the latitude, within which models such as those described above can operate. Configurations of individual field lines have not been determined sufficiently to locate the position of the limiting latitude with respect to the auroral zone. We will, in the following paragraphs, argue that the day-side "soft zone" and the night-side "soft zone" or "post-breakup auroral zone" as defined in Section III lie outside this limit.

It is evident from the Aurora 1 data that, whereas the region of soft electron fluxes on the night side can contain auroral-type electron spectra during a polar substorm, the day-side "soft zone" has no such characteristic. Thus, even though these two zones show similar electron spectra and both exhibit strong anisotropies, they are not connected via auroral charged particle trajectories to the same region of the magnetosphere. The plasma sheet in the tail has been shown to bear some relation to polar substorms (Vasyliunas, 1967; Freeman and Maguire, 1967). Therefore, we eliminate

the regions of the tail near the ecliptic as sources of the day-side soft electron region. Vasyliunas, 1967, has suggested that an extension of the plasma sheet may exist just inside the subsolar magnetopause. We would expect such a region to map into high day-side latitudes, but reject such a possibility for the soft electron zone, since the particles in this region should be energized to some extent by the magnetospheric electric fields as described above. If such a plasma sheet extension does exist, it is probably related to the day-side region of "auroral type" electrons. Finally, the day-side "soft zone" could be determined by the field lines which map onto the surface of the magnetosphere, implying injection either at the neutral point (see Figure 1) or by some degree of merging between the geomagnetic field and a southward component of the magnetosheath field. Brice, 1967, has considered such merging and estimates that for a 1y merged field which is swept back to  $100 R_E$  downstream of the earth, a region  $3^\circ$  in latitude on the day side would be directly accessible to thermalized solar wind. Such a picture is consistent with the Aurora 1 data in that we should expect a very soft electron spectrum (see Bame et al., 1967), rapid variations, and no auroral substorm effects. Nevertheless, this zone has been detected on every one of about 30 passes, while the merging model requires a southward component of the magnetosheath magnetic field, which the present data (Fairfield and Cahill, 1966) indicate may not always occur. Also, particle detectors at large radial distances on OGO 3 (Vasyliunas, 1967) and Vela 2 and 3 (Bame et al., 1967) have not detected appreciable particle fluxes near the magnetopause except close to the ecliptic plane. Therefore, if such merging is responsible

for the observed day-side fluxes, it probably occurs much closer to the earth than the  $17.5 R_E$  orbit of the Vela satellites.

The polar cap, in which very weak electron fluxes are found, is probably connected to the region of the tail beyond about  $6 R_E$  above or below the ecliptic plane. This conclusion is based on the assumption that day side field lines emanating from just below the polar cap form the magnetosphere boundary and on the fact that no electron fluxes have been detected in the above-mentioned tail regions (Bame et al., 1967; Vasyliunas, 1967). Therefore, if the polar cap field lines cross the ecliptic plane, they do so beyond the radial distance to which the plasma sheet extends. If this is so, the very sharp soft zone - polar cap transition which is especially predominant on the night side would seem to preclude a gradual decrease in plasma sheet densities, requiring instead a steep gradient which may exist but to date has not been predicted or observed. A more tenable picture would involve a gradual plasma sheet radial density gradient with a sharp decrease occurring about  $6 R_E$  above and below the neutral sheet. Such a steep gradient has some basis in previous satellite data (Bame et al., 1967; Vasyliunas, 1967).

The night-side "soft zone" or "post-breakup auroral zone" has been described in Section III and shown to possess extremely variable characteristics during auroral substorms. In the absence of a substorm, fairly soft electron spectra and rapid variations are observed in this region. During a substorm, however, an auroral-type double-peaked spectrum is observed along with the typically soft spectrum mentioned

above, and these are encountered alternately as the satellite traverses the zone. We interpret these rapid variations as partly temporal and partly spatial, due to auroral arc multiplicity. Such a poleward motion of auroral forms is consistent with the expansive phase of the auroral substorm as discussed by Akasofu, 1964, (see Figure 41). Observations of high-energy electrons ( $\geq 40$  kev) by Lin et al., 1968, has revealed a similar increase in the latitude at which these electrons are detected. Lin et al., 1968, concluded from intensity considerations that the high-energy electrons originate outside the Van Allen zone. We propose that their observations were of the high-energy tail of the double-peaked spectrum noted herein.

There has been much recent speculation concerning the role of magnetospheric magnetic field merging in the auroral substorm (see, e. g., Axford, 1967; Akasofu, 1967). The very nature of the substorm, that is, a sudden onset followed by rapid growth and a slow recovery, is that which might result from the perturbation of a system in precarious equilibrium. The magnetic merging explanation is tempting when one considers the immense store of magnetic potential energy which resides in the open tail of the magnetosphere. As the earth rotates, magnetic field lines on the dusk side are continually being swept into the tail while on the dawn side reconnection proceeds at the same rate. Thus, at any time an amount of potential energy resides in the tail which has been estimated by Atkinson, 1966, and others, to be quite sufficient to drive the auroral substorm while, of most importance, there exists a state of lower potential energy that is accessible through magnetic merging. We should note

that the observations of Heppner et al., 1967, that magnetic effects in the tail seem to follow the sudden substorm onset, render doubtful the explanation that merging is initiated by an impulse from the solar wind, producing in turn the sudden onset. Rather, at this point we should consider a single mechanism as producing the onset and acting as the triggering mechanism for merging, with the latter explaining the expansive phase of the substorm. The triggering mechanism might occur in the auroral ionosphere, as suggested by Heppner et al., 1967, or in some other region of the magnetosphere, but there are no solid proposals at this time.

Magnetic merging across the neutral sheet in the tail provides a reasonable explanation for the expansive phase, that is, the rapid ( $\sim 30$  km/sec) poleward motion of auroral forms which follows the brightening and subsequent breakup of quiet arcs. Parker, 1957a, has considered magnetic merging across a neutral sheet in terms of diffusion of the magnetic field through the plasma, a process requiring times of the order of  $\tau = c^{-2}(4\pi\sigma_3 l^2)$ , where  $l$  is a length characteristic of the spatial variation of  $\bar{B}$  and  $\sigma_3$  is the Cowling conductivity. Whereas  $l$  is not prohibitive for localized tail structures,  $\sigma_3$  is essentially infinite in the collisionless neutral sheet so that the field should remain frozen in to the plasma and merging should proceed on a very long time scale. There are two possibilities which may tend to decrease the time required for merging. The first of these involves a local extreme reduction in plasma density so that vacuum merging can occur in limited regions. This mechanism should find its greatest applicability in the cusp region near the earth where plasma densities are low

(Dessler, 1968).

The other possibility is a growing instability which can occur when the neutral sheet is perturbed by a low frequency Alfvén wave. We will consider such a situation in the following paragraphs and show that merging can occur impulsively by this mechanism in times of the order of tens of seconds for conditions such as those in the neutral sheet.

C. Neutral Sheet Instability as a Possible Cause of the Expansive Phase of the Auroral Substorm.

It has been noted (Coppi et al., 1966; Hoh, 1965) that a configuration such as that present in the neutral sheet is closely akin to that of a sheet pinch containing a neutral plane, and hence can be unstable to certain types of perturbations. Hoh, 1965, has shown that particle acceleration will occur in such a situation, while Coppi et al., 1966, have proposed the neutral sheet instability as responsible for the auroral substorm. In order to demonstrate the pertinence of such a mechanism, the following model is presented and evaluated in the light of the data from this and other experiments.

In formulating this or any model, it is desirable initially to achieve maximum simplicity consistent with the observations. We will, therefore, consider the magnetospheric tail configuration of Figure 1 and confine our attention to regions of the tail near the ecliptic plane. It will be consistent with the observations of Ness, 1965, to consider a neutral sheet of about 600 km thickness extending from

the dawn to the dusk magnetospheric boundaries. Further, we will assume that the geomagnetic field is excluded from this region by the pressure of the attendant plasma. That is to say, the only magnetic field in this region is that produced by the neutral sheet current while beyond some 600 km above or below the ecliptic the dominant field is the geomagnetic dipole as perturbed by the neutral sheet current and other currents flowing on the surface of the magnetosphere. In the region external to the neutral sheet, the magnetic field has the approximately constant value of  $15\gamma - 30\gamma$ , with that inside the neutral sheet decreasing in some manner to zero at the ecliptic plane. Considering the coordinate system shown in Figure 1, we will make the further simplifying assumption that the neutral sheet is of infinite extent in the x and y directions and that all equilibrium parameters vary only with x.

We therefore will present a self-consistent description of a two-component plasma sheet with the following characteristics:

- (1) No external electric or magnetic fields,
- (2) Charge neutrality,
- (3) Maxwell-Boltzmann velocity distribution for both ions and electrons,
- (4) Flow velocity along the z-axis which is consistent with the observed tail fields.

The equilibrium distribution for each particle species is given in terms of the plasma density, particle mass and charge, thermal velocities, flow velocity and the electric and magnetic fields produced by the plasma. That is,

$$f_{oj} = N n_j(x) \left( \frac{m_j}{2\pi k T_j} \right)^{3/2} \exp \left( \frac{-\frac{1}{2} m_j v^2}{k T_j} \right), \quad (39)$$

where,

- $m_j$  = particle mass,
- $k$  = Boltzmann constant,
- $T_j$  = kinetic temperature,
- $n_j(x)$  = particle density,
- $N$  = normalization factor,
- $v$  = total velocity.

The density,  $n_j(x)$ , can be written in terms of the electric and magnetic potentials produced by the plasma, using the Boltzmann formula,

$$n_j(x) = n_o \exp \left[ \frac{-q_j \phi_o(x) + q_j V_j A_o(x)}{k T_j} \right], \quad (40)$$

where, the subscript o denotes equilibrium quantities,  $\phi_o$  and  $A_o$  the electric potential and magnetic vector potential respectively,  $q_j$  the particle charge and  $V_j$  the flow velocity. In the above relation, the quantity  $k T_j [q_j \phi_o(x) - q_j V_j A_o(x)]^{-1}$  can be regarded as an electromagnetic scale height for the plasma sheet. From the relation for  $n_j(x)$ , our assumption of charge neutrality is seen to require that  $\phi_o = 0$  and that,

$$-\frac{V_i}{T_i} = \frac{V_e}{T_e}, \quad (41)$$

if we consider singly charged ions such that  $q_i = -q_e$ .

We are now in a position to calculate the equilibrium



magnetic field produced by the plasma sheet. Since  $\Phi_0 = 0$ , we have no electric field and Maxwell's equation may be replaced by Ampere's law,

$$\nabla \times \nabla \times \bar{A}_0 = \frac{4\pi}{c} \bar{J}_0, \quad (42)$$

where,  $\bar{J}_0$  is the equilibrium current and  $c$  the speed of light. This equation may be rewritten in terms of the distribution function as,

$$\nabla(\nabla \cdot \bar{A}_0) - \nabla^2 \bar{A}_0 = \frac{4\pi}{c} \sum_j q_j \int \bar{v}_{cj} f_{oj} d^3 \bar{v}, \quad (43)$$

where  $\bar{v}_{cj}$  is the current-carrying velocity. Choosing the Coulomb gauge ( $\nabla \cdot \bar{A}_0 = 0$ ) and noting that  $\bar{v}_{cj} = v_{zj} \hat{z}$ , with the  $\hat{z}$  denoting a unit vector, we have,

$$\frac{d^2 A_{0z}}{dx^2} = - \frac{4\pi}{c} \sum_j q_j \int v_z f_{oj} d^3 v. \quad (44)$$

After normalizing the distribution function, we can solve the above differential equation for the equilibrium magnetic vector potential,  $\bar{A}_0 = A_{0z} \hat{z}$ .

To normalize  $f_{oj}$  we require that the total number of particles of type  $j$  in a unit volume at the origin be given by the integral of  $f_{oj}(x=0)$  and be equal to  $n_0$ . That is,

$$N = \left[ \left( \frac{m_j}{2\pi k T_j} \right)^{3/2} \int \exp \left( - \frac{m_j v^2}{2k T_j} \right) d^3 v \right]^{-1} = \frac{1}{4}, \quad (45)$$

where we have used the fact that  $A_0(x=0) = 0$ . Evaluating

the integral in equation 44, we obtain the differential equation,

$$\frac{d^2 A_{oz}}{dx^2} = \frac{-n_o e \pi}{c} (V_i - V_e) \exp\left(\frac{e V_i A_{oz}}{k T_i}\right), \quad (46)$$

where we have used the relation 41.

As shown in Appendix II.A., this equation has the solution,

$$A_{oz} = \frac{k T_i}{e V_i} \ln \cosh^{-2} \frac{x}{L}, \quad (47)$$

where,

$$L = \left[ \frac{2ckT_i}{n_o e^2 \pi V_i^2 (1 + T_e/T_i)} \right]^{\frac{1}{2}}. \quad (48)$$

The expression for the ion and electron number densities can then be written,

$$n_j(x) = n_o \cosh^{-2} \frac{x}{L}, \quad (49)$$

so that L may be interpreted as a measure of the thickness of the sheet. The equilibrium magnetic field is obtained as follows,

$$\begin{aligned} \bar{B}_o &= \nabla \times \bar{A}_o = - \frac{\partial A_{oz}}{\partial x} \hat{y} \\ &= \left[ \left\{ \frac{2n_o \pi}{c} k(T_i + T_e) \right\}^{\frac{1}{2}} \tanh \frac{x}{L} \right] \hat{y}. \end{aligned} \quad (50)$$

We are interested in the behavior of this equilibrium situation when a perturbation of the form,  $\bar{A}_1 = A_1(x) e^{i(\omega t + \kappa y)} \hat{z}$  is applied. The resulting distribution function will be

denoted by  $f_j (= f_{oj} + f_{lj})$ . Inserting this combination into the collisionless Boltzmann equation, which is then linearized by considering only those terms first order in the perturbation, and noting that  $f_{oj}$  satisfies the collisionless Boltzmann equation for the equilibrium fields, we are left with,

$$\begin{aligned} \frac{\partial f_{lj}}{\partial t} + \bar{v} \cdot \nabla f_{lj} + \frac{q_j}{m_j} (\bar{v} \times \bar{B}_0) \cdot \nabla_v f_{lj} + \\ \frac{q_j}{m_j} (\bar{E}_1 + \bar{v} \times \bar{B}_1) \cdot \nabla_v f_{oj} = 0, \end{aligned} \quad (51)$$

or,

$$\frac{df_{lj}}{dt} = - \frac{q_j}{m_j} (\bar{E}_1 + \bar{v} \times \bar{B}_1) \cdot \nabla_v f_{oj}, \quad (52)$$

where,

$$\begin{aligned} \bar{E}_1 &= - \frac{1}{c} \frac{\partial \bar{A}_1}{\partial t} = - \frac{i\omega}{c} A_1 z, \\ \bar{B}_1 &= \nabla \times \bar{A}_1 = i\kappa A_1 x - \frac{\partial A_1}{\partial x} y, \\ \nabla_v f_{oj} &= \frac{-m_j}{kT_j} (v_x f_{oj} x + v_y f_{oj} y + (v_z - V_j) f_{oj} z). \end{aligned}$$

For this type of perturbation, the total time derivative may be written,

$$\frac{d}{dt} = i\omega + v_x \frac{\partial}{\partial x} + v_y i\kappa,$$

so that  $f_{lj}$  is given by the time integral over the unperturbed orbits,

$$f_{lj} = \int_{-\infty}^t \left( \frac{q_j f_{oj}}{kT_j} \right) \left( v_j \frac{dA_1}{dt} + v_z E_1 \right) dt.$$

Explicit integration over the charged particle trajectories in the field  $\bar{B}_0$  is distracting in its mathematical details (see Hoh, 1966). However, we can recover the approximate form of  $f_{1j}$  by assuming  $v_z$  and  $v_y$  constant and integrating over time, deferring to a later paragraph treatment of the unperturbed particle trajectories, with the result,

$$f_{1j} = \frac{q_j f_{0j}}{kT_j} v_j A_1 - i(\omega + \kappa v_y)^{-1} v_z E_1. \quad (54)$$

We wish to investigate the stability criterion and to this end we consider the Maxwell equation,  $\nabla \times \nabla \times \bar{A}_1 = \frac{4\pi}{c} \bar{J}_1$ , or, in this case, with  $\bar{A}_1 = A_{1z} \hat{z}$ , and setting  $\nabla \cdot \bar{A}_1 = 0$ ,

$$\frac{\partial^2 A_1}{\partial x^2} + \frac{\partial^2 A_1}{\partial y^2} = -\frac{4\pi}{c} \sum_j q_j \int_{-\infty}^{\infty} v_z f_{1j} d^3 v. \quad (55)$$

The integral on the right is evaluated in Appendix II.B., assuming low frequency perturbations, such that  $\omega/\kappa \ll v_{Tj}$ , where  $v_{Tj} = (2kT_j/m_j)^{1/2}$ . As we will discuss later, low frequency waves not only simplify the mathematics but are physically the most interesting. The results of Appendix II.B. allow us to write equation 55 for low frequencies as,

$$-Cn(x) \frac{\partial A_1}{\partial t} + \frac{\partial^2 A_1}{\partial x^2} + \frac{\partial^2 A_1}{\partial y^2} + \frac{2n(x)}{n_0 L^2} A_1 = 0, \quad (56)$$

where,

$$C = \frac{4\pi}{c} \sum_j \frac{q_j^2}{kT_j} \left( \frac{m_j}{2\pi kT_j} \right)^{1/2} \left( \frac{kT_j}{m_j} + v_j^2 \right).$$

Due to the assumed form of  $A_1$ , we expect  $\frac{\partial^2 A_1}{\partial x^2}$  to be much

smaller than the other terms in this equation. Neglecting this term and replacing  $\partial A_1 / \partial t$  and  $\partial^2 A_1 / \partial y^2$  by  $i\omega A_1$  and  $-\kappa^2 A_1$  respectively, we have,

$$- Cn(x) i\omega A_1 + \left( \frac{2n(x)}{n_o L^2} - \kappa^2 \right) A_1 = 0. \quad (57)$$

Therefore,  $i\omega$  is given by,

$$i\omega = \frac{\frac{2n(x)}{n_o} - \kappa^2 L^2}{L^2 C n(x)}. \quad (58)$$

Since  $2L$  is the approximate thickness of the plasma sheet, we consider only those  $x$  such that  $|x| < L$ . In this range, since  $\cosh u = \frac{1}{2}(e^u + e^{-u})$ , the plasma density may be approximated by,

$$.5n_o < n(x) < n_o, \text{ for } 0 < |x| < L. \quad (59)$$

Positive values of  $i\omega$  then require  $\kappa^2 L^2 < \frac{2n(x)}{n_o}$  or,  $\kappa^2 L^2 < 1$ . That is, when  $\kappa^2 L^2 < 1$ ,  $A_1$  grows with time and hence we have instability. Of course, when  $\kappa=0$ , the wave itself, hence the instability, will vanish, so we find an ideal neutral sheet configuration to be unstable for  $\omega/\kappa < v_{Tj}$  and  $\partial^2 A_1 / \partial x^2$  small if the condition  $0 < \kappa^2 L^2 < 1$  is satisfied. This result has been obtained by several authors (Furth, 1962; Pfirsch, 1962; Laval and Pellat, 1964) in varying degrees of approximation.

The growth rate,  $(i\omega)^{-1}$  cannot be calculated exactly from the above relation for  $i\omega$  because of the approximations made. However, in an exact treatment, Laval et al., 1965,

have shown that the growth time is on the order of 10 seconds for an electron temperature of 100 ev and densities of a few per  $\text{cm}^3$ .

To describe a simple physical picture of the instability, we refer to Figure 48, taken from Hoh and Bers, 1966, which indicates the initial distortion of the equilibrium magnetic field due to the perturbation,  $\bar{A}_1 = A_1(x)e^{i(\omega t + \kappa y)\frac{1}{2}}$ . This perturbation may be viewed in terms of the currents which would alter the equilibrium configuration as shown. As noted in Figure 48, the perturbed currents are always antiparallel to the induced electric field  $\bar{E}_1$ , so that the energy of these currents is transferred to  $\bar{E}_1$ , thereby energizing the wave by a form of Landau growth. This results in a growth of the magnetic field distortion until magnetic merging occurs at the nodes, which we have shown above to be separated by a distance on the order of  $L$  (the neutral sheet thickness). The stability criterion derived above can be interpreted to mean that there must be sufficient separation of regions of oppositely directed perturbed currents and electric fields to prevent their mutual interaction, the required distance being on the order of an ion cyclotron radius.

It will be of interest to inquire into the unperturbed particle trajectories to determine which type of particles actually drive the instability. Referring to the work of Parker, 1957b, and considering the region  $|x| < L$ , so that  $\tanh \frac{x}{L} \approx \frac{x}{L}$ , we have for the equations of motion of particles in the equilibrium magnetic field  $\bar{B}_0$ ,

$$\begin{aligned}
 m_j \frac{d^2 x}{dt^2} &= - \frac{q_j}{c} v_z B_{\max} \frac{x}{L}, \\
 m_j \frac{d^2 z}{dt^2} &= \frac{q_j}{c} v_x B_{\max} \frac{x}{L}.
 \end{aligned}
 \tag{60}$$

Integrating the second of these equations once with respect to  $t$ , we have,

$$v_z = \frac{q_j}{m_j c} \frac{x^2}{L} B_{\max} + v_{z0}.
 \tag{61}$$

The possible trajectories are many, but may be separated into those that cross the  $x = 0$  plane and those that do not. Figure 49, taken from Hoh and Bers, 1966, indicates the general features of these two types of orbits. That is, the noncrossing particles drift in the direction opposite to  $v_j$  while the crossing particles trace out a meandering type of orbit along either the  $+z$  or  $-z$  direction. Since the thermal velocity is much greater than the resulting drift velocity, the crossing particles will be most effective in transferring energy to and from the perturbed electromagnetic fields. Also, due to their lower velocity for  $T_i \approx T_e$ , the ions will not be nearly as effective as the electrons. We can estimate the region to which the crossing particles are confined by considering an electron at  $x=0$  with an initial velocity in the  $-z$  direction with magnitude  $v_T$ , i. e., an average particle. At its maximum excursion from the  $x=0$  plane, its velocity will be  $\bar{v} = v_T \hat{z}$  and the corresponding value of  $x$  is given by,

$$x_{\max} = \left( \frac{2v_T}{\omega_{B_{\max}}} L \right)^{\frac{1}{2}}, \quad (62)$$

where,  $\omega_{B_{\max}}$  is the cyclotron frequency at  $B = B_{\max}$  and  $v_T/\omega_{B_{\max}}$  is equivalent to an average electron cyclotron radius  $\rho_e$ , so that,

$$x_{\max} = (2\rho_e L)^{\frac{1}{2}}, \quad (63)$$

or,

$$x_{\max} \approx 35 \text{ km},$$

for  $T_e = 100 \text{ ev}$ ,  $B = 20\gamma$ , and  $L = 300 \text{ km}$ . It has been shown by Parker, 1957b, that in the region  $|x| < (2\rho_e L)^{\frac{1}{2}}$  the particle drift velocities are in the  $-z$  direction for all particles crossing the  $x=0$  plane at angles to the  $-z$  axis of less than about  $130^\circ$  while the others drift in the  $+z$  direction. Therefore, most of the electrons drift along the  $\bar{E}_1$  direction in the region near the crest of the perturbed magnetic field as shown in Figure 48, and these are the electrons which will be giving up energy to the perturbation fields, while a few will drift against  $\bar{E}_1$ , hence becoming energized.

Various types of particle acceleration which can occur near the neutral sheet have been investigated by Speiser, 1965, and Hoh, 1965. For our purposes, however, it is most significant that such an inherent neutral sheet instability could play the dominant role in the expansive phase of the substorm through the merging of magnetic field lines and the resulting transfer of magnetic energy to particle energy.



The results which we have obtained are correct only for low frequency perturbations, such that  $\omega/k \ll v_{Tj}$ , where  $k^2 L^2 < 1$ . With  $L \sim 300$  km and  $T_j \sim 100$  ev - 1,000 ev, periods must be on the order of minutes to tens of minutes or longer. The existence of wave disturbances in the magnetic tail is not as yet on a sound experimental basis. However, the theoretical arguments of Dessler and Walters, 1964, that variations in the orientation of the interplanetary magnetic field should cause a "tail wagging" type of perturbation, and the experimental detection by Anderson, 1965, of an apparent periodicity of  $\sim 5$  minutes in tail electron fluxes ( $\geq 40$  kev) are suggestive that such low frequency perturbations could be of importance. As discussed in Section I.C., some experimental support for magnetic field merging in the tail is found in the observations of Anderson and Ness, 1966, that high-energy "island" electron fluxes are associated with broad regions of magnetic field depression.

The fact that electron precipitation is observed in the night-side soft zone during normal periods (i. e., before the auroral breakup) casts some doubt on the idea proposed by Evans, 1968, that the expansive phase of the auroral substorm results from pitch angle scattering of trapped particles into the loss cone resulting from an enhancement of trapped particle fluxes, as described by Kennel and Petschek, 1966. The continuous precipitation of electrons in the night-side soft zone is more consistent with field lines which extend into the plasma sheet with the expansive phase of the substorm resulting from impulsive injection of energetic particles.

#### D. Summary and Conclusions.

In summary, the Aurora 1 SPECS experiment measured electrons and protons in the energy range  $50 \text{ ev} \leq E \leq 100 \text{ kev}$  (with the proton measurements, especially in the range  $E < 1 \text{ kev}$ , being of much less accuracy than the electron measurements) in the polar regions at magnetic local times within two hours of noon and midnight. During periods of slight to moderate planetary and high-latitude magnetic activity ( $1 \leq K_p, K_c \leq 4$ ), high-latitude electron precipitation was detected in two regions of latitude. In the lower latitude region ( $L \sim 5-8$  near midnight,  $L \sim 8-20$  near noon), "auroral" type electron spectra were observed. These spectra are relatively flat or slightly peaked in the energy range  $1 - 10 \text{ kev}$ . In addition, they exhibit a rising intensity below a few hundred electron volts and a very sharp intensity decrease for energies above  $\sim 10 \text{ kev}$ . Electron pitch angle distributions in this region were observed to be nearly isotropic over the upper hemisphere, with an atmospheric loss of electrons noted for energies  $> 500 \text{ ev}$ .

Adjacent to and poleward of this region a zone of much softer electrons was observed, with spectra tending to peak near  $100 \text{ ev}$  and falling off sharply with increasing energy, so that nearly all the electrons have energies less than a few kev. Large spatial and/or temporal variations, which precluded pitch angle determinations by the spinning satellite, were observed in this region.

The boundary between these two regions was observed to undergo a diurnal variation (for the sampled local times)

which approximates that of the high-latitude boundary of the average visual auroral zone. This boundary was observed to lie at lower latitudes during periods of increased magnetic activity, while the high-latitude boundary of the soft electron zone was observed to lie at higher latitudes for smaller values of the angle between the earth's dipole axis and the earth-sun line (Maehlum, 1968).

The night-side soft electron region was seen to contain localized "auroral" type electron fluxes during an auroral zone bay disturbance. During very quiet periods ( $K_p, K_c \sim 0$ ), electron fluxes in the night-side hard electron region were below the detectable limit of the experiment, while no decrease in intensity was noted in the soft electron region, although the spectra in that region were somewhat softer than during more disturbed periods.

Night-side proton precipitation was also found to occur in two contiguous zones, with harder and softer fluxes noted in the lower and higher latitude zones respectively. These zones did not correspond exactly to the electron zones. Rather, the hard proton zone was observed either to straddle or to lie just below the low-latitude boundary of the soft electron zone. No proton precipitation was observed poleward of the high-latitude cutoff of the soft electron fluxes.

During an auroral zone bay disturbance, the proton fluxes in the soft proton region became somewhat harder. For very quiet periods, the protons, unlike the electrons, were found in both zones with only slightly less intensity, but

somewhat softer spectra than during the more disturbed periods.

Of these observations, those which have a precedent were found to be generally consistent with previous measurements in the same regions. We further concluded that:

(1) Due to the observed reflection coefficient ( $\sim .1$  to  $.01$ ) for electron energies  $\geq 1$  keV in the hard electron zone, most of these electrons must have been accelerated at altitudes above 4000 km. However, we obtained pitch angle distributions only for three-point spectra and hence did not examine pitch angle variations of the various spectral details.

(2) Because of the observed universal time dependence of the position of the high-latitude boundary of the soft electron zone (Maehlum, 1968), and since, during auroral zone bay disturbances, the "auroral" type electron fluxes were observed to extend up to that boundary, we concluded that there should be a longitudinal, as well as a seasonal, dependence of the maximum poleward extent of the expansive phase of the auroral substorm as observed from the ground near midnight.

(3) In view of the similarity of the electron fluxes observed in the hard electron region near noon and midnight, the auroral injection and acceleration mechanism(s) must be operative to much the same degree near noon and midnight, and that the steady-state magnetospheric electric field models satisfy this criterion most easily.

(4) Since particle precipitation is seen to occur in the night-side soft electron zone before auroral breakup, it is difficult to envisage the expansive phase of the auroral

substorm as resulting from pitch angle scattering of trapped electrons into the loss cone. Rather, impulsive injection of energetic particles, such as could occur as a result of magnetic field merging in the tail, is probably necessary. Such a picture could also account for the normal night-side soft electron zone through a mapping of the plasma sheet to low altitudes.

(5) Since electron fluxes in the hard electron region were below detectable limits (at least on the night side) during magnetically very quiet periods, the auroral electron acceleration and/or precipitation mechanism(s) must be either inoperative or weak enough to be effectively damped out (perhaps by ionospheric dissipation) during these times.

(6) The gross similarities between the zones of proton and electron precipitation and their similar behavior during auroral substorms suggest a degree of commonality between the electron and proton injection and acceleration mechanism(s). However, the presence of the hard proton zone (with somewhat softer spectra than during more disturbed times) during very quiet periods indicates that, whereas the proton acceleration mechanism is dependent on the level of magnetic activity, the protons are not affected as much as are the electrons.

We were not able to make a definite decision about the configuration of the polar magnetic field lines, mainly because of lack of sufficient magnetic field and particle measurements throughout the magnetosphere and magnetosheath. However, we did conclude that the Aurora 1 data is most consistent with a hard electron zone, or quiet auroral zone, which occurs on field lines which are sufficiently closed

that the auroral particle behavior (at least for electrons) is much the same near noon as near midnight.

Lack of extensive particle measurements in the magnetosheath, coupled with the fact that the particle spectra should be dependent on the distance downstream of the stagnation point (that is, the maximum temperature and minimum streaming velocity should occur just at the subsolar point with these parameters approaching the unperturbed solar wind values far downstream of the earth), made an assessment of the degree of communication between this region and the low altitude polar regions difficult. However, it is possible that the day-side "soft zone" is connected in some way to the magnetosheath (perhaps through merging of geomagnetic field lines with magnetosheath field lines or through neutral point injection).

Regarding the night-side "soft zone", the presence of "spikes" of energetic electrons and the continued presence of soft particle fluxes even during very quiet periods suggested that this region is connected to the geomagnetic tail. To support this conclusion, in Figure 50 we compare the electron spectrum which we presented for the night-side "soft zone" in Figure 36 with a typical plasma sheet electron spectrum published by Montgomery, 1968. Note that Montgomery's spectrum is plotted for omnidirectional fluxes, so the Aurora 1 directional fluxes (in the absence of a measured pitch angle distribution) should be multiplied by a number of order 5 - 10, resulting in somewhat better agreement. Even with this uncertainty, there is reasonable agreement both qualitatively and quantitatively.

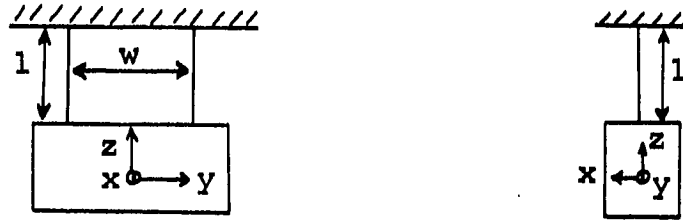
Finally, it is hoped that the results of the Aurora 1 SPECS experiment will serve as sufficient motivation for further low altitude polar charged particle measurements, with greater sensitivity and time resolution and at other local times.

ACKNOWLEDGEMENTS:

I am grateful to Professor Brian J. O'Brien for his continuing guidance and support. Particular thanks are due to Cdr. C. W. Causey of ONR and to the personnel of the Navy Space Systems Activity, Space Systems Division, of the U. S. Naval Space Surveillance Systems, of Goddard Space Flight Center for STADAN support, the NASA Manned Spacecraft Center, and members of the Space Science Facilities at Rice University for their help and support. I wish to further acknowledge Mr. R. L. Trachta, Payload Manager, and Mr. H. Killen, Payload Engineer, and the valuable assistance of Mr. F. H. Abney and Mr. R. A. Harrison in the design of the SPECS instrument. Many helpful discussions with Drs. B. N. Maehlum, L. H. Westerlund, and M. A. Schield, and Mr. R. E. LaQuey are gratefully acknowledged. Special thanks are due my wife, Kathleen, and daughter, Angela, for their technical and moral support. This research was supported in part by the Office of Naval Research under contract Nonr-4964(1).

APPENDIX I: Derivation of Equation for Experimental Determination of Satellite Moments of Inertia.

Consider a solid, rectangular-shaped body of mass  $M$  suspended by two massless wires as shown below,



where,  $w$  is the distance between the wires and  $1$  is the length of the wires. If a slight angular displacement,  $\theta$ , is imparted about the  $z$ -axis, the change in potential energy of the system (neglecting torsion in the wires, and assuming that the displacement of the point at which the wire is attached is perpendicular to the  $y$ -axis) can be written,

$$V = - Mg \cos \left\{ \sin^{-1} \left( \frac{w \sin \theta}{1} \right) \right\} ,$$

where, the angle in braces is the angle between the wires and the vertical. For small angles, such that  $\sin \varphi \approx \varphi$ , we have the Lagrangian,

$$L = \frac{1}{2} I_z \dot{\theta}^2 + Mg \cos \left( \frac{w \theta}{1} \right) ,$$

where,  $I_z$  represents the moment of inertia about the  $z$ -axis and  $g$  the acceleration of gravity. Lagrange's equation gives,

$$I_z \ddot{\theta} + Mg \left( \frac{w}{1} \right) \sin \left( \frac{w}{1} \right) = 0 ,$$



or, with  $\sin \theta \approx \theta$ ,

$$I_z \frac{d^2}{dt^2} \left( \frac{w\theta}{2l} \right) + Mg \left( \frac{w^2}{4l^2} \right) \frac{w\theta}{2l} = 0,$$

which is the equation for simple harmonic motion with period

$$T = 4\pi \left( \frac{I_z l^2}{Mgw^2} \right)^{\frac{1}{2}}.$$

Therefore, the moment of inertia about the z-axis is given by,

$$I_z = \frac{Mgw^2 T^2}{16\pi^2 l^2}.$$

APPENDIX II: Mathematical Details of Section IV.C.

II.A. Solution of the Differential Equation 46.

We rewrite equation 46 as follows,

$$\frac{d^2 A_{oz}}{dx^2} = -b \exp(gA_{oz}),$$

and proceed, multiplying both sides by  $2(dA_{oz}/dx)$ , generating,

$$2 \frac{dA_{oz}}{dx} \frac{d^2 A_{oz}}{dx^2} = -2 \frac{dA_{oz}}{dx} b \exp(gA_{oz}).$$

Integrating with respect to  $x$ , we have,

$$\left[ \frac{dA_{oz}}{dx} \right]^2 = -2 \int b \exp(gA_{oz}) dA_{oz} + C_1,$$

or,

$$dx = \frac{dA_{oz}}{\left\{ -2 \int b \exp(gA_{oz}) dA_{oz} + C_1 \right\}^{1/2}}.$$

Integrating over  $A_{oz}$  yields,

$$dx = \frac{dA_{oz}}{\left\{ -\frac{2b}{d} \exp(gA_{oz}) + C_2 \right\}^{1/2}}.$$

Letting  $u = (2b/g)^{1/2} \exp(gA_{oz}/2)$ , we can rewrite this as,

$$dx = 2 \frac{du}{gu(-u^2 + C_2)^{\frac{1}{2}}},$$

which integrates to,

$$x = \frac{2}{d} \left[ -C_2^{-\frac{1}{2}} \ln \left\{ u^{-1} \left( C_2^{\frac{1}{2}} + \sqrt{-u^2 + C_2} \right) \right\} \right] + C_3.$$

Since,

$$\operatorname{sech}^{-1} \frac{w}{a} = \ln \left\{ w^{-1} \left( a + \sqrt{-w^2 + a^2} \right) \right\},$$

x is given alternatively by,

$$x = \frac{2}{d} \left\{ -C_2^{-\frac{1}{2}} \operatorname{sech}^{-1} \left( \frac{u}{C_2^{\frac{1}{2}}} \right) \right\} + C_3.$$

The boundary condition,  $A_{oz}(x=0) = 0$ , gives the relation,

$$C_3 \frac{gC_2^{\frac{1}{2}}}{2} = \operatorname{sech}^{-1} \left\{ \left( \frac{2b}{gC_2} \right)^{\frac{1}{2}} \right\},$$

which is satisfied if  $C_3 = 0$  and  $C_2 = 2b/g$ . Therefore, the equilibrium magnetic vector potential is given by,

$$\bar{A}_O = A_{OZ} z = g^{-1} \left\{ \ln \cosh^{-2} \left[ \left( \frac{bg}{2} \right)^{\frac{1}{2}} x \right] \right\}^{\frac{1}{2}},$$

or, substituting for b and g and using the relation

$$V_e T_i = -V_i T_e,$$

$$\bar{A}_O = \frac{kT_i}{eV_i} \ln \cosh^{-2} \left[ \left\{ \frac{n_o e^{2\pi V_i^2} (1 + T_i/T_e)}{2ckT_i} \right\}^{\frac{1}{2}} x \right]^{\frac{1}{2}}.$$

## II.B. Evaluation of the Integral in Equation 55.

We are to evaluate the integral,

$$\sum_j q_j \int v_z f_{1j} d^3v ,$$

or,

$$\sum_j \frac{q_j^2}{kT_j} \int v_j A_1 v_z f_{0j} d^3v -$$

$$\sum_j \frac{q_j^2}{kT_j} \int i(\omega + \kappa v_y)^{-1} v_z^2 E_1 f_{0j} d^3v = I_1 + I_2 .$$

Considering first the integral  $I_1$ , integration over velocity space yields,

$$\int v_z f_{0j} d^3v = \frac{n(x)}{4} v_j ,$$

so that for the two-component plasma,

$$I_1 = \frac{e^2}{4k} \left\{ \frac{v_i^2}{T_i} - \frac{v_e^2}{T_e} \right\} n(x) A_1 .$$

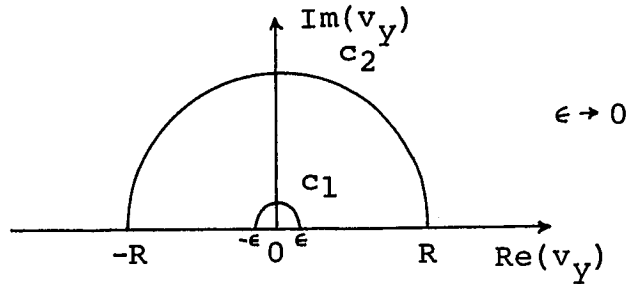
Multiplying the terms in parentheses by  $T_i/T_i$  and noting that  $v_e T_i = -v_i T_e$ , it is seen that, referring to Eq. 48,

$$I_1 = \left( \frac{c}{2\pi n_o} \right) \frac{n(x)}{L^2} A_1 .$$

Evaluation of  $I_2$  for low frequencies, such that  $\omega/\kappa \ll v_{Tj}$ , where  $v_{Tj} = (2kT_j/m_j)^{1/2}$ , proceeds as follows. First note that  $\bar{E}_1 = -c^{-1}(\partial A_1/\partial t)$ , so that,

$$I_2 = \frac{i}{c} \sum_j \frac{q_j^2}{kT_j} (\omega + \kappa v_y)^{-1} v_z^2 \frac{A_1}{t} f_{oj} d^3v.$$

For small  $\omega$ , we make the approximation,  $(\omega + \kappa v_y) = \kappa(\omega/\kappa + v_y) \approx \kappa v_y$ , since  $v_y = v_{Tj}$  for an average particle. While the integrations over  $v_x$  and  $v_z$  are straightforward, the simple pole at  $v_y = 0$  must be taken into account in integrating over  $v_y$ . We consider  $v_y$  as in general a complex variable and integrate over the contour shown below, and let  $R \rightarrow \infty$ .



Since the function  $v_y^{-1} \exp(-m_j v_y^2 / 2kT_j)$  is real and analytic except at  $v_y = 0$ , the only contribution will be from the integration around  $c_1$ . That is,

$$\begin{aligned} \int_{-\infty}^{\infty} v_y^{-1} \exp\left(-\frac{m_j v_y^2}{2kT_j}\right) dv_y &= 2\pi i \operatorname{Res}_{v_y=0} \left\{ v_y^{-1} \exp\left(-\frac{m_j v_y^2}{2kT_j}\right) \right\} \\ &= 2\pi i \lim_{v_y \rightarrow 0} v_y \left\{ v_y^{-1} \exp\left(-\frac{m_j v_y^2}{2kT_j}\right) \right\} \\ &= 2\pi i, \end{aligned}$$

and we have,

$$I_2 = -\frac{\pi}{c} \sum_j \frac{q_j^2}{kT_j} \left(\frac{m_j}{2\pi kT_j}\right)^{1/2} \left(\frac{kT_j}{m_j} + v_j^2\right) n(x) \frac{\partial A_1}{\partial t}.$$

BIBLIOGRAPHY

- Akasofu, S.-I., The development of the auroral substorm, Planet. Space Sci., 12, 273, 1964.
- Akasofu, S.-I., Dynamic morphology of auroras, Space Sci. Rev., 4, 498, 1965.
- Akasofu, S.-I., The auroral oval and the internal structure of the magnetosphere, Aurora and Airglow, ed. by Billy M. McCormac, Reinhold Publishing Corp., New York, 267, 1967.
- Albert, R. D., Energy and flux variations of nearly mono-energetic auroral electrons, J. Geophys. Res., 72, 5811, 1967a.
- Albert, R. D., Low-energy electron and proton spectra in the auroral zone, Trans. Am. Geophys. Union, 48, 180, 1967b.
- Alfven, H. and C.-G. Fälthammer, Cosmical Electrodynamics, 2nd ed., Oxford Univ. Press, London, 1963.
- Anderson, K. A., Balloon observations of x-rays in the auroral zone, J. Geophys. Res., 65, 551, 1960.
- Anderson, K. A., Energetic electron fluxes in the tail of the magnetosphere, J. Geophys. Res., 70, 4741, 1965.
- Anderson, K. A., and N. F. Ness, Correlation of magnetic fields and energetic electrons on the Imp 1 satellite, J. Geophys. Res., 71, 3705, 1966.
- Angel, D. W., H. W. Cooper, W. R. Hunter and R. Tousey, Extreme ultraviolet detection with the Bendix single channel photomultiplier, Paper presented at the Image Intensifier Symposium, Ft. Belvoir, Va., 24-26 Oct., 1961.
- Atkinson, G., A theory of polar substorms, J. Geophys. Res., 71, 5157, 1966.
- Axford, W. I., Magnetic storm effects associated with the tail of the magnetosphere, Space Sci. Rev., 7, 149, 1967.

- Axford, W. I., and C. O. Hines, A unifying theory of high-latitude geophysical phenomena and geomagnetic storms, Canadian J. Phys., 39, 1433, 1961.
- Axford, W. I., H. E. Petschek, and G. L. Siscoe, Tail of the magnetosphere, J. Geophys. Res., 70, 1231, 1965.
- Bame, S. J., J. R. Asbridge, H. E. Felthouser, E. W. Hones, and I. B. Strong, Characteristics of the plasma sheet in the earth's magnetotail, J. Geophys. Res., 72, 113, 1967.
- Baroody, E. M., A theory of secondary emission from metals, Phys. Rev., 78, 780, 1950.
- Beard, D. B., The interaction of the terrestrial magnetic field with the solar corpuscular radiation, J. Geophys. Res., 65, 3559, 1960.
- Beard, D. B., The solar wind geomagnetic field boundary, Rev. of Geophys., 2, 335, 1964.
- Bostrom, R., Auroral electric fields, Aurora and Airglow, ed. by Billy M. McCormac, Reinhold Publ. Corp., New York, 293, 1967.
- Brice N. M., Fundamentals of very low frequency emission generation mechanisms, J. Geophys. Res., 69, 4515, 1964.
- Brice, N. M., Bulk motion of the magnetosphere, J. Geophys. Res., 72, 5193, 1967.
- Bridge, H., A Egidi, A. Lazarus, E. Lyon, and L. Jacobson, Preliminary results of plasma measurements on Imp A, Space Res. V, 1965.
- Bruining, H., Physics and Applications of Secondary Electron Emission, Pergamon Press, London, ch. 4, 1954.
- Burch, J. L., Low-energy electron fluxes at latitudes above the auroral zone, To be published, J. Geophys. Res., 73, June 1, 1968.
- Cahill, L. J. and P. J. Amazeen, The boundary of the geomagnetic field, J. Geophys. Res., 68, 1835, 1963.

- Carpenter, D. L., Whistler evidence of a "knee" in the magnetospheric ionization density profile, J. Geophys. Res., 68, 1675, 1963.
- Carpenter, D. L., and K. Stone, Direct detection by a whistler method of the magnetospheric electric field associated with a polar substorm, Planet. Space Sci., 15, 395, 1967.
- Chamberlain, J. W., Physics of the Aurora and Airglow, Academic Press, New York, ch. 4, 1961.
- Chapman, S., and J. Bartels, Geomagnetism, Oxford Press, London, 1940.
- Chapman, S., and V. C. A. Ferraro, A new theory of magnetic storms, Terr. Mag. Atmos. Elec., 36, 77, 171, 1931.
- Chase, L. M., Spectral measurements of auroral zone particles, Preprint of Space Sciences Lab., Univ. Calif., Berkeley, 1967.
- Chase, L. M., and K. A. Anderson, Spectral measurements of auroral-zone particles, Trans. Am. Geophys. Union, 48, 180, 1967.
- Coleman, P. J., L. Davis, and C. P. Sonett, Steady component of the interplanetary magnetic field: Pioneer V, Phys. Rev. Letters, 5, 43, 1960.
- Coppi, B., G. Laval, and R. Pellat, Dynamics of the geomagnetic tail, Phys. Rev. Letters, 16, 1207, 1966.
- Criswell, D. R., and B. J. O'Brien, Quadrant photometer for satellite-borne auroral and optical measurements, Applied Optics, 6, 1111, 1967.
- Davis, L. R., O. E. Berg, and L. H. Meredith, Direct measurements of particle fluxes in and near auroras, Space Research, ed. by H. K. Bijl, 721, 1960.
- Davis, T. N., The Aurora, Intro. to Space Science, ed. by W. N. Hess, 205, 1965.
- Dessler, A. J., Length of magnetospheric tail, J. Geophys. Res., 69, 3913, 1964.



- Dessler, A. J., Solar wind and interplanetary magnetic field, Rev. of Geophys., 5, 1, 1967.
- Dessler, A. J., Magnetic merging in the magnetospheric tail, J. Geophys. Res., 73, 209, 1968.
- Dessler, A. J., and R. D. Juday, Configuration of auroral radiation in space, Planet. Space Sci., 13, 63, 1965.
- Dessler, A. J., and G. K. Walters, Hydromagnetic coupling between solar wind and magnetosphere, Planet. Space Sci., 12, 227, 1964.
- Dungey, J. W., Interplanetary magnetic field and the auroral zones, Phys. Rev. Letters, 6, 47, 1961.
- Dwight, H. B., Tables of Integrals and Other Mathematical Data, 4th ed., MacMillan, New York, 179, 1961.
- Eather, R. H., Auroral proton precipitation and hydrogen emissions, Rev. of Geophys., 5, 207, 1967.
- Evans, D. S., Low energy charged-particle detection using the continuous-channel electron multiplier, Rev. Sci. Instr., 36, 375, 1965.
- Evans, D. S., Rocket observations of low energy auroral electrons, Aurora and Airglow, ed. by Billy M. McCormac, Reinhold Publ. Corp., New York, 191, 1967a.
- Evans, D. S., The observation of a near monoenergetic flux of auroral electrons, Goddard Space Flt. Center Preprint, X-611-67-487, 1967b.
- Evans, D. S., Seminar on Auroral Electrons, Presented at Rice Univ., March, 1968.
- Evans, J. E., R. G. Johnson, R. D. Sharp, and J. B. Reagan, Recent results from satellite measurements of low-energy particles precipitated at high latitudes, Space Sci. Rev., 7, 263, 1967.
- Fairfield, D. H., and L. J. Cahill, Transition region magnetic field and polar magnetic disturbances, J. Geophys. Res., 71, 155, 1966.

- Fan, E. Y., G. Gloeckler, and J. A. Simpson, Evidence for >30 kev electrons accelerated in the shock transition region beyond the earth's magnetospheric boundary, Phys. Rev. Letters, 13, 149, 1964.
- Farnsworth, U. S. Patent 1,969, 399, 1930.
- Fejer, J. A., Theory of the geomagnetic daily disturbance variations, J. Geophys. Res., 69, 123, 1964.
- Feldstein, Y. I., Peculiarities in the auroral distribution and magnetic disturbance distribution in high latitudes caused by the asymmetrical form of the magnetosphere, Planet. Space Sci., 14, 121, 1966.
- Frank, L. A., Low-energy proton and electron experiment for the orbiting geophysical observatories B and E, Univ. of Iowa Rep. 65-22, 1965.
- Freeman, J. W., and J. J. Maguire, Gross local-time particle asymmetries at the synchronous orbit altitude, J. Geophys. Res., 72, 5257, 1967.
- Freeman, J. W., J. A. Van Allen, and L. J. Cahill, Explorer 12 observations of the magnetospheric boundary and the associated solar plasma on September 13, 1961, J. Geophys. Res., 68, 2121, 1963.
- Fritz, T. A., and D. A. Gurnett, Diurnal and latitudinal effects observed for 10 kev electrons, J. Geophys. Res., 70, 2485, 1965.
- Furth, H. P., The mirror instability for finite particle gyro radii, Nucl. Fusion, Supplement, part 1, 169, 1962.
- Gold, T., Magnetic fields in the solar system, Nuovo Cimento, Supplement, 10, 13, 318, 1959.
- Goldstein, H., Classical Mechanics, Addison-Wesley, Reading, Mass., 107, 1950.
- Gosling, J. T., J. R. Asbridge, S. J. Bame, and I. B. Strong, Vela 2 measurements of the magnetopause and bow shock positions, J. Geophys. Res., 72, 101, 1967.

- Gringauz, K. I., Lunik I, Unpublished, 1959.
- Hagstrum, H. D., Theory of auger ejection of electrons from metals by ions, Phys. Rev., 96, 336, 1954.
- Heppner, J. P., M. Sugiura, T. L. Skillman, B. D. Ledley, and M. Campbell, OGO-A magnetic field observations, J. Geophys. Res., 72, 5417, 1967.
- Hoffman, R. A., and D. S. Evans, OGO-4 auroral particles experiment and calibration, Goddard Space Flt. Center Preprint X-611-67-632, 1967.
- Hoh, F. C., Acceleration processes and the tail of the magnetosphere, Boeing Document DI-82-0457, 1965.
- Hoh, F. C., Stability of a sheet pinch, Phys. Fluids, 9, 277, 1966.
- Hoh, F. C., and A. Bers, Resonant particle energy transfer to magnetic perturbations with application to the geomagnetic tail, Boeing Document DI-82-0589, 1966.
- Jackson, J. D., Classical Electrodynamics, John Wiley, New York, 1963.
- Johnson, M. C., and J. Svenson, Absolute quantum efficiency of a channeltron photomultiplier, Bendix Corp. Rep., 1965.
- Kennel, C. F., and H. E. Petschek, Limit on stably trapped particle fluxes, J. Geophys. Res., 71, 1, 1966.
- Konradi, A., Electron and proton fluxes in the tail of the magnetosphere, J. Geophys. Res., 71, 2317, 1966.
- Laval, G., and R. Pellat, Methode d'etude de la stabilite de certaines solutions d l'equation de Vlasov., Compt. Rend., 259, 1706, 1964.
- Laval, G., R. Pellat, and M. Vuillemin, Instabilites electromagnetiques des plasmas sans collisions, Proceedings of the Second International Conference on Plasma Physics and Thermonuclear Fusion (International Atomic Energy Agency, Vienna, 1965), Paper CN-21/71.

- Lin, W. C., I. B. McDiarmid, and J. R. Burrows, Electron fluxes at 1000-km altitude associated with auroral substorms, Canadian J. Phys., 46, 80, 1968.
- Maehlum, B. N., Universal time control of the low energy electron fluxes in the polar regions, To be published, J. Geophys. Res., 73, June 1, 1968.
- Maehlum, B. N., and B. J. O'Brien, Study of energetic electrons and their relationship to auroral absorption of radio waves, J. Geophys. Res., 68, 997, 1963.
- McDaniel, E. W., Collision Phenomena in Ionized Gases, John Wiley, New York, 1964.
- McDiarmid, I. B., and E. E. Budzinski, Angular distribution and energy spectra of electrons associated with auroral events, Canadian J. Phys., 42, 2048, 1964.
- McDiarmid, I. B., E. E. Budzinski, B. A. Whalen, N. Sckopke, Rocket observations of electron pitch-angle distributions during auroral substorms, Canadian J. Phys., 45, 1755, 1967.
- McDiarmid, I. B., and J. R. Burrows, Electron fluxes at 1000 km associated with the tail of the magnetosphere, J. Geophys. Res., 70, 3031, 1965.
- McDiarmid, I. B., and J. R. Burrows, Local time asymmetries in the high-latitude boundary of the outer radiation zone for the different electron energies, Canadian J. Phys., 46, 49, 1968.
- McIlwain, C. E., Direct measurement of particles producing visible aurorae, J. Geophys. Res., 65, 2727, 1960.
- McIlwain, C. E., Coordinates for mapping the distribution of magnetically trapped particles, J. Geophys. Res., 66, 3681, 1961.
- Mead, G. D., Deformation of the geomagnetic field by the solar wind, J. Geophys. Res., 69, 1181, 1964.
- Mead, G. D., and D. B. Beard, Shape of the geomagnetic field solar wind boundary, J. Geophys. Res., 69, 1169, 1964.

- Michel, F. C., Nonthermal properties of a postshock plasma, Phys. Fluids, 8, 1283, 1965.
- Montgomery, M. D., Observations of electrons in the earth's magnetotail by Vela launch 2 satellites, J. Geophys. Res., 73, 871, 1968.
- Montgomery, M. D., S. Singer, J. P. Conner, and E. E. Stogsdill, Spatial distribution, energy spectra and time variations of energetic electrons ( $E \geq 50$  kev) at 17.7 earth radii, Phys. Rev. Letters, 14, 209, 1965.
- Mott, N. F., and H. S. W. Massey, The Theory of Atomic Collisions, 3rd ed., Oxford Univ. Press, London, 502, 1965.
- Mozer, F. S., Rocket measurements of energetic particles, 3, proton results, J. Geophys. Res., 70, 5717, 1965.
- Mozer, F. S., and P. Bruston, Observation of the low-altitude acceleration of auroral protons, J. Geophys. Res., 71, 2201, 1966.
- Ness, N. F., The earth's magnetic tail, J. Geophys. Res., 70, 2989, 1965.
- Neugebauer, M., and C. W. Snyder, Mariner 2 observations of the solar wind, 1, average properties, J. Geophys. Res., 71, 4469, 1966.
- Neugebauer, M., and C. W. Snyder, Mariner 2 observations of the solar wind, 2, relation of plasma properties to the magnetic field, J. Geophys. Res., 72, 1823, 1967.
- Nishida, A., Formation of a plasmopause, or magnetospheric plasma knee by combined action of magnetospheric convection and plasma escape from the tail, J. Geophys. Res., 71, 5669, 1966.
- Northrop, T. G., Adiabatic charged-particle motion, in Plasma Physics in Theory and Application, ed. by W. B. Kunkel, McGraw-Hill Book Co., New York, 1966.
- O'Brien, B. J., A large diurnal variation of the geomagnetically trapped radiation, J. Geophys. Res., 68, 989, 1963.

- O'Brien, B. J., High-latitude geophysical studies with satellite Injun 3, part 3, precipitation of electrons into the atmosphere, J. Geophys. Res., 69, 13, 1964.
- O'Brien, B. J., Auroral Phenomena, Science, 148, 449, 1965.
- O'Brien, B. J., Interrelations of energetic charged particles in the magnetosphere, Solar-Terrestrial Physics, ed. by J. W. King and W. S. Newman, Academic Press, London, ch. 6, 1967.
- O'Brien, B. J., C. D. Laughlin, and D. A. Gurnett, High-latitude geophysical studies with satellite Injun 3, part 1, description of the satellite, J. Geophys. Res., 69, 1, 1964.
- O'Brien, B. J., C. D. Laughlin, J. A. Van Allen, and L. A. Frank, Measurements of the intensity and spectrum of electrons at 1000-kilometer altitude and high latitudes, J. Geophys. Res., 67, 1209, 1962.
- O'Brien, B. J., F. Abney, J. Burch, R. Harrison, R. LaQuey, and T. Winiecki, SPECS, a versatile space-qualified detector of charged particles, Rev. Sci. Instr., 38, 1058, 1967.
- Parker, E. N., Sweet's mechanism for merging magnetic fields in conducting fluids, J. Geophys. Res., 62, 509, 1957a.
- Parker, E. N., Newtonian development of the dynamical properties of ionized gases of low density, Phys. Rev., 107, 924, 1957b.
- Pfirsch, D., Instabilitäten vom Spiegel Typ, Z. Naturforschung, 17a, 861, 1962.
- Ploch, Massenabhängigkeit der Elektronenauslösung durch isotope Ionen, Z. Physik, 130, 174, 1951.
- Reasoner, D. L., Rocket measurement of auroral alpha particles, To be published, J. Geophys. Res., 1968.
- Reid, G. C., and R. Parthasarathy, Ionospheric effects of energetic electron bursts in the tail of the magnetosphere, J. Geophys. Res., 71, 3267, 1966.

- Sandford, B. P., Aurora and airglow intensity variations with time and magnetic activity at southern high latitudes, J. Atmos. Terr. Phys., 26, 749, 1964.
- Schmidt, K. C., and C. F. Hendee, Continuous channel electron multiplier operated in the pulse saturated mode, IEEE Trans. Nucl. Sci., NS-13, 100, 1966.
- Sharp, R. D., and R. G. Johnson, Satellite measurements of auroral particle precipitation, To be published in Proc. of the Advanced Study Institute on Earth's Particles and Fields, Freising, Germany, July 31 - Aug. 11, 1967.
- Sharp, R. D., R. G. Johnson, M. F. Shea, and G. B. Shook, Satellite measurements of precipitating protons in the auroral zone, J. Geophys. Res., 72, 227, 1967.
- Sharp, R. D., and R. G. Johnson, Some average properties of auroral electron precipitation as determined from satellite observations, J. Geophys. Res., 73, 969, 1968.
- Sonett, C. P., E. J. Smith, and A. R. Sims, Surveys of the distant geomagnetic field: Pioneer 1 and Explorer 6, Space Research, ed. by H. K. Kallmann-Bijl, 921, 1960.
- Speiser, T. W., Particle trajectories in model current sheets, 1; analytical solutions, J. Geophys. Res., 70, 4219, 1965.
- Sternglass, E. J., Theory of secondary electron emission by high-speed ions, Phys. Rev., 108, 1, 1957.
- Stringer, W. J., and A. E. Belon, The morphology of the IQSY auroral oval, 1, interpretation of isoauroral diagrams, J. Geophys. Res., 72, 4415, 1967.
- Swift, D. W., Mechanism for energizing electrons in the magnetosphere, J. Geophys. Res., 70, 3061, 1965.
- Synge, J. L., and B. A. Griffith, Principles of Mechanics, 3rd ed., McGraw-Hill, New York, 333, 1959.
- Taylor, H. E., and E. W. Hones, Adiabatic motion of auroral particles in a model of the electric and magnetic fields surrounding the earth, J. Geophys. Res., 70, 3605, 1965.

- Van Allen, J. A., Direct detection of auroral radiation with rocket equipment, Proc. Nat'l Acad. U. S., 43, 57, 1957.
- Van Allen, J. A., The geomagnetically trapped corpuscular radiation, J. Geophys. Res., 64, 1683, 1959.
- Vasyliunas, V., A survey of low energy electrons in the evening sector of the magnetosphere with OGO-1 and OGO-3, Submitted to J. Geophys. Res., Dec., 1967.
- Vegard, L., On the properties of the rays producing aurorae borealis, Phil. Mag., 23, 211, 1912.
- Vegard, L., Emission spectra of night sky and aurora, Reports of the Gassiot Committee, 82, The Physical Society of London, 1948.
- Walbridge, E., The limiting of magnetospheric convection by dissipation in the ionosphere, J. Geophys. Res., 72, 5213, 1967.
- Westerlund, L. H., Rocket-borne observations of the auroral electron energy spectra and their pitch-angle distribution, PhD Thesis, Rice Univ., 1968.
- Whalen, B. A., I. B. McDiarmid, and E. E. Budzinski, Rocket measurements in proton aurora, Canad. J. Phys., 45, 3247, 1967.
- Williams, D. J., and G. D. Mead, Nightside magnetosphere configurations as obtained from trapped electrons at 1100 kilometers, J. Geophys. Res., 70, 3017, 1965.
- Williams, D. J., and W. F. Palmer, Distortions in the radiation cavity as measured by an 1100 kilometer polar orbiting satellite, J. Geophys. Res., 70, 557, 1965.
- Winckler, J. R., Atmospheric phenomena, energetic electrons and the geomagnetic field, Tech. Rep. CR-40, Univ. of Minn., 1961
- Wolfe, J. H., R. W. Silva, and M. A. Myers, Preliminary results from the Ames research center plasma probe observations of the solar wind geomagnetic field interaction region on IMP 2 and OGO 1, Space Res. VI, 680, 1966.



Woolridge, D. E., Theory of secondary emission, Phys. Rev.,  
56, 562, 1939.

FIGURE CAPTIONS

Figure 1: Sketch of approximate magnetosphere configuration and several particle domains as viewed by O'Brien, 1967.

Figure 2: Spectra of electron counting rates versus energy, measured in the magnetosheath and plasma sheet. These spectra are relative differential energy spectra multiplied by energy. (Bame et al., 1967).

Figure 3: Latitudinal positions of the "centers" of the various regions of precipitation as observed during the Lockheed 1965 flight. Data from both the northern and southern hemispheres are included. The centers of the proton regions are defined as the location of peak flux in a 21 kev threshold detector. The centers of the electron regions are the estimated "centers of gravity" of the total precipitated energy as determined by a 15 ev threshold detector (night zone), a 9 kev threshold detector (hard day zone), and a differential detector with center energy near 1 kev (soft day zone).

Figure 4: Photograph of Aurora 1 satellite, showing solar panels, antennas, and viewing ports of the two photometers.

Figure 5: Sketch of Aurora 1, showing the various structures, detectors, and telemetry modules. Principal axes are indicated.

Figure 6: Block diagram of a typical channel in the Aurora 1 analog telemetry.

Figure 7: Maximum deviation of the Aurora 1 detector axis from the local geomagnetic vector as a function of time after launch.

Figure 8: Euler angles as used in this thesis (Goldstein, 1950).

Figure 9: Photograph of a Bendix Model CEM-4010 channel multiplier. Inner diameter of tube is 1 mm. Tube length is 101 mm.

Figure 10: Photograph of a Bendix Model CEM-4028 helical channel multiplier.

Figure 11: Typical plot of secondary electron output per incident primary electron as a function of primary energy.  $\delta$  is the number of secondaries emitted.

Figure 12: Typical differential energy distribution of secondary electrons for primary electrons of energy  $E_p$ .

Figure 13: (a) The normal electron energy diagram of a metal;  $\phi$  is the work function, and  $\epsilon_0$  is the depth of the conduction band with respect to the level of zero kinetic energy in the continuum. (b) The energy diagram modified by the approach of an ion (with ionization potential  $V_i$ ) within a distance  $S$  of the surface.  $\alpha$  and  $\beta$  are the depths with respect to the level of zero kinetic energy of the energy levels of electrons 1 and 2 respectively. (McDaniel, 1964).

Figure 14: Absolute efficiency of a Bendix channel multiplier for counting electrons as a function of primary

electron energy (Frank, 1965).

Figure 15: Absolute efficiency of a Bendix channel multiplier for counting  $\text{Li}^+$  as a function of primary  $\text{Li}^+$  kinetic energy (Frank, 1965). Also plotted is an approximate efficiency curve for  $\text{H}^+$ , assuming that the efficiency is a function only of ionic charge and velocity.

Figure 16: Sketch of the SPECS energy analyzer geometry, showing approximate locations of apertures, deflection plates, and channel multipliers.

Figure 17: Nominal energy passbands of SPECS for electrons and protons. These passbands were generated by calculations based on a simplified SPECS geometry and experimental measurements with a preliminary SPECS breadboard.

Figure 18: Aurora 1 SPECS system block diagram, showing high voltage power supply, channel multiplier charge-sensitive amplifiers, and related logic circuitry.

Figure 19: Experimental measurement of spread in beam energy of the electron accelerator used in calibration of the Aurora 1 SPECS. The data is presented in terms of the output current of a faraday cup mounted behind a retarding grid to which variable voltage is applied.

Figure 20: Typical angular response curves of a SPECS channel at various electron energies. This particular set of curves was obtained from Channel 3 (plate voltage 350 V) of a detector similar to the Aurora 1 SPECS.

Figure 21: Sketch of relative response to an isotropic electron beam of the various Aurora 1 SPECS channels as a function of primary electron energy.

Figure 22: Geometric factors (the numbers by which count rates are divided to yield flux in particles  $\text{cm}^{-2} \text{ster}^{-1} \text{ev}^{-1} \text{sec}^{-1}$ ) for the Aurora 1 SPECS channels which are used in this thesis.

Figure 23: Sketch of typical experimental curves of response versus incident electron energy for two different flux levels, which were used in determining the true versus apparent count rate relations.

Figure 24: True versus apparent count rate relation for Channel 1 of the Aurora 1 SPECS. Solid line is theoretical curve assuming a Poisson distribution of intervals between particle counts, while the dots are experimental points.

Figure 25: Dead times and true versus apparent count rate relations for the six Aurora 1 SPECS channels, based on pre-launch measurements at a pressure of  $10^{-6}$  mm Hg.

Figure 26: Absolute efficiency of a Bendix channel multiplier for counting electrons as a function of primary electron energy as measured by Arnoldy. (Hoffman and Evans, 1967).

Figure 27: Sample of strip chart output of Aurora 1 analog data, showing detector scaler switches and housekeeping analog levels.

Figure 28: Response of Channel 6 during a northern

Hemisphere day-side pass through the polar regions, based on 0.5-sec. count rate averages taken once every 5 sec. Pitch angle ranges are derived from values transmitted once every 16 seconds. (June 30, 1967;  $K_p \sim 3$ ).

Figure 29: Response of Channel 6 during a southern hemisphere night-side pass through the polar regions (June 30, 1967;  $K_p \sim 3$ ).

Figure 30: Response of Channel 6 during a northern hemisphere night-side pass through the polar regions (June 30, 1967;  $K_p \sim 3$ ).

Figure 31: Diurnal variation of the position of the "auroral zone" and "soft zone" electron fluxes. Also shown are the average zone of 70% occurrence of visual aurora in the zenith (Feldstein, 1966) and the average latitude above which the fluxes of electrons ( $E \geq 35$  kev) at pitch angles close to  $90^\circ$  are at cosmic ray background (McDiarmid and Burrows, 1967).

Figure 32: Invariant latitude ( $\Lambda_1$ ) of the boundary between the hard and soft electron regions as a function of magnetic local time for various values of  $K_p$ .

Figure 33: Invariant latitude ( $\Lambda_2$ ) of the high-latitude boundary of the soft electron region as a function of magnetic local time for various values of  $K_p$ .

Figure 34: Invariant latitude ( $\Lambda_2$ ) of the night-side high-latitude boundary of the soft electron region as a function of universal time for  $K_p \leq 4$ . (Maehlum, 1968).

Figure 35: Differential flux in several SPECS channels during a pass through the polar regions, based on 0.1-sec. count rate averages taken once every 5 sec. Six-point differential spectra are plotted for a few selected points, with passbands defined by 10% response to a flat isotropic laboratory electron spectrum. (Day side;  $K_p$ ,  $K_c \sim 1$ ).

Figure 36: Same as Figure 35, (Night side;  $K_p$ ,  $K_c \sim 3$ ).

Figure 37: Same as Figure 35, (Night side;  $K_p$ ,  $K_c \sim 3$ ).

Figure 38: Same as Figure 35, except without six-point spectra, (Night side;  $K_p \sim 0+ - 1-$ ,  $K_c = 0$ ).

Figure 39: Differential proton flux in several SPECS channels during a pass through the polar regions, based on 0.1-sec. count rate averages taken once every 5 sec. Six-point differential spectra are plotted for a few selected points with passbands derived by correcting the electron passbands for proton efficiencies. (Night side;  $K_p$ ,  $K_c \sim 3$ ).

Figure 40: Same as Figure 39, (Night side;  $K_p \sim 0+ - 1-$ ,  $K_c = 0$ ).

Figure 41: Orientations of auroral forms during the development of the auroral substorm. (Akasofu, 1964).

Figure 42: Same as Figure 35. Night side;  $K_p$ ,  $K_c \sim 3$ ).

Figure 43: Same as Figure 39, except without six-point spectra. (Night side;  $K_p$ ,  $K_c \sim 3$ ).

Figure 44: Magnetogram from College, Alaska, for July 18, 1967, showing variations in the horizontal component of the

local geomagnetic vector.

Figure 45: Comparison of several electron spectra using the efficiency measurements of Frank and Arnoldy.

Figure 46: (a) Comparison of an Aurora 1 day-side "soft zone" electron spectrum with a spectrum obtained by the Lockheed experimenters in the same region. (b) Comparison of an Aurora 1 night-side proton spectrum with a spectrum obtained by the Lockheed experimenters. Both spectra were taken during periods of very weak magnetic activity.

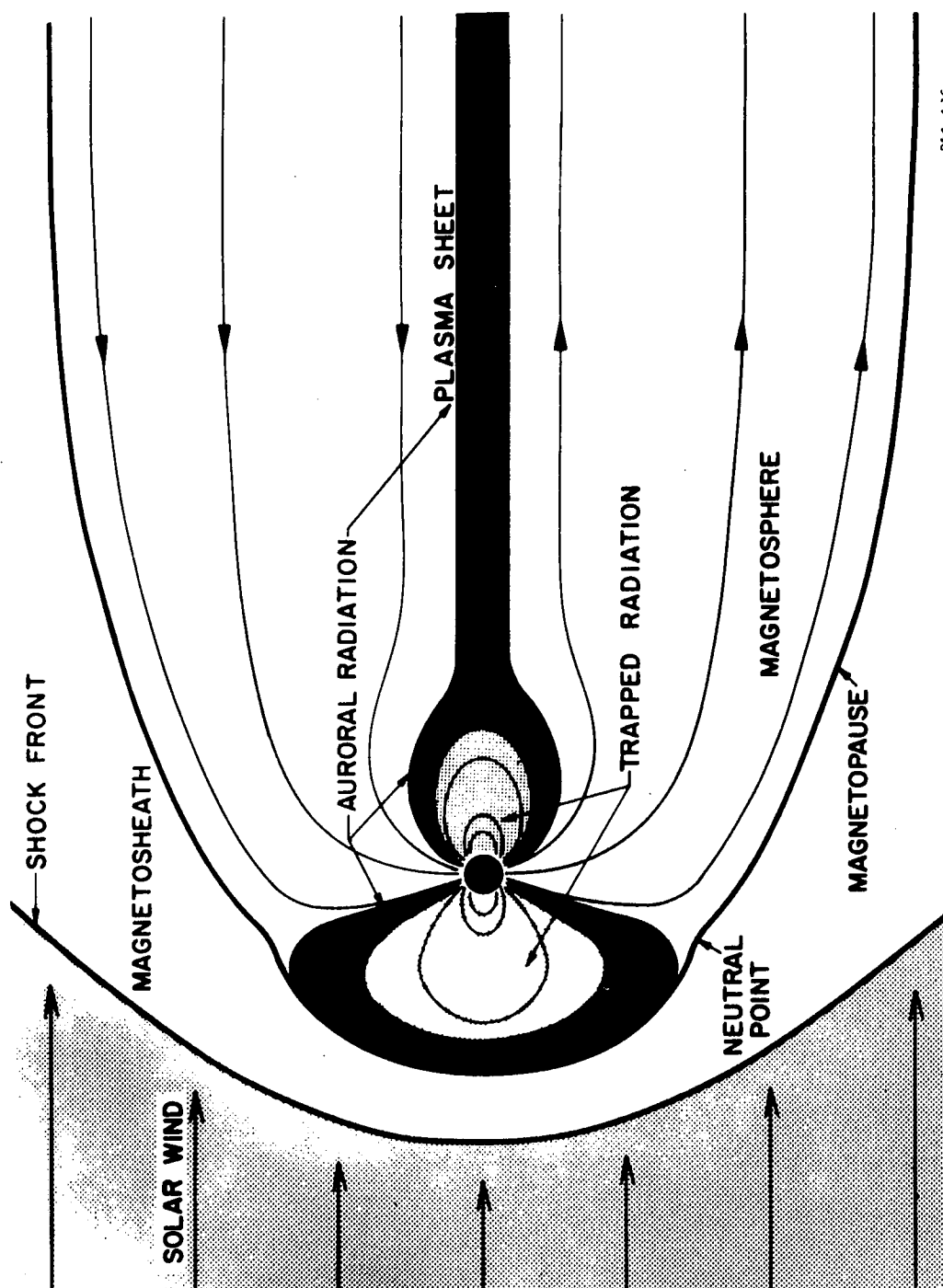
Figure 47: Comparison of an Aurora 1 electron spectrum obtained during magnetic bay activity (see Figure 42) with an electron spectrum measured by Evans, 1967a, on a sounding rocket in a post-breakup aurora.

Figure 48: The magnetic field configuration, electric field, and currents which result when the neutral sheet magnetic field experiences a perturbation of the form  $\bar{A}_1 = A_1(x) \exp(i\omega t + ixy) \hat{z}$ . (Hoh and Bers, 1966).

Figure 49: Two classes of electron trajectories in the neutral sheet magnetic field configuration. (Hoh and Bers, 1966).

Figure 50: Comparison of a directional differential electron spectra measured by the Aurora 1 SPECS in the night-side soft electron zone with an omnidirectional differential electron spectrum published by Montgomery, 1968, for the tail plasma sheet.





PS-4-10C

FIGURE 1

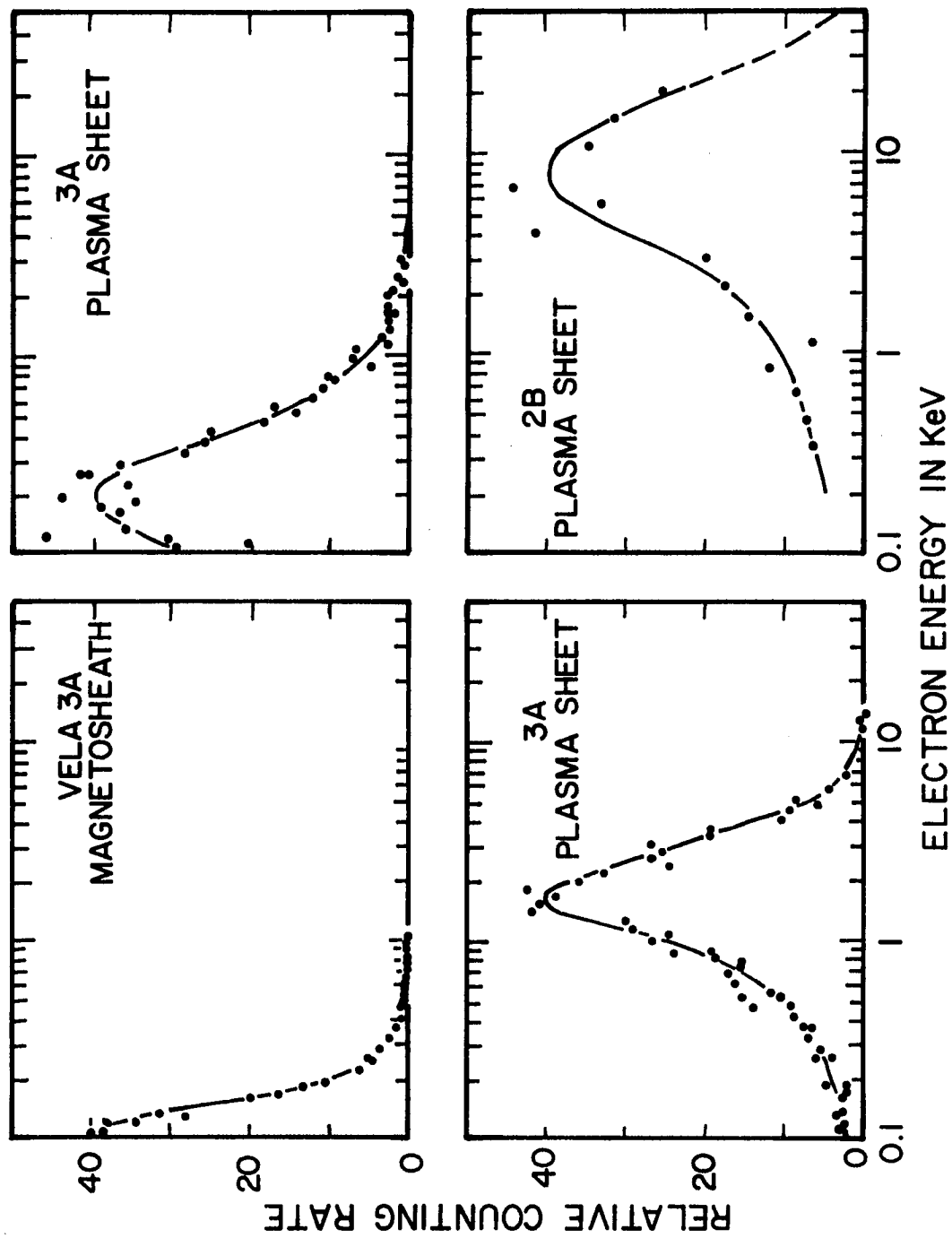


FIGURE 2

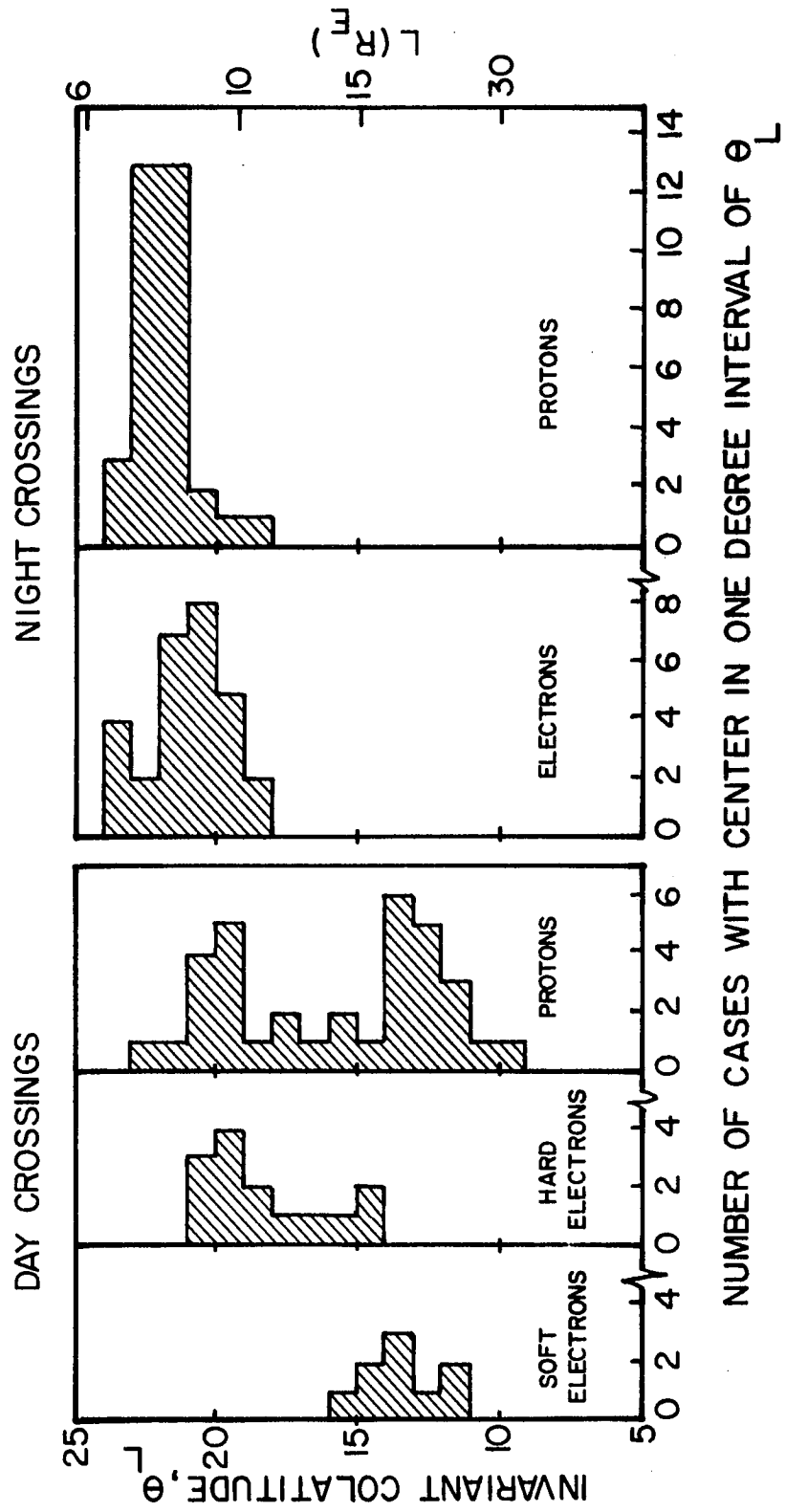


FIGURE 3

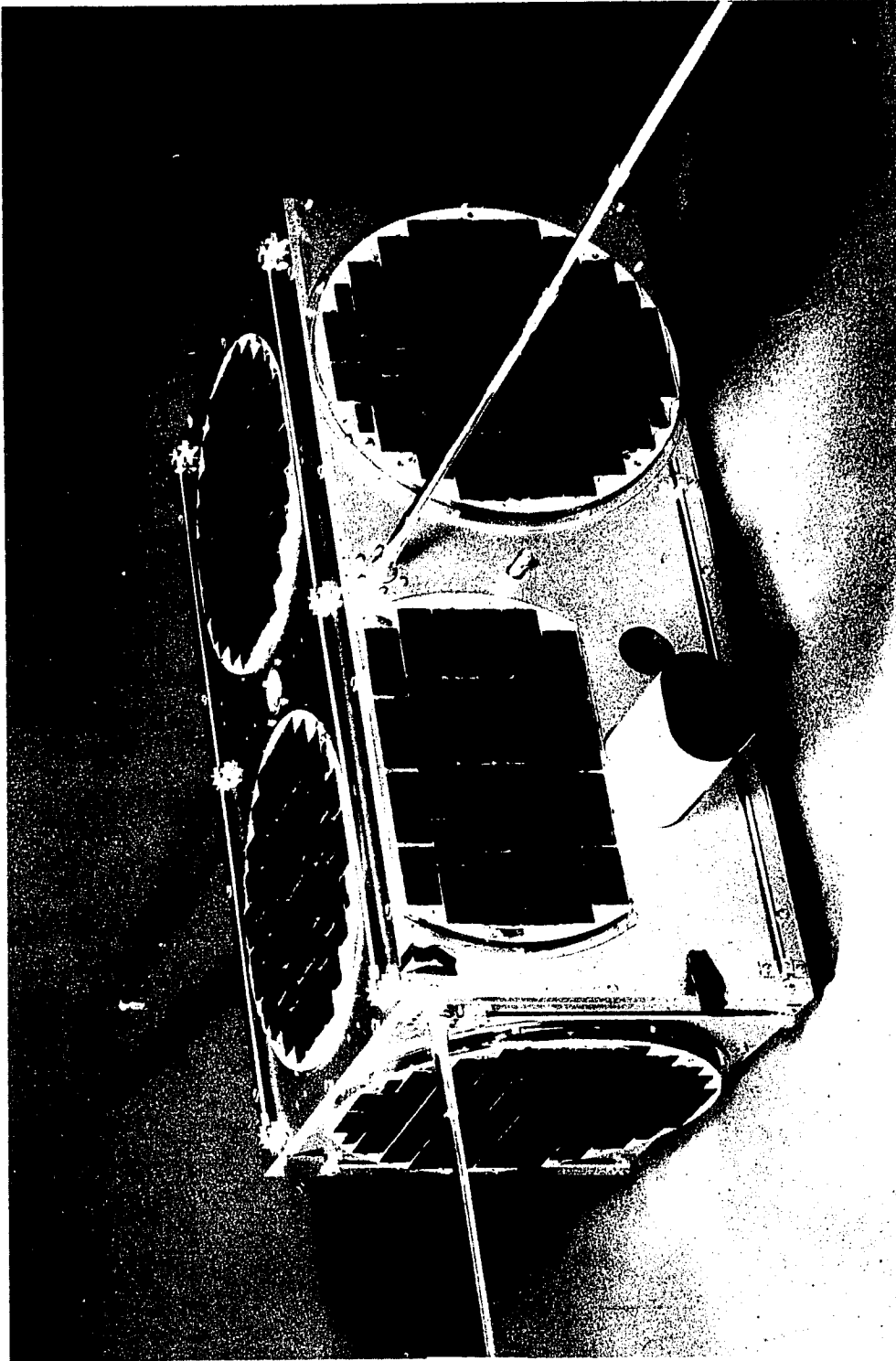


FIGURE 4

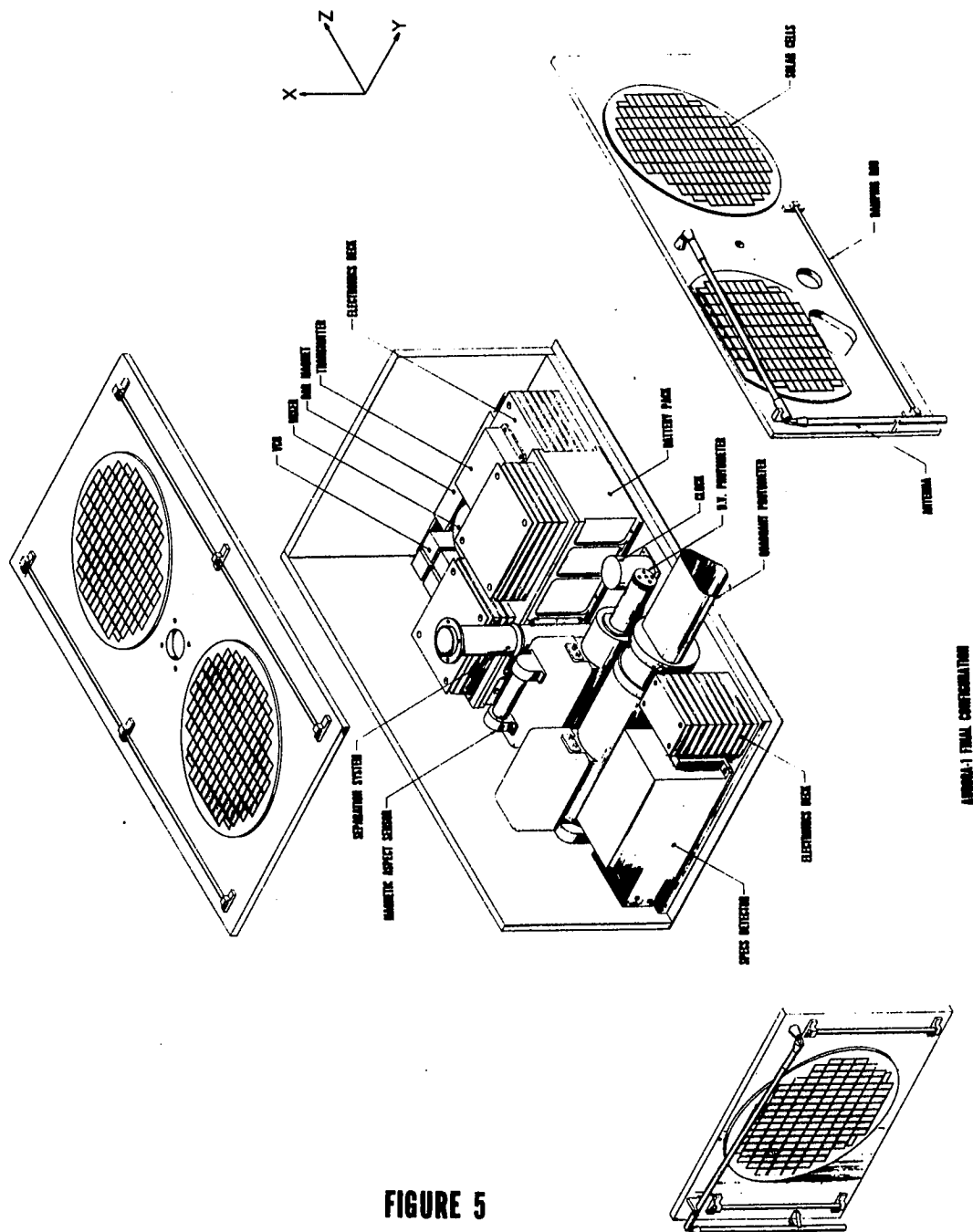
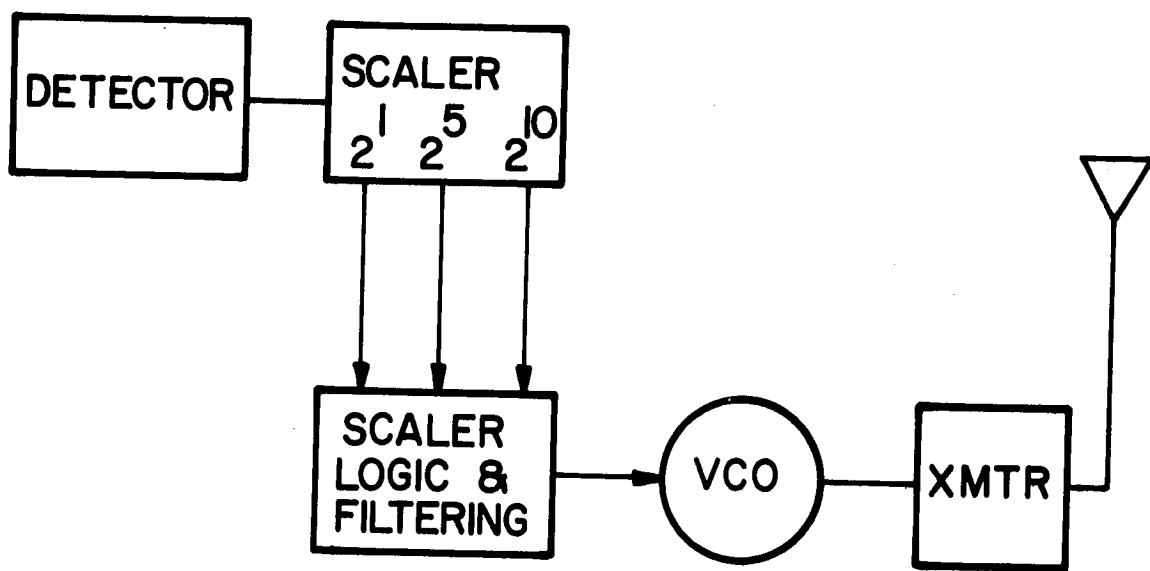


FIGURE 5

ARMOR-1 FINAL CONFIRMATION



TYPICAL TELEMETRY CHANNEL

FIGURE 6

## DEVIATION FROM MAGNETIC ALIGNMENT

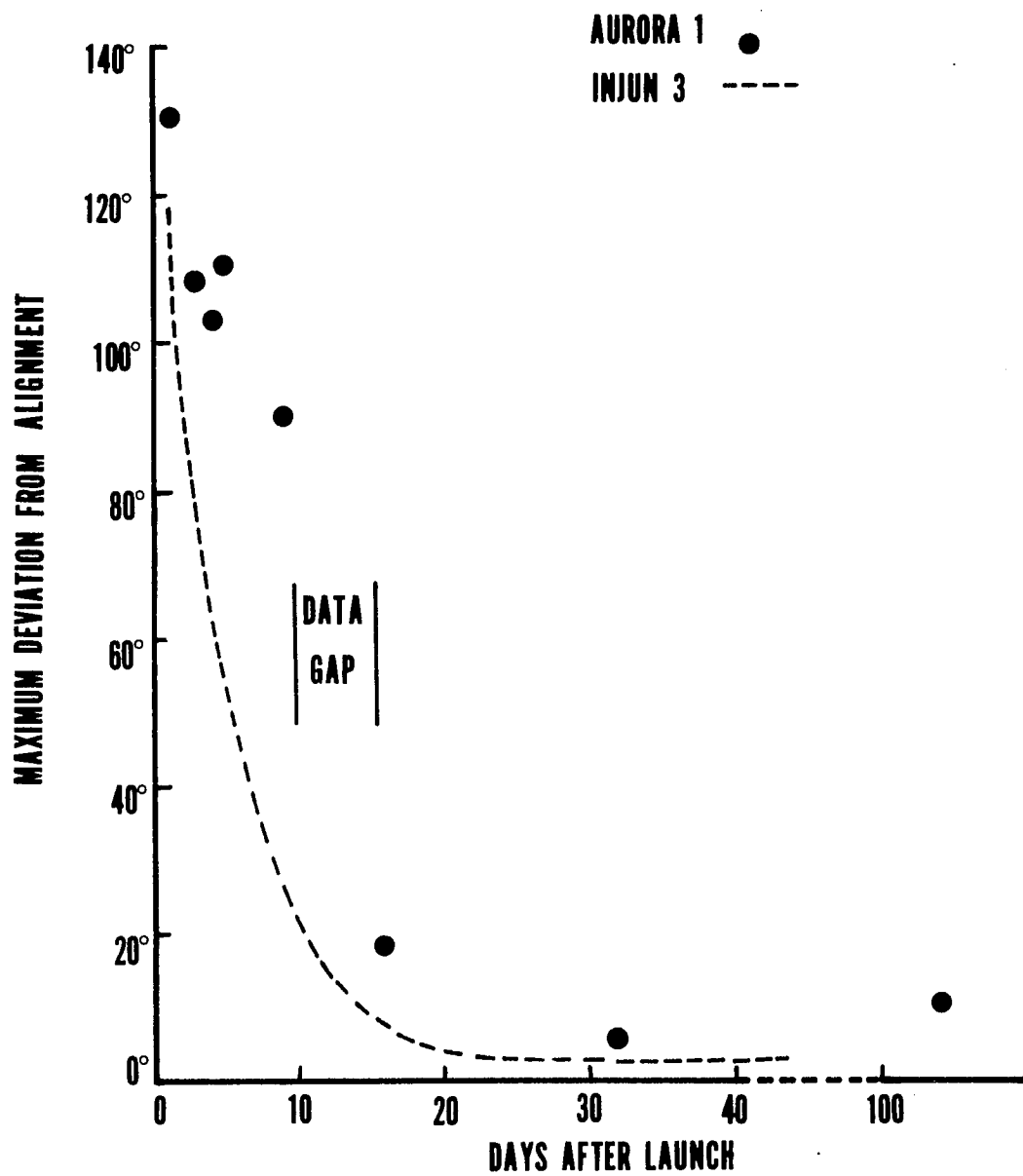


FIGURE 7

# EULER ANGLES

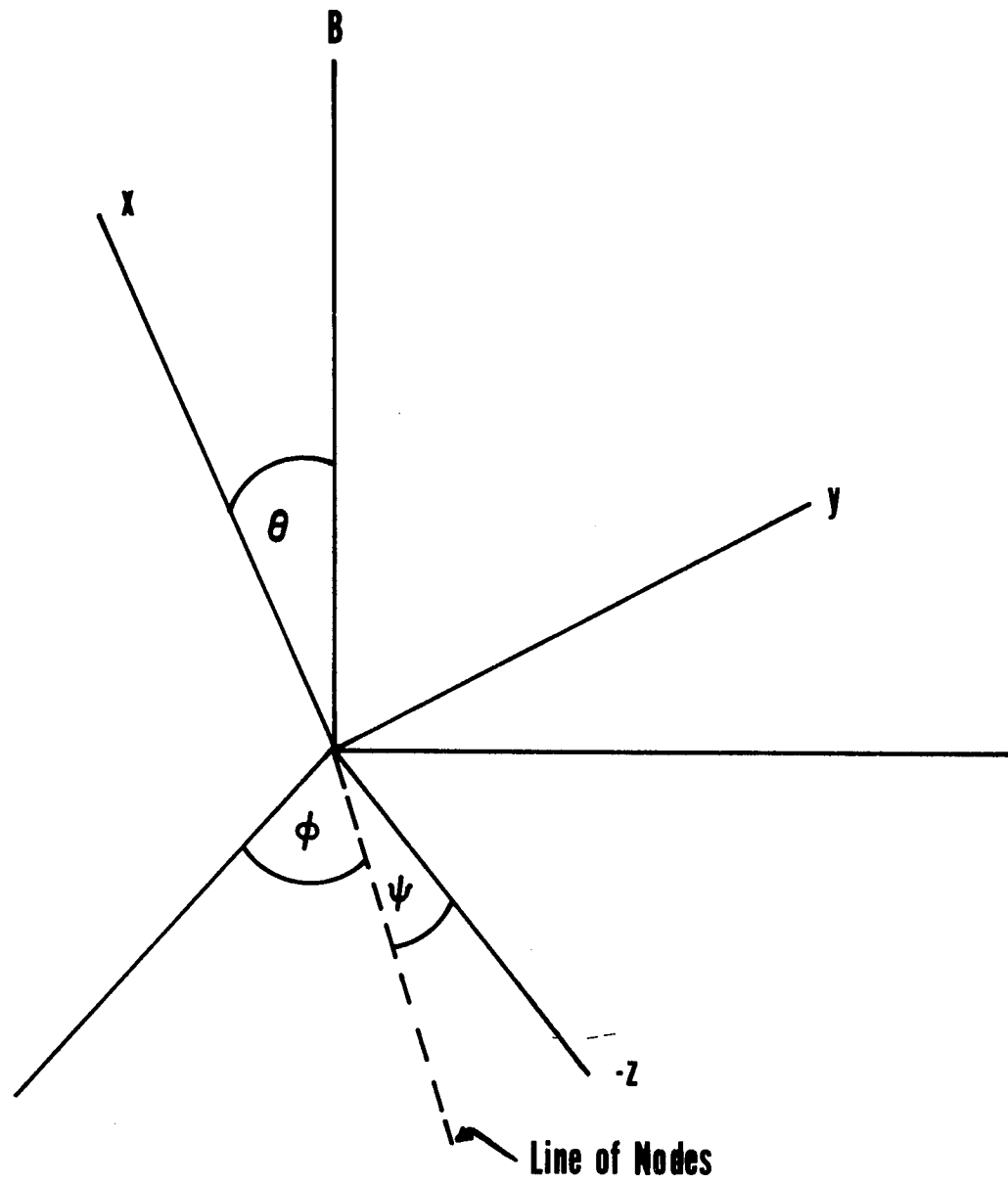


FIGURE 8



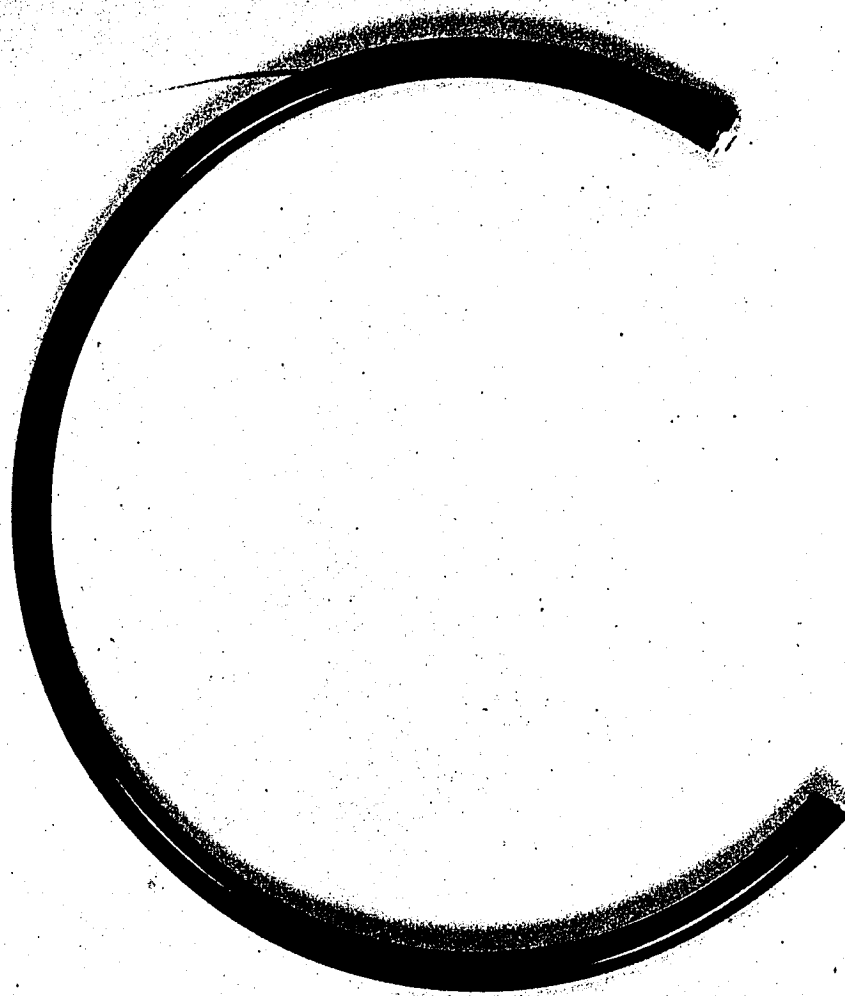
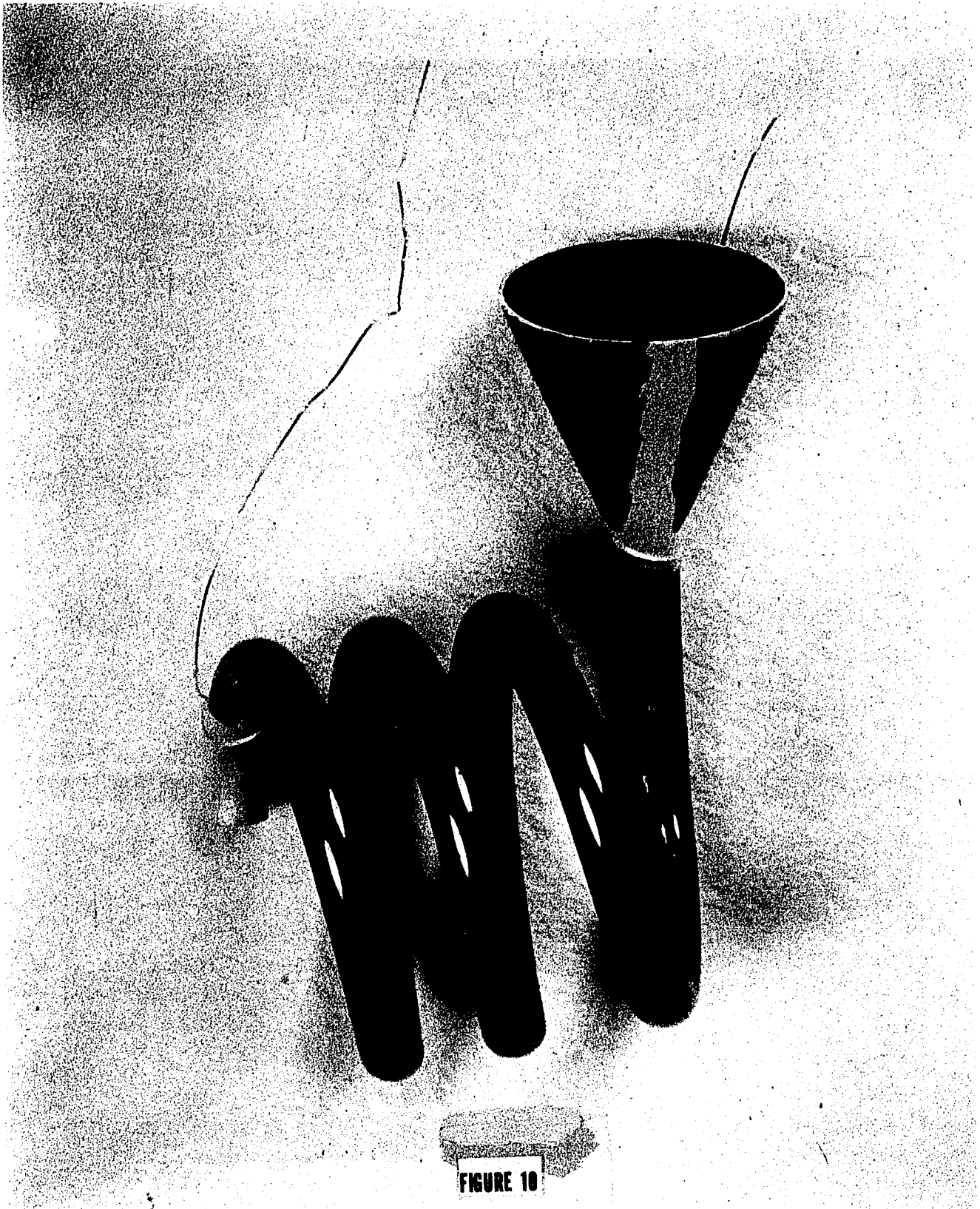


FIGURE 9



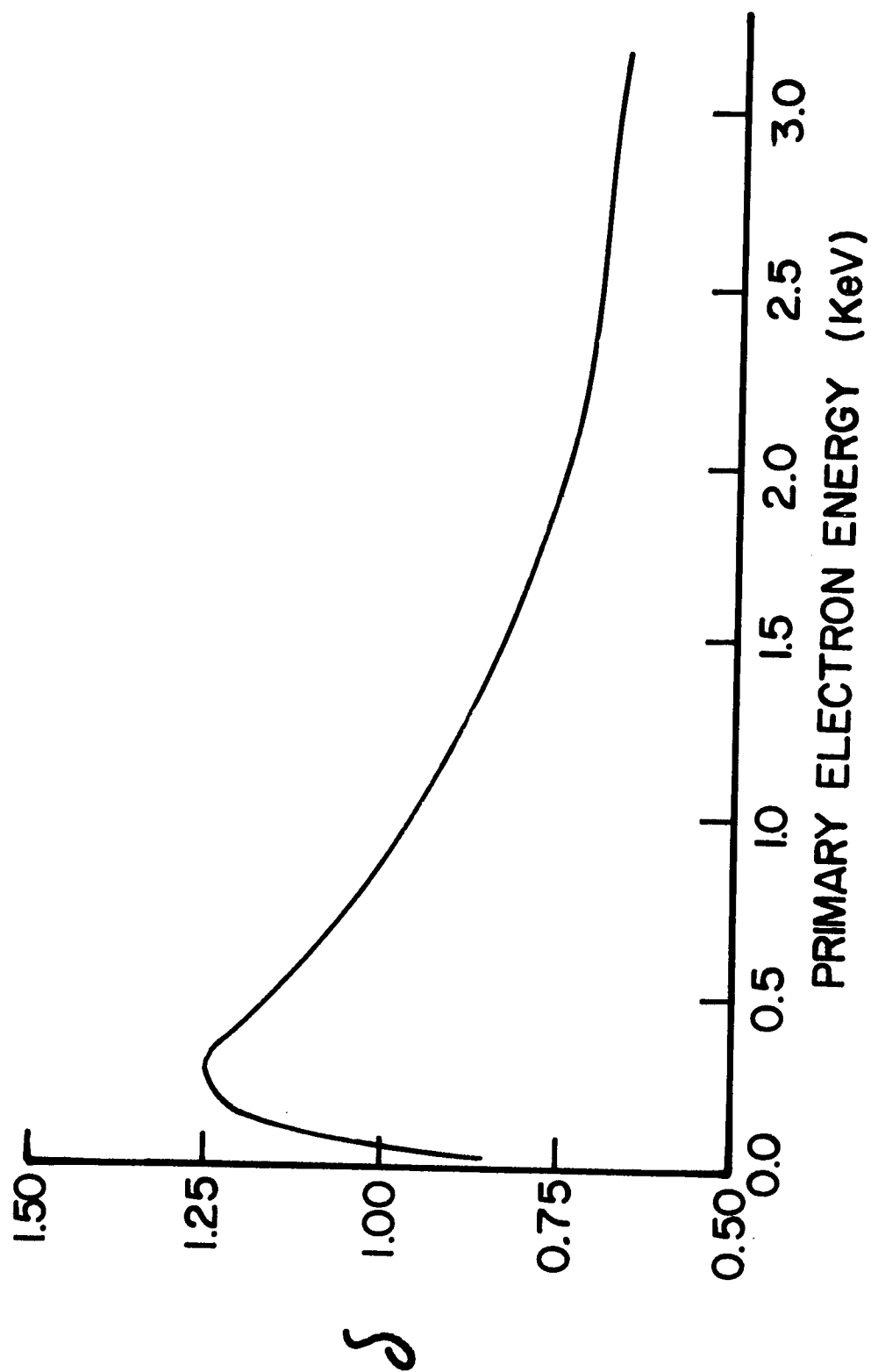


FIGURE 11

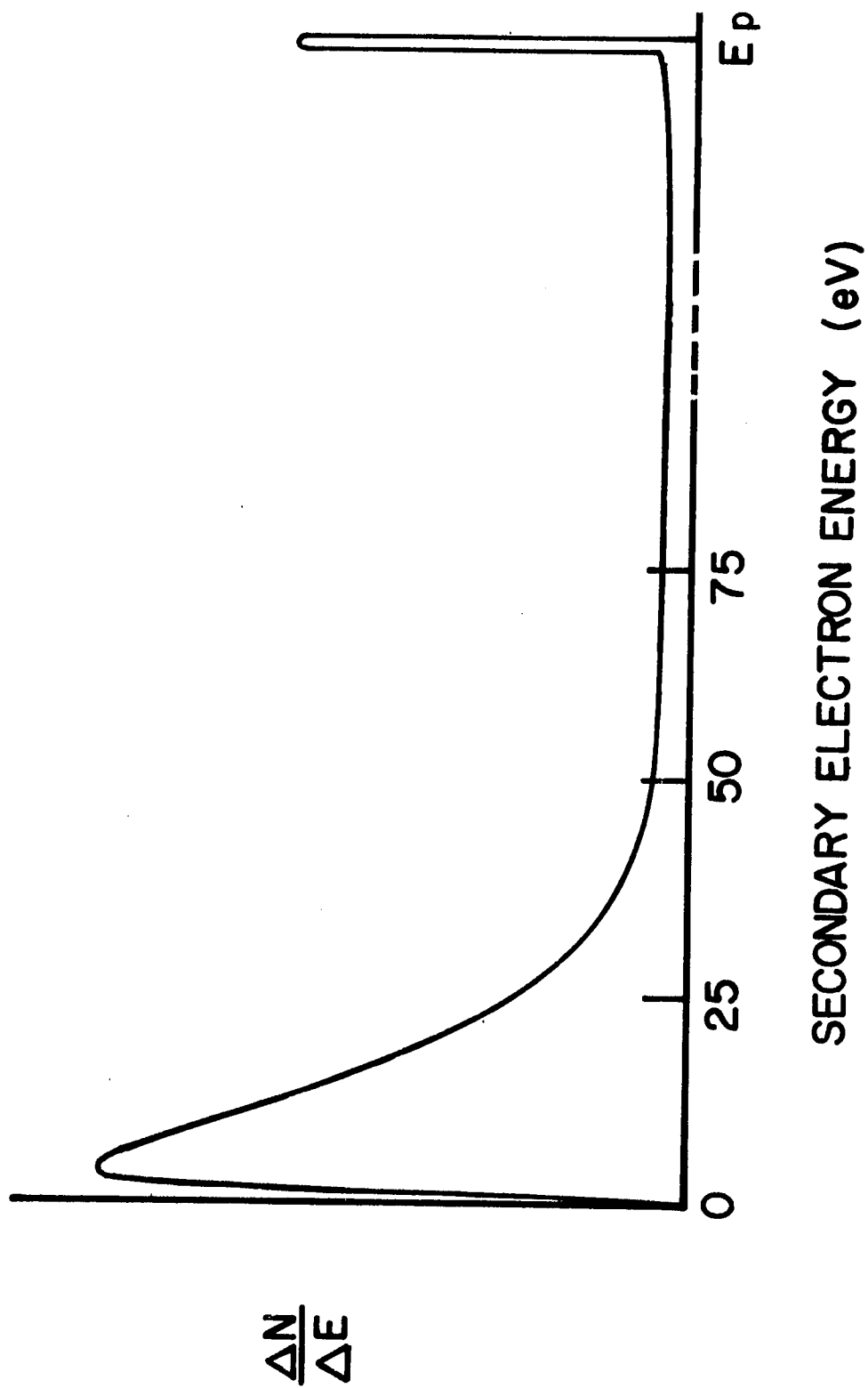


FIGURE 12

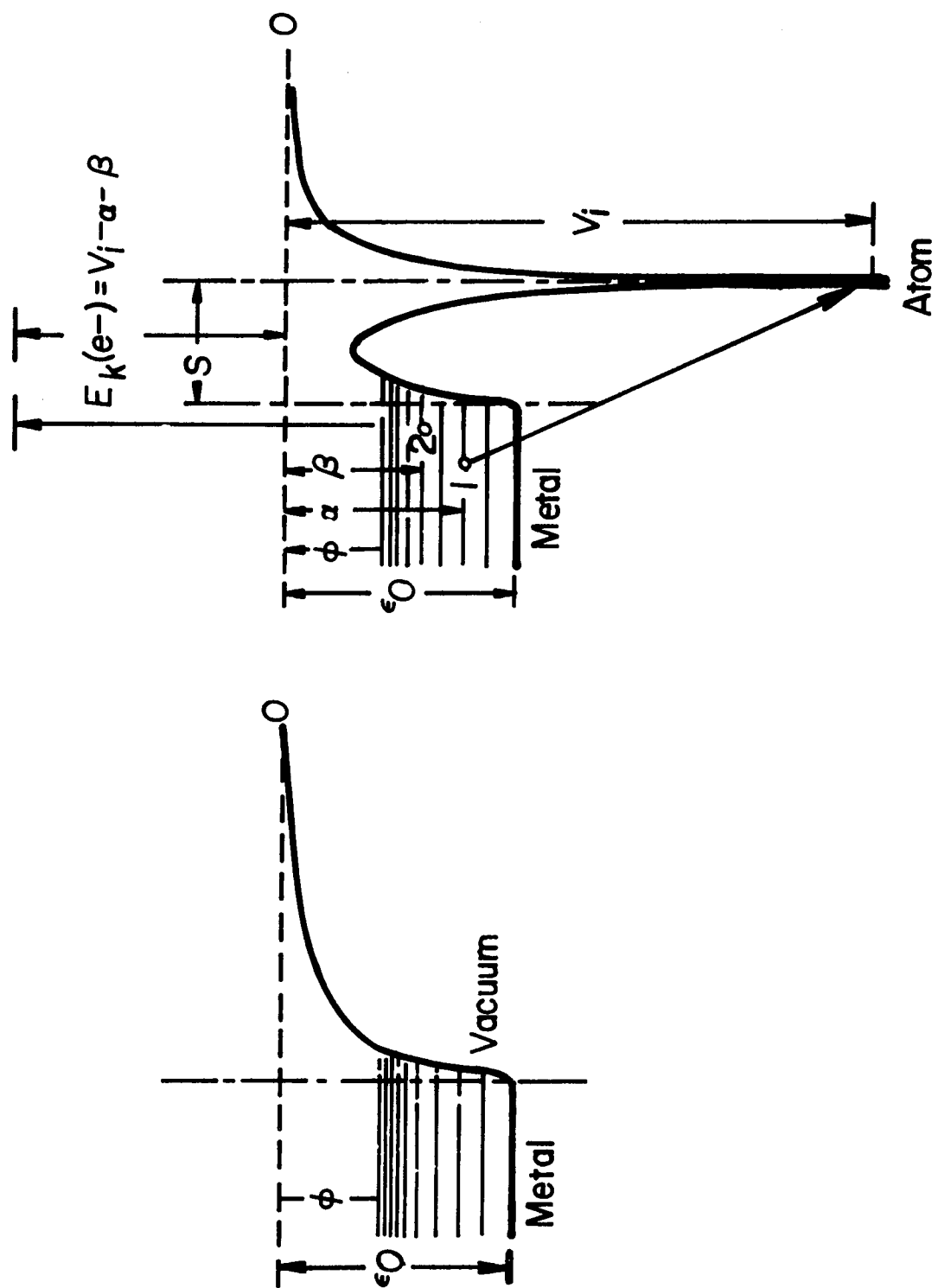


FIGURE 13

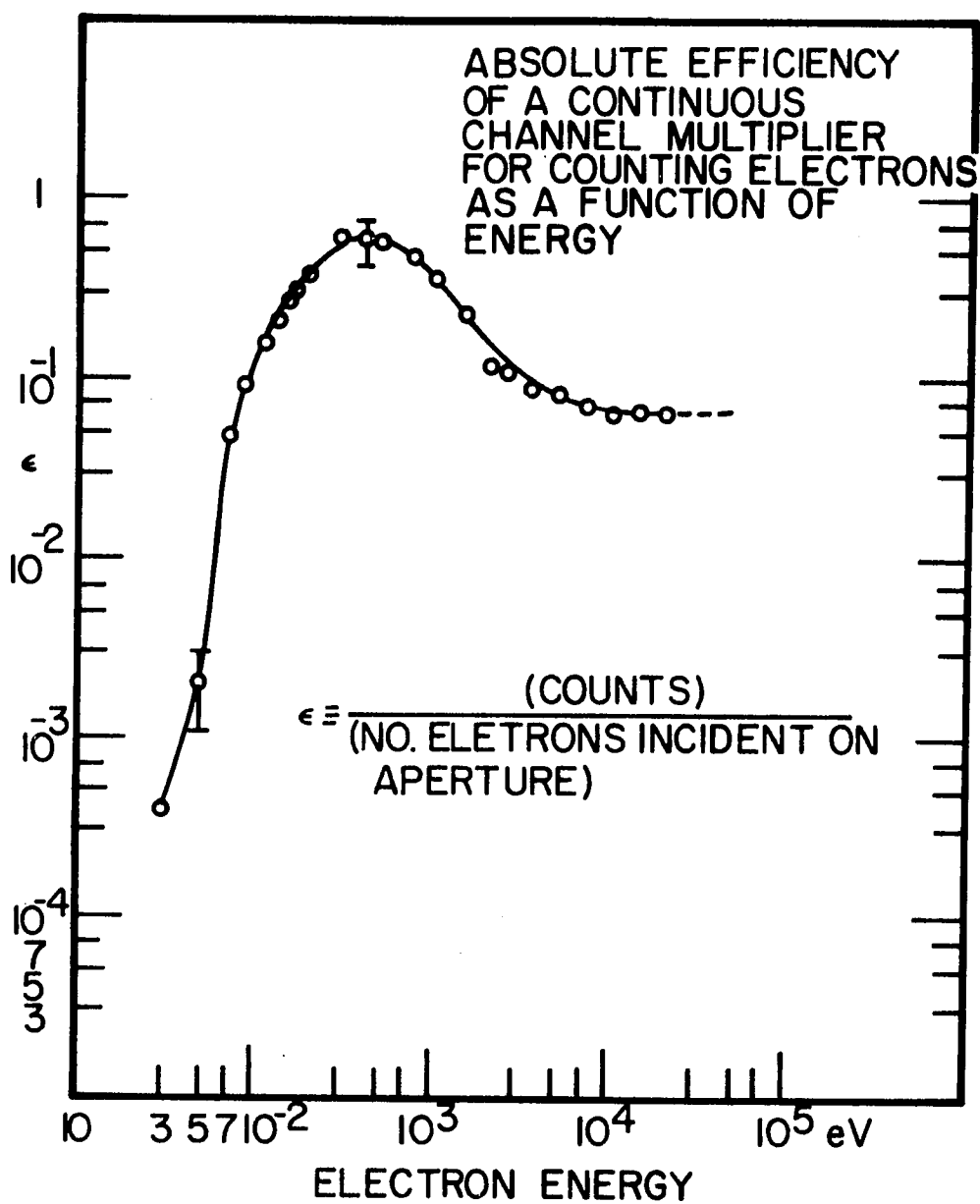


FIGURE 14

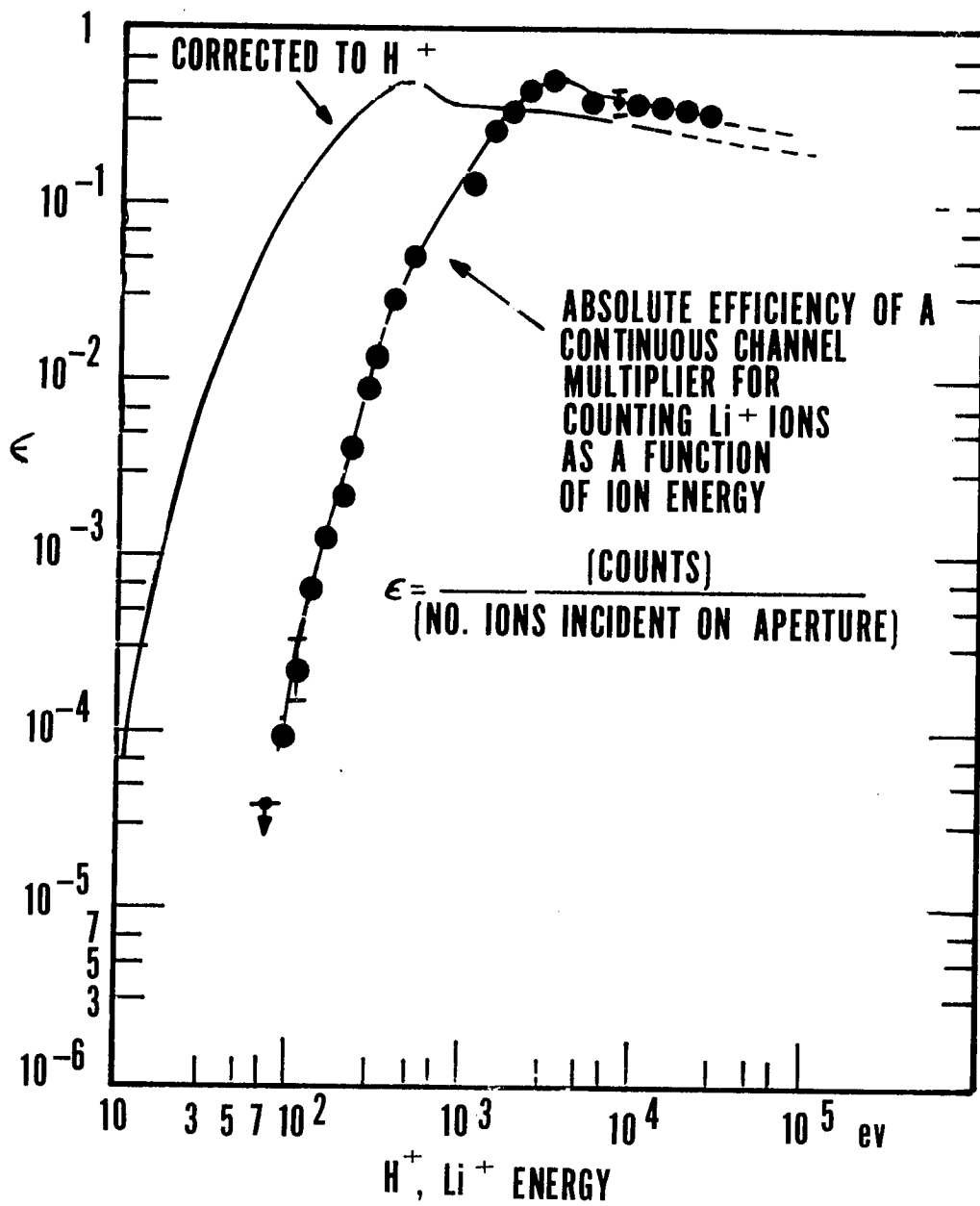
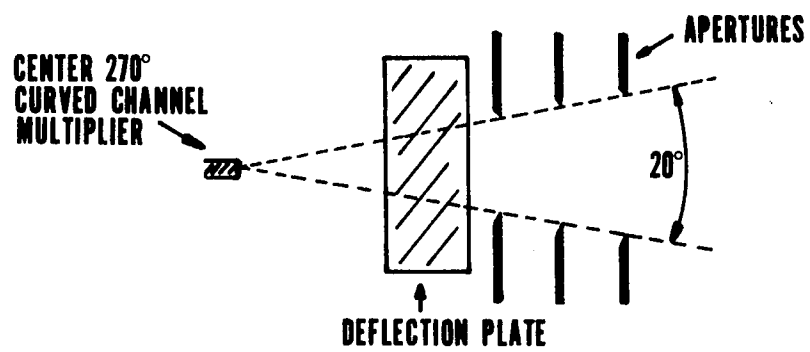
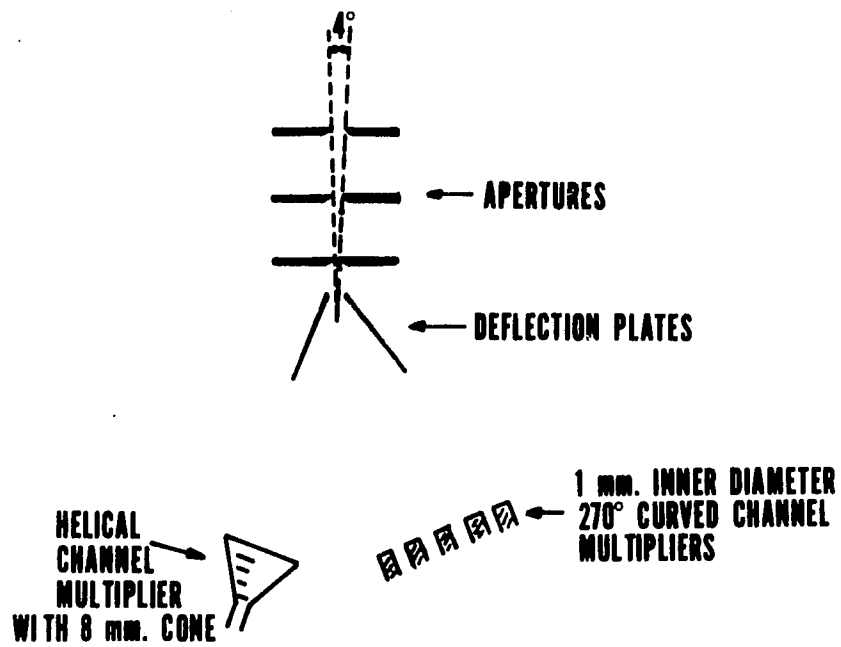
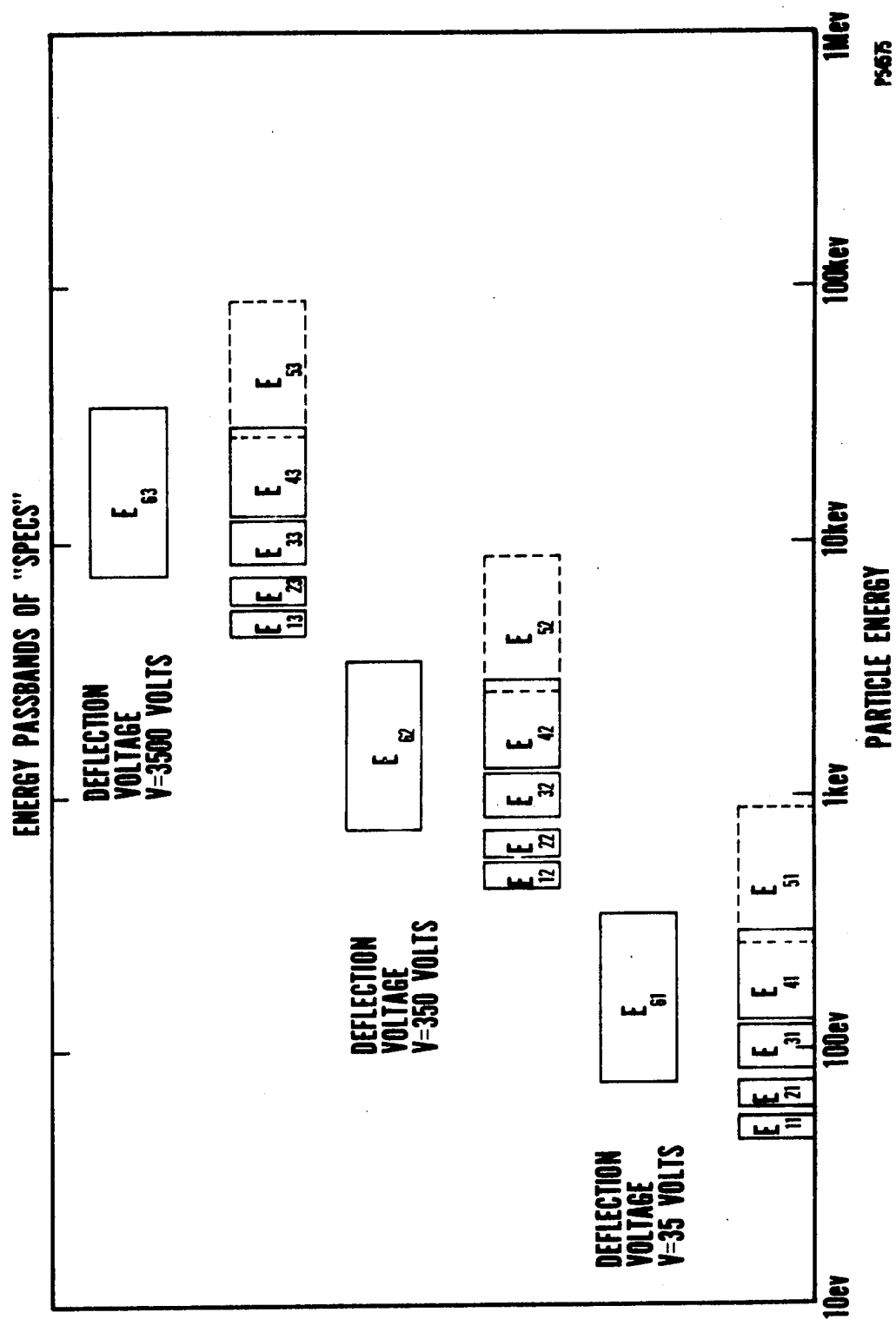


FIGURE 15

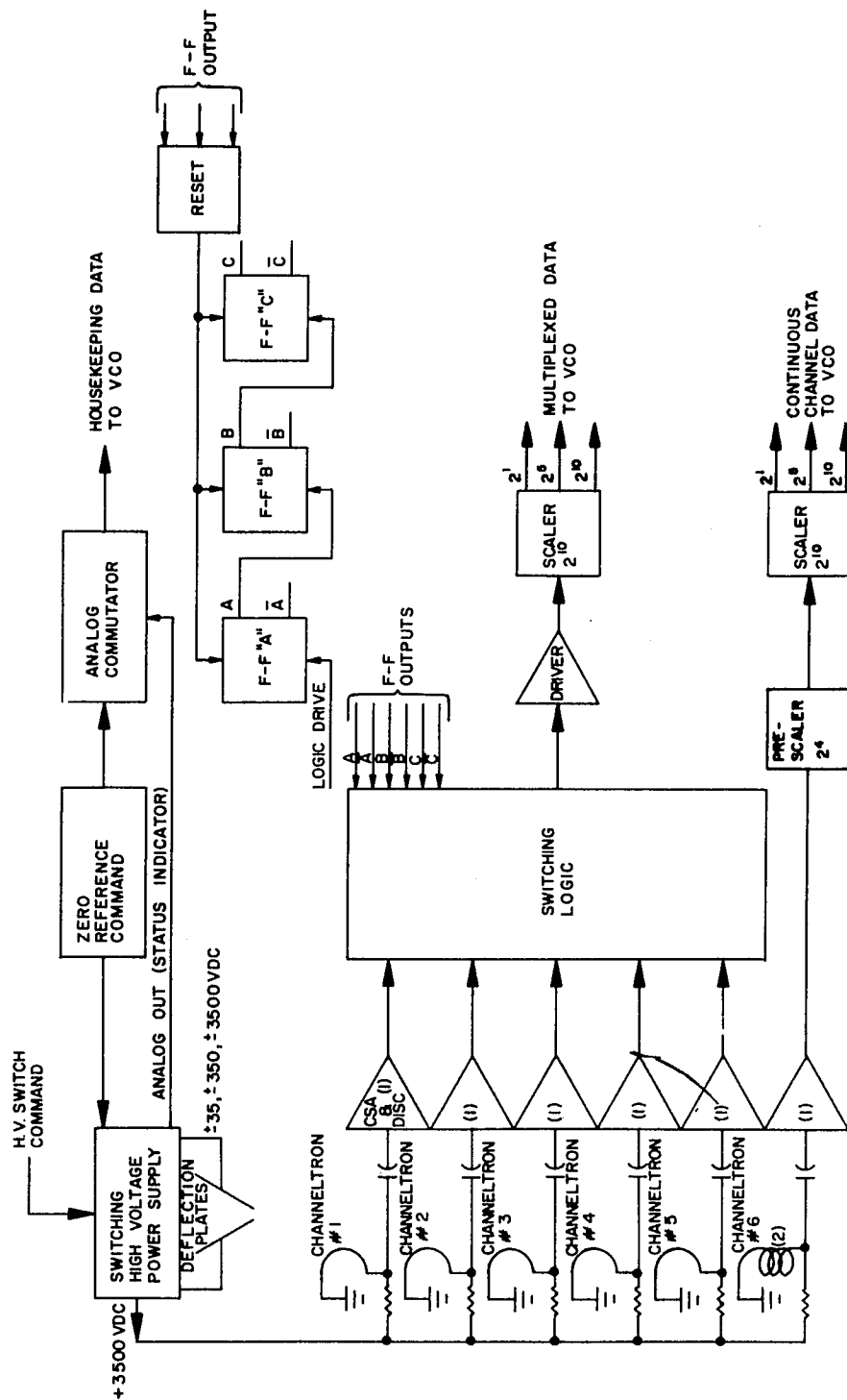


**FIGURE 16**





**FIGURE 17**



NOTES:

- (1) CHARGE-SENSITIVE AMPLIFIER & DISCRIMINATOR.
- (2) CHANNELTRON #6 IS HELICAL UNIT WITH 8 MM CONE APERTURE. ALL OTHERS CURVED 270° WITH 1MM APERTURE.

## AURORA SPECS SYSTEM BLOCK DIAGRAM

FIGURE 18

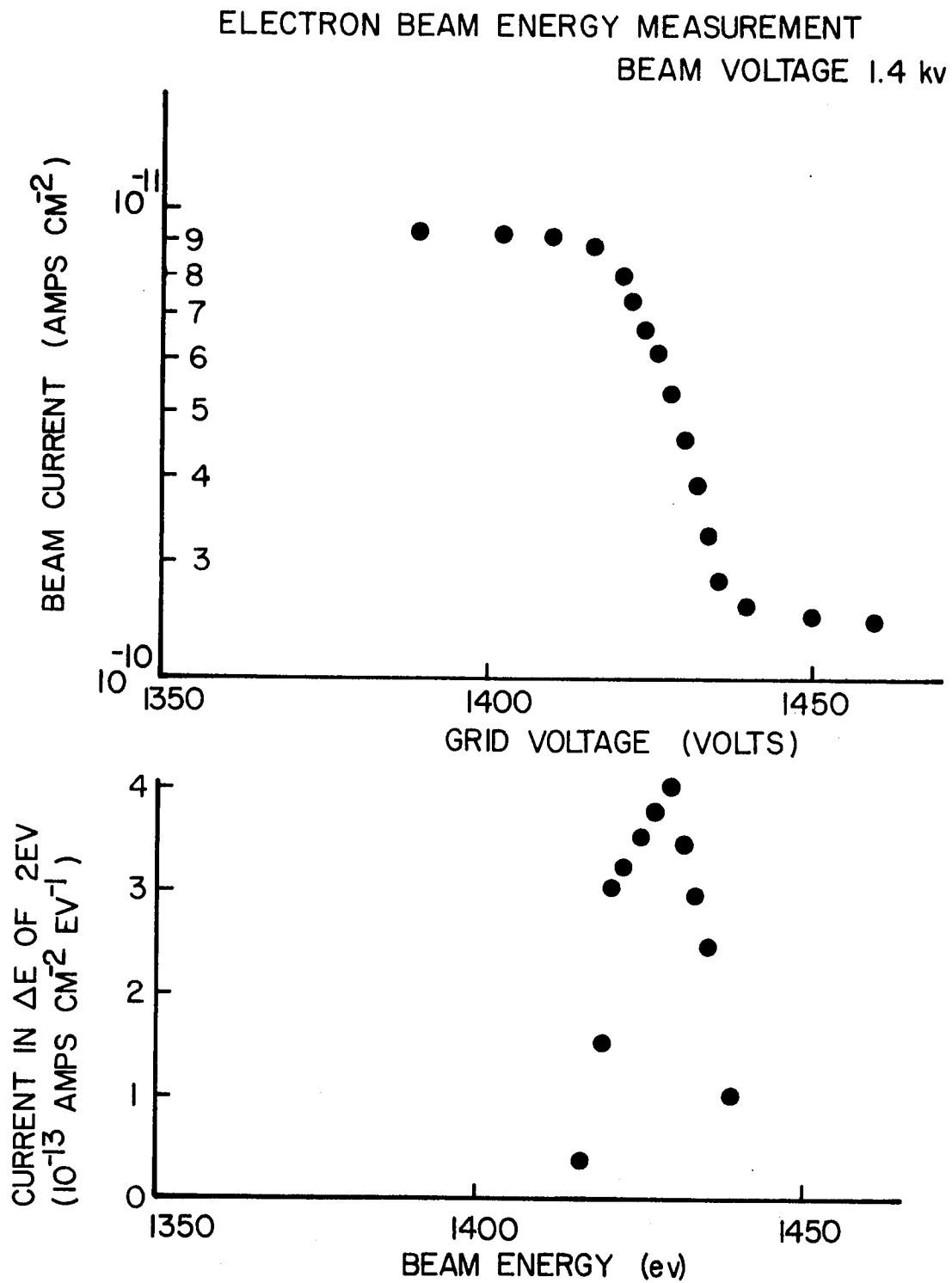
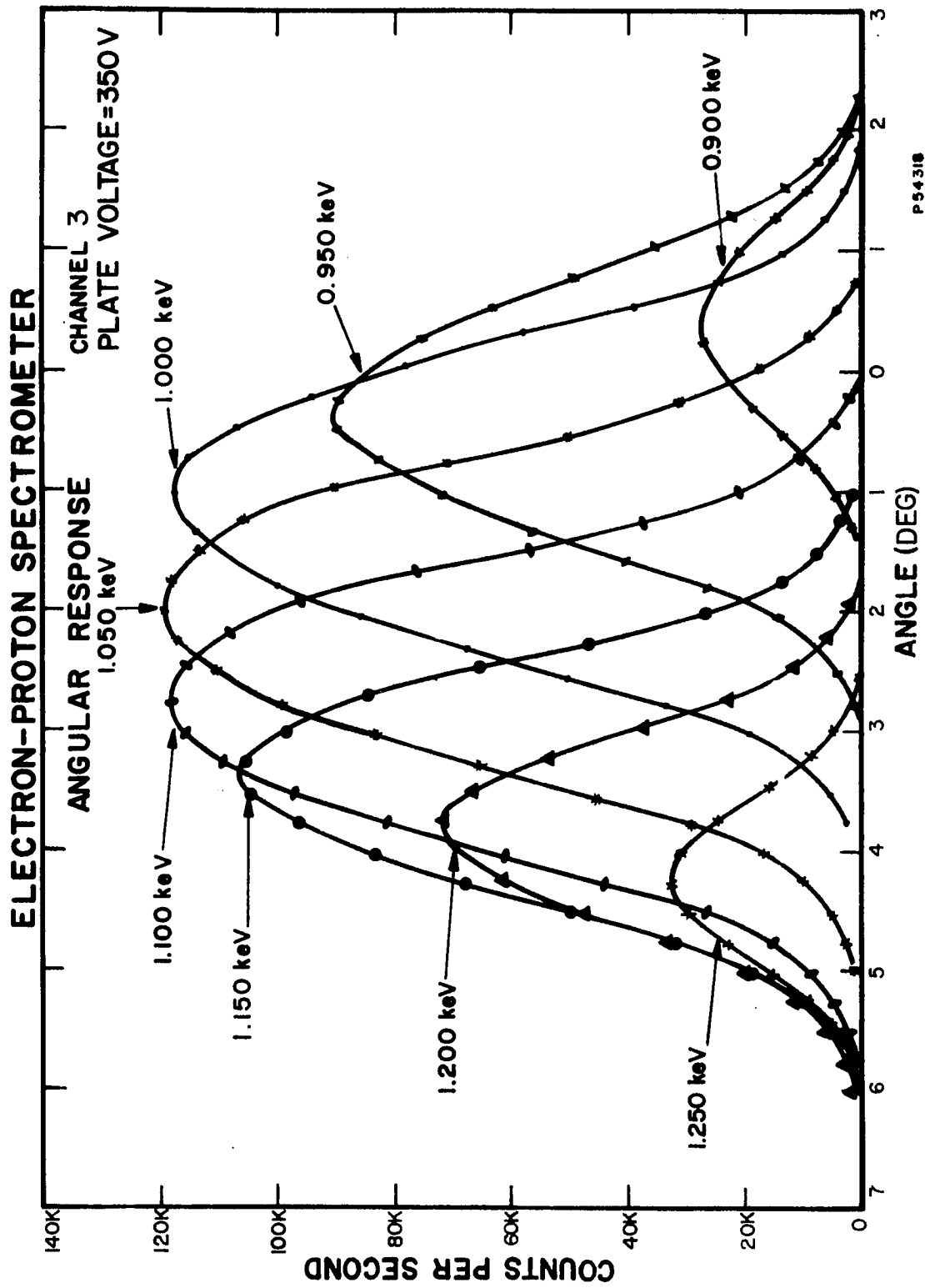


FIGURE 19



P 54318

FIGURE 20

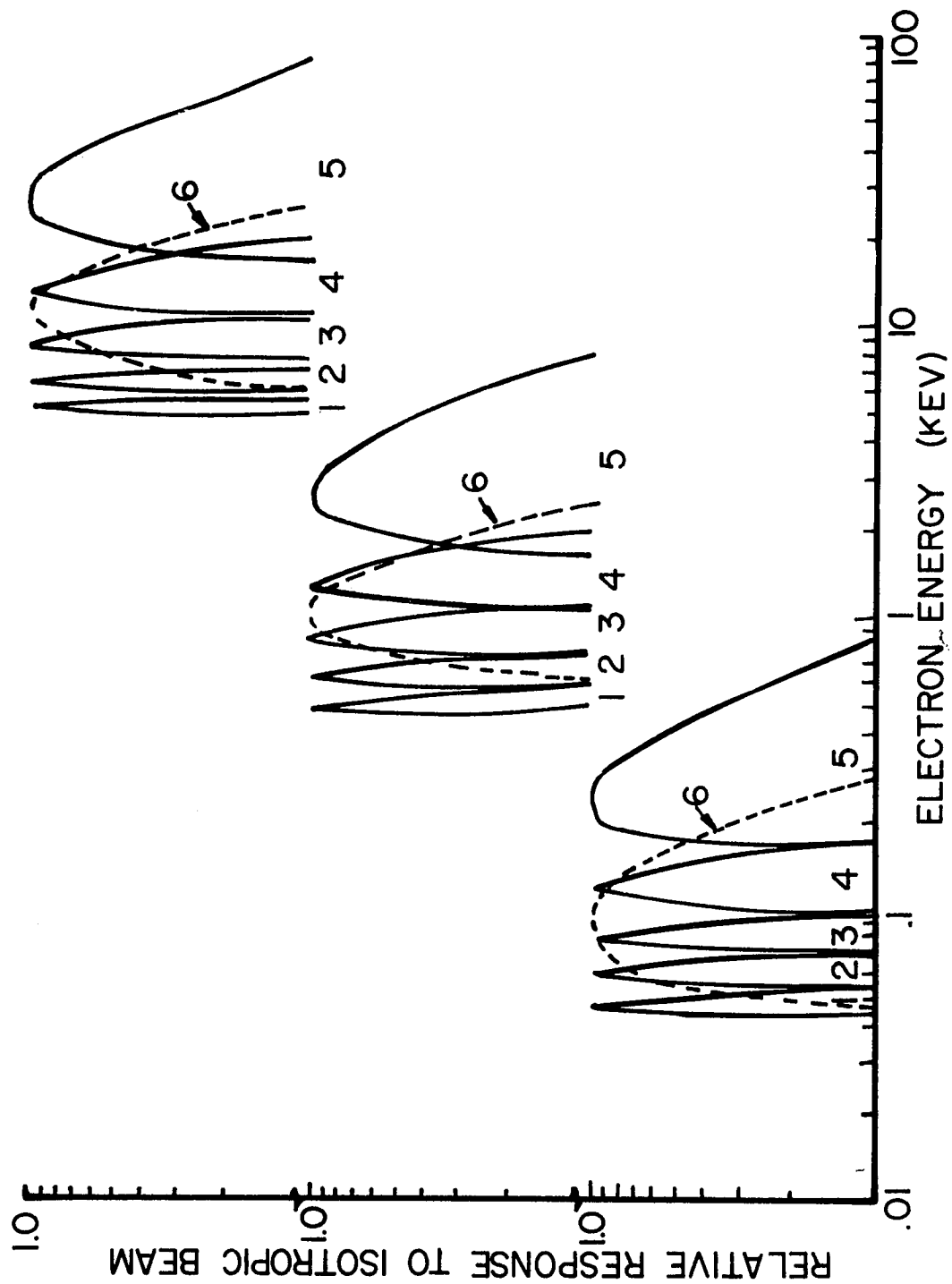


FIGURE 21

SPECS GEOMETRIC FACTORS

ELECTRONS:

<u>Channel</u>	<u>Plate Voltage</u>	<u>Geometric Factor (cm<sup>2</sup> ster ev)</u>
4	35 V	$8.67 \times 10^{-4}$
5	35 V	$1.52 \times 10^{-2}$
6	35 V	$7.15 \times 10^{-3}$
4	350 V	$8.06 \times 10^{-3}$
5	350 V	$2.46 \times 10^{-2}$
6	350 V	$4.75 \times 10^{-1}$
4	3500 V	$2.39 \times 10^{-2}$
5	3500 V	$1.88 \times 10^{-1}$
6	3500 V	$1.25 \times 10^0$

PROTONS:

<u>Channel</u>	<u>Plate Voltage</u>	<u>Geometric Factor (cm<sup>2</sup> ster ev)</u>
4	35 V	$6.02 \times 10^{-4}$
5	35 V	$1.22 \times 10^{-2}$
4	350 V	$1.78 \times 10^{-2}$
5	350 V	$1.17 \times 10^{-1}$
4	3500 V	$1.26 \times 10^{-1}$
5	3500 V	$7.45 \times 10^{-1}$

Other channels not used.

**FIGURE 22**

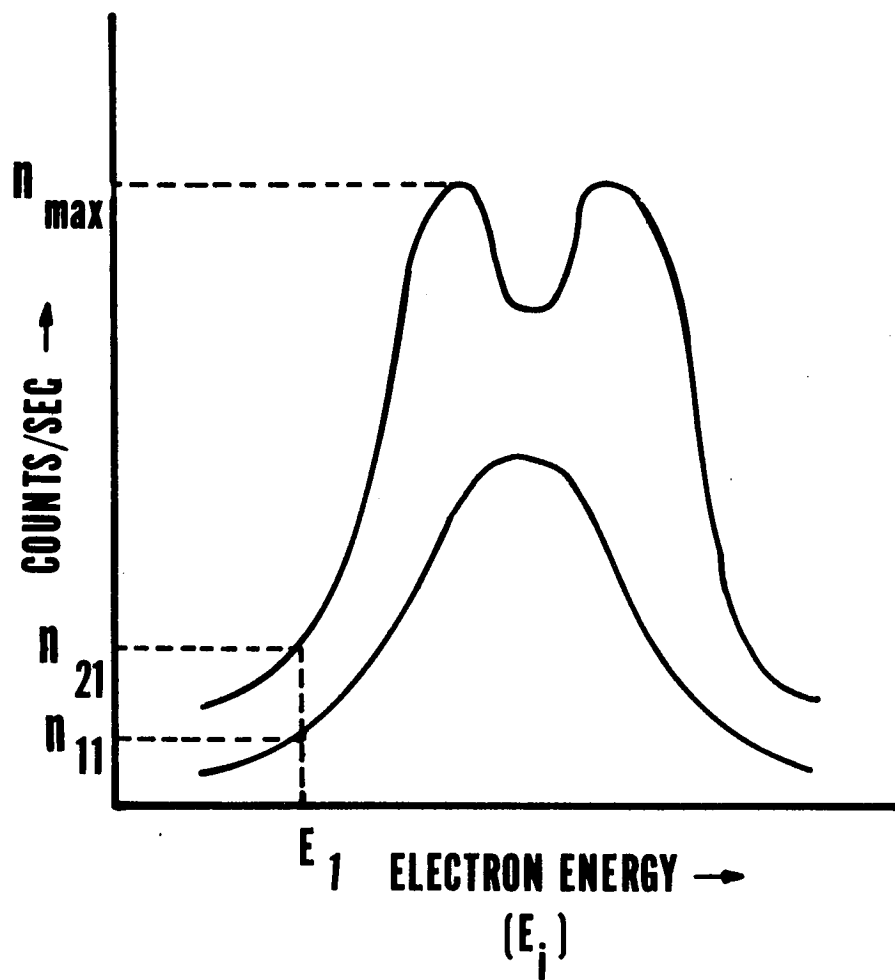


FIGURE 23

TRUE vs. APPARENT COUNT RATE  
CHANNEL 1

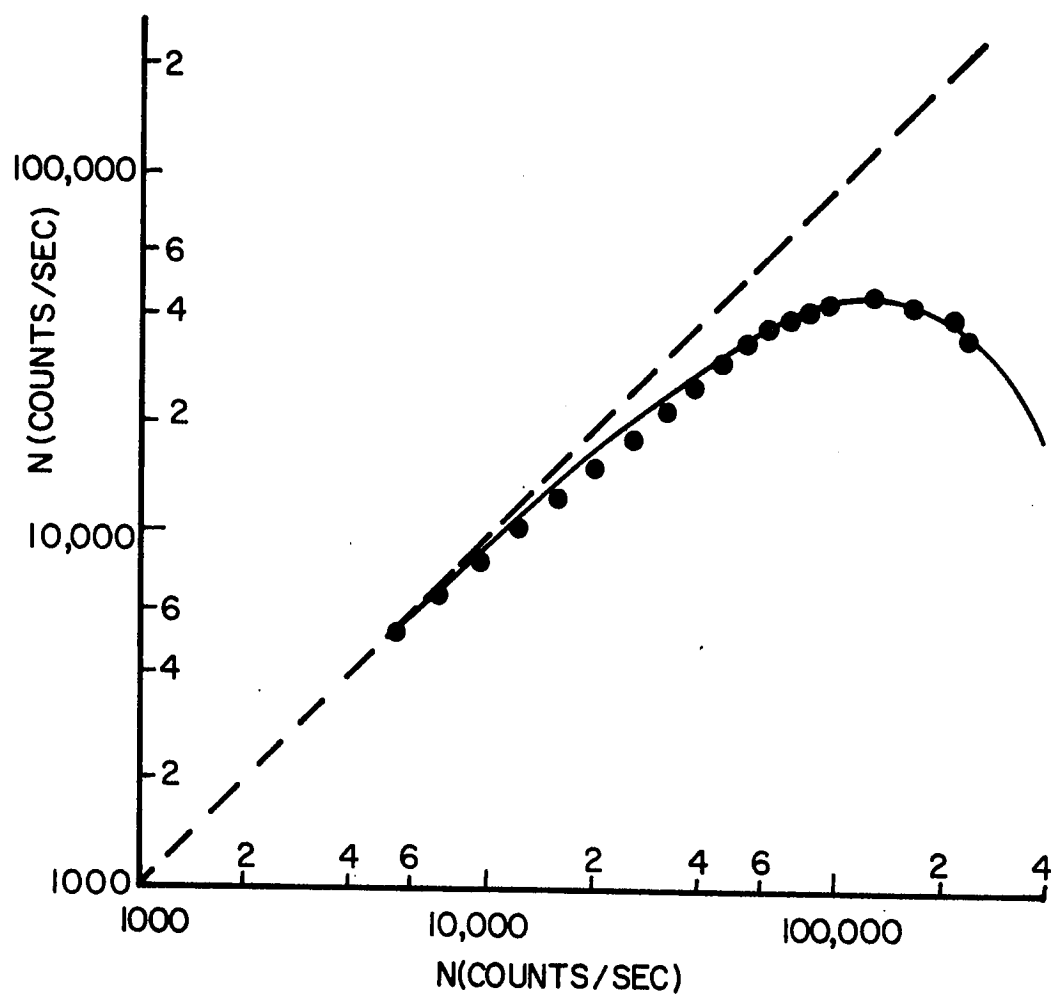


FIGURE 24



TRUE (N) VS. APPARENT (n) COUNT RATE

Prelaunch at  $10^{-6}$  mm Hg.

<u>Channel</u>	<u>Dead Time</u>	<u>n(N)</u>
1	$7.96 \times 10^{-6}$ sec	$n = Ne^{-N(7.96 \times 10^{-6})}$
2	$9.31 \times 10^{-6}$ sec	$n = Ne^{-N(9.31 \times 10^{-6})}$
3	$1.52 \times 10^{-5}$ sec	$n = Ne^{-N(1.52 \times 10^{-5})}$
4	$1.48 \times 10^{-6}$ sec	$n = Ne^{-N(1.48 \times 10^{-6})}$
5	$1.61 \times 10^{-6}$ sec	$n = Ne^{-N(1.61 \times 10^{-6})}$
6	$5.46 \times 10^{-6}$ sec	$n = Ne^{-N(5.46 \times 10^{-6})}$

FIGURE 25

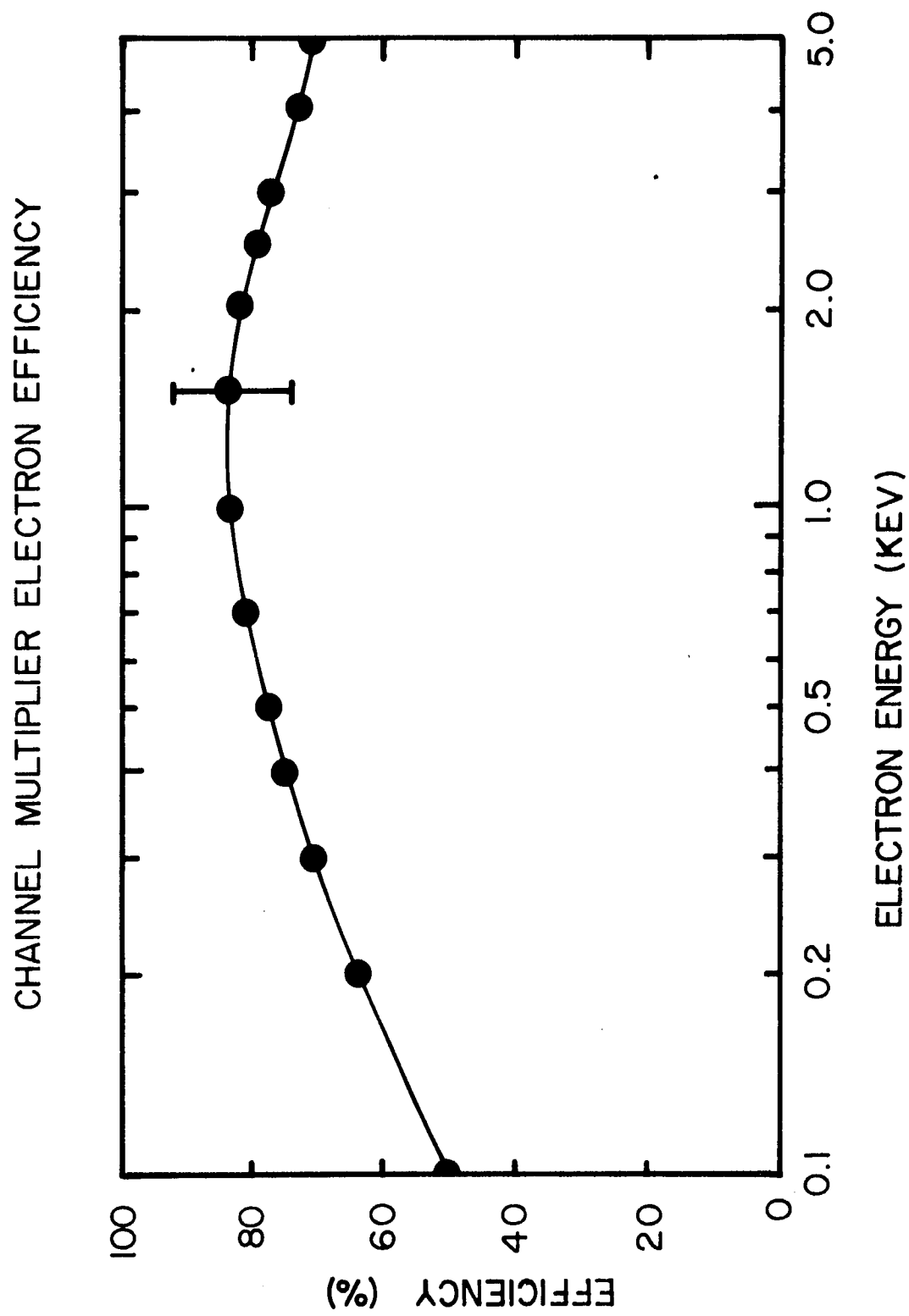


FIGURE 26

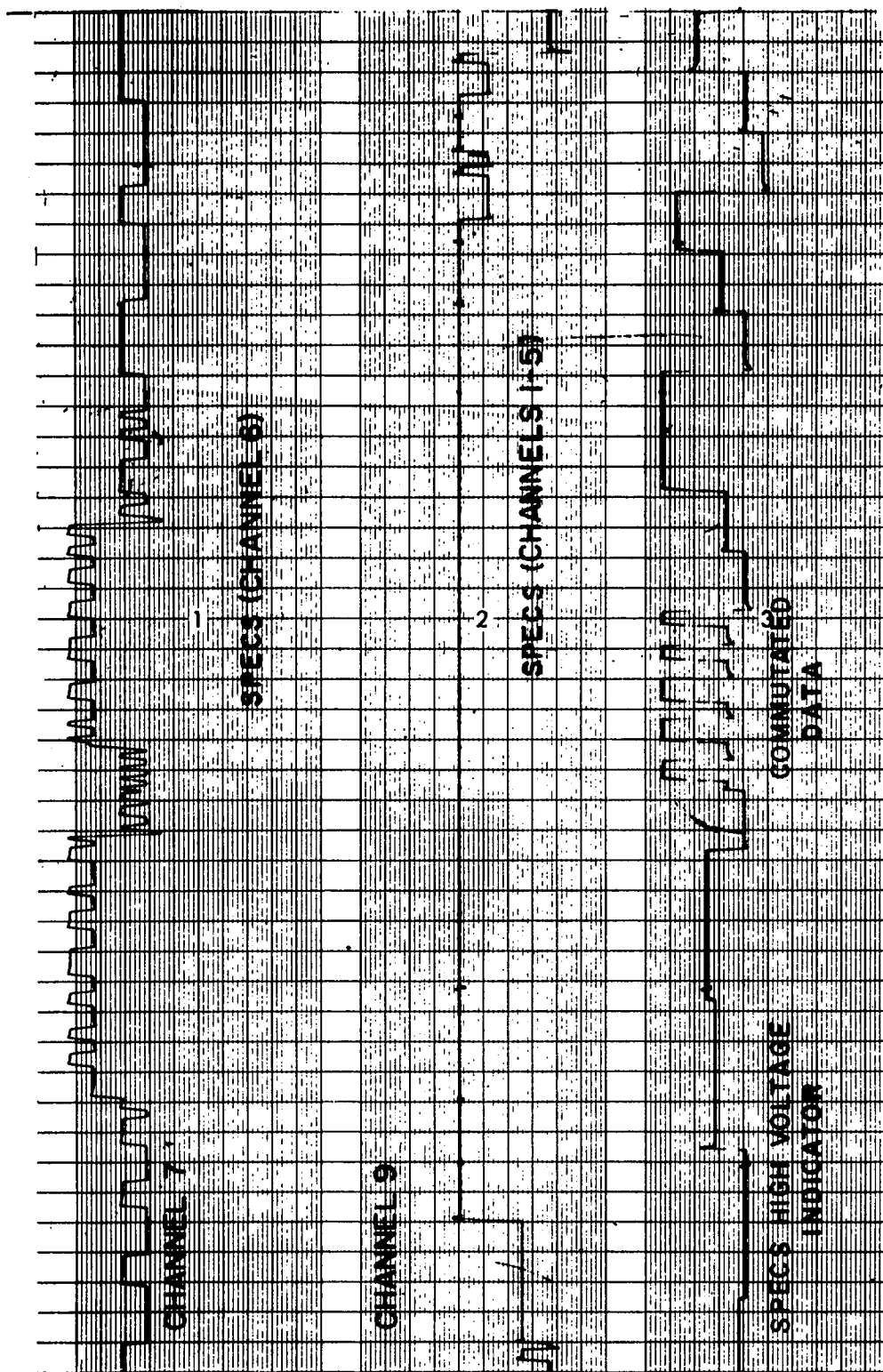


FIGURE 27

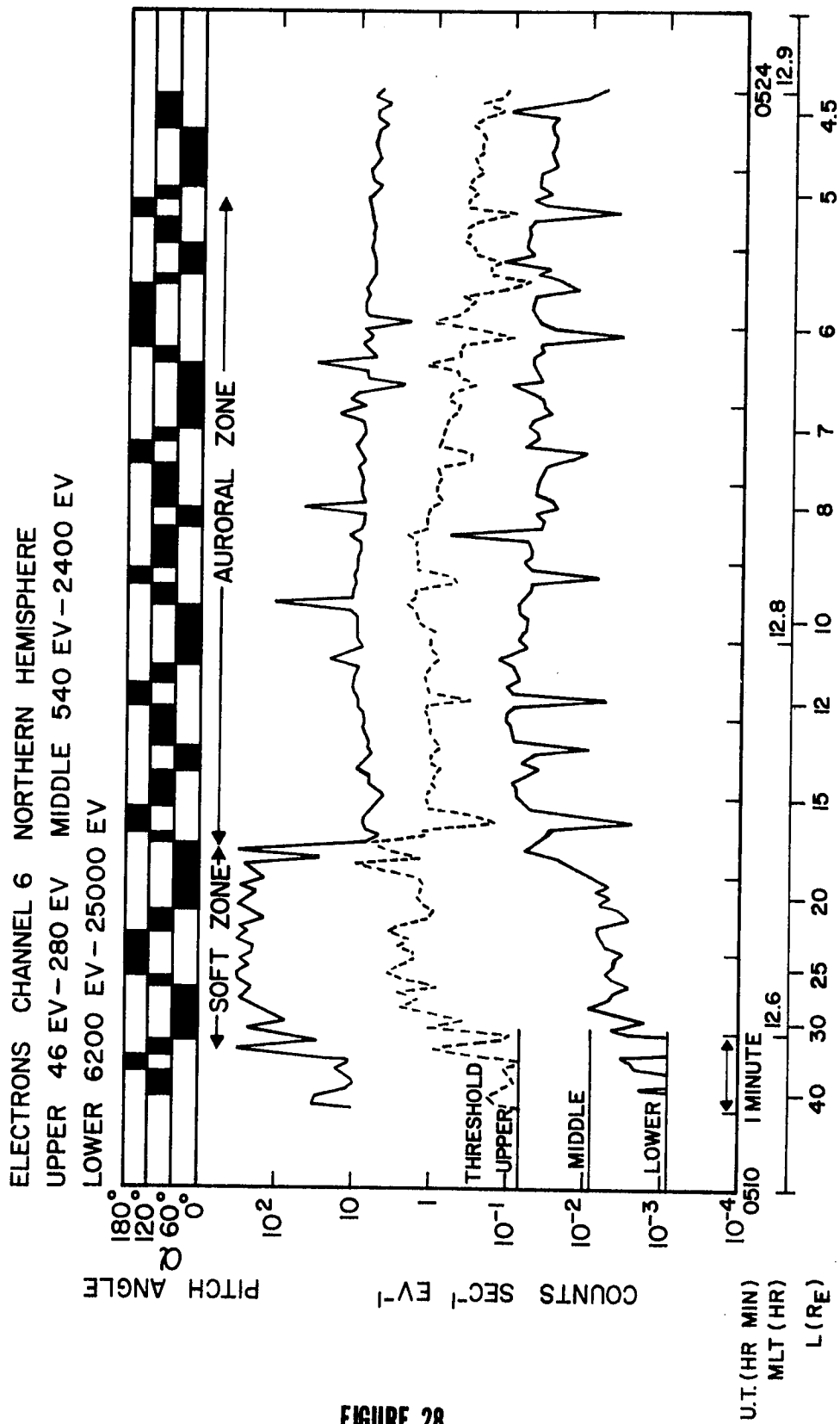


FIGURE 28

ELECTRONS CHANNEL 6 SOUTHERN HEMISPHERE  
 UPPER 46 EV - 280 EV MIDDLE 540 EV - 2400 EV  
 LOWER 6200 EV - 25000 EV

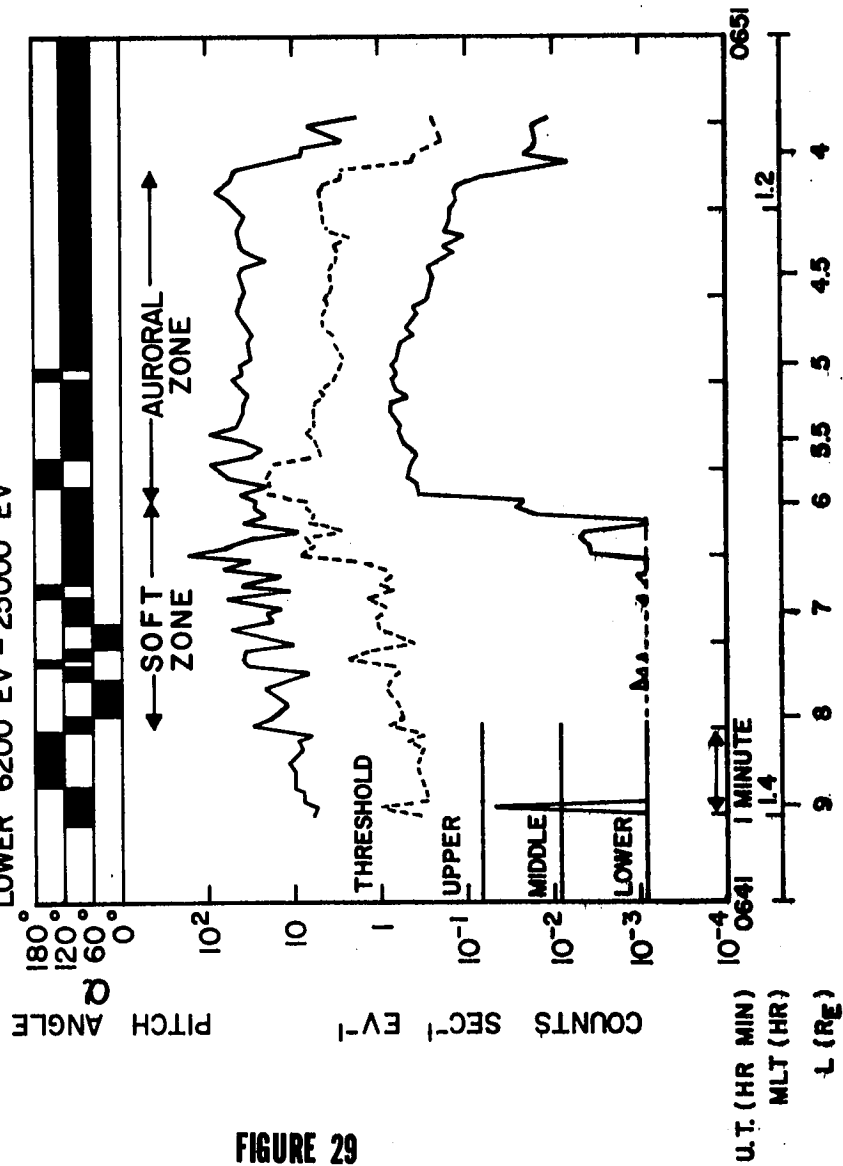


FIGURE 29

ELECTRONS CHANNEL 6 NORTHERN HEMISPHERE  
 UPPER 46 EV - 280 EV MIDDLE 540 EV - 2400 EV  
 LOWER 6200 EV - 25000 EV

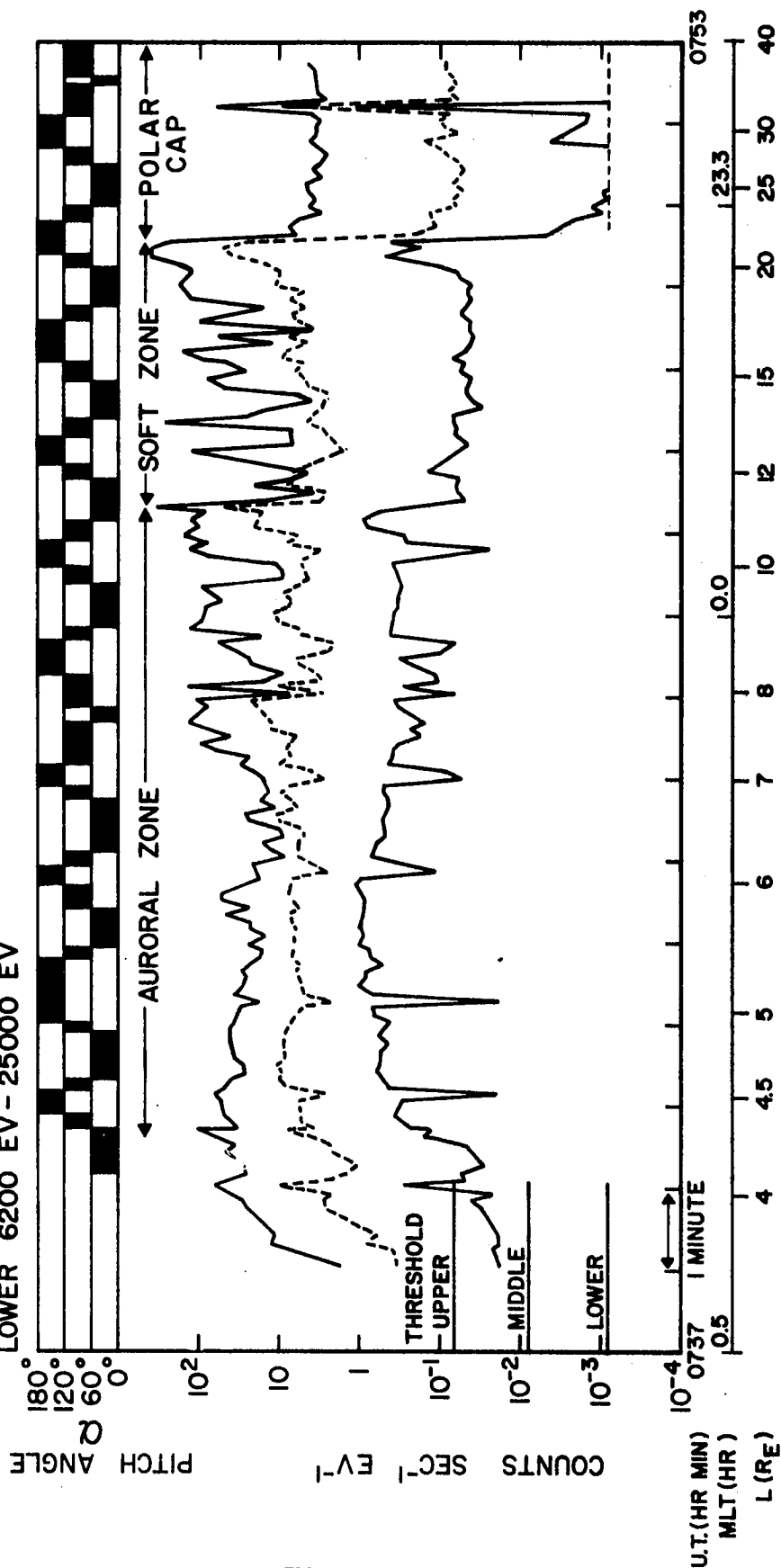


FIGURE 30

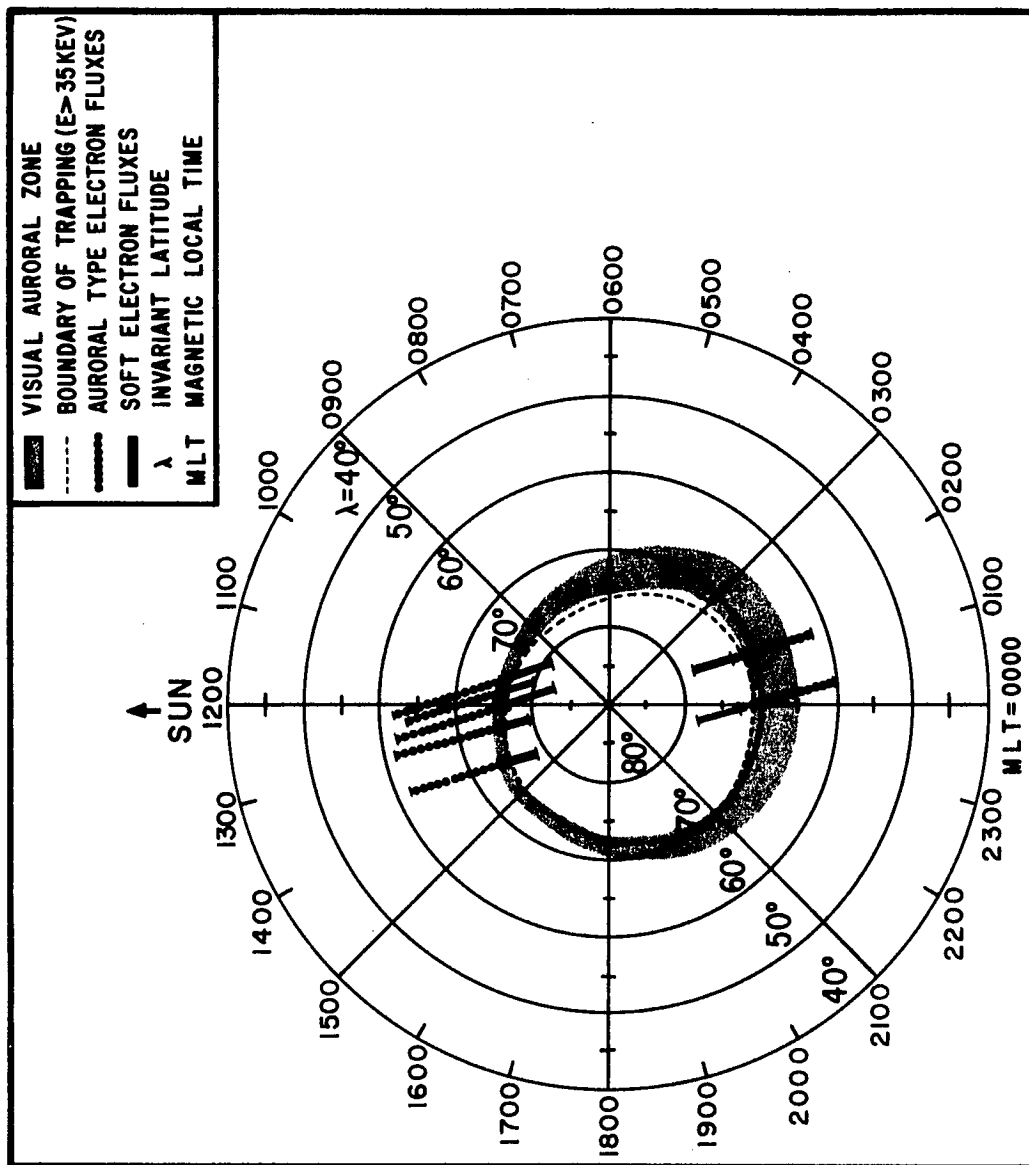


FIGURE 31

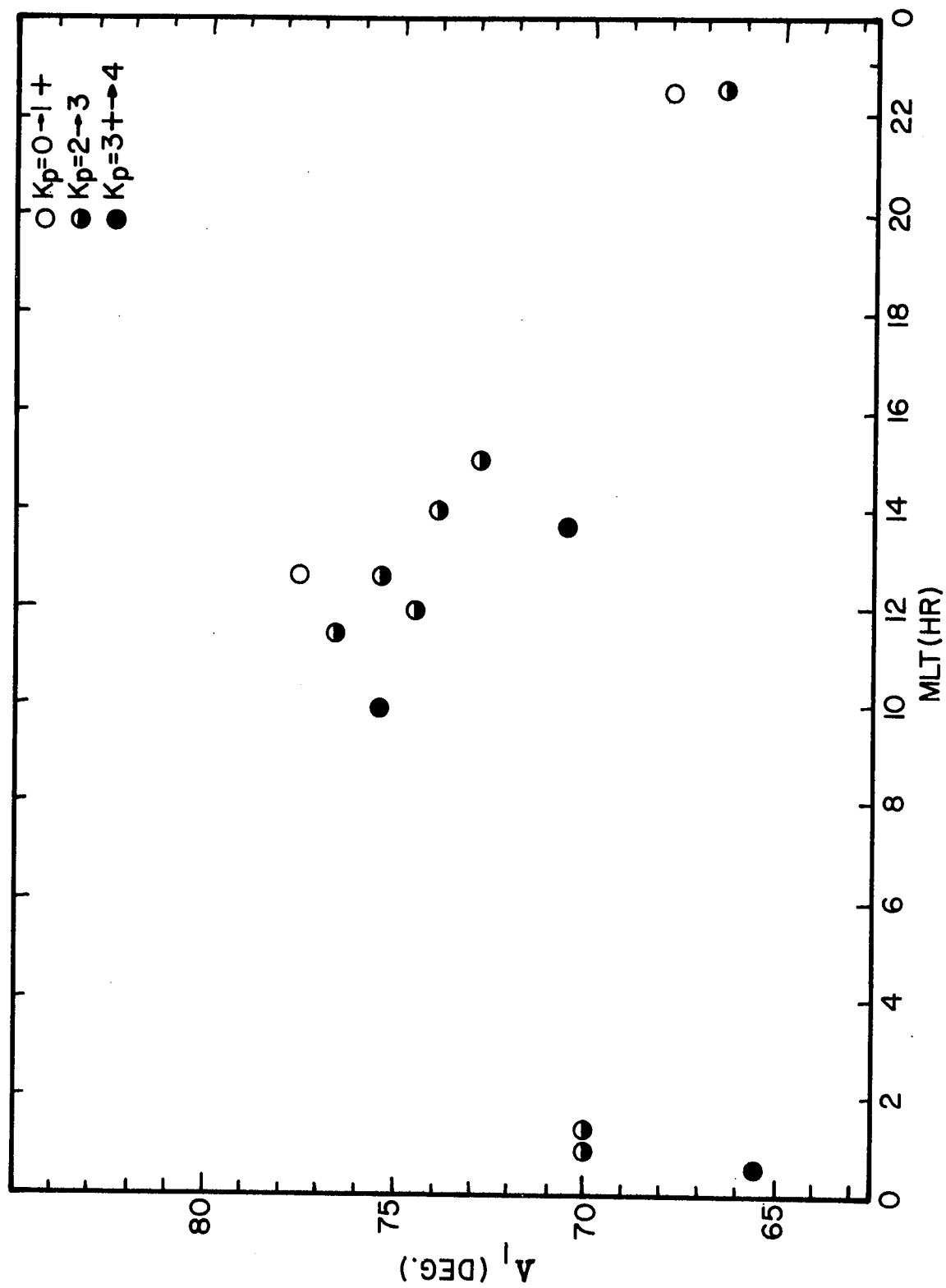


FIGURE 32



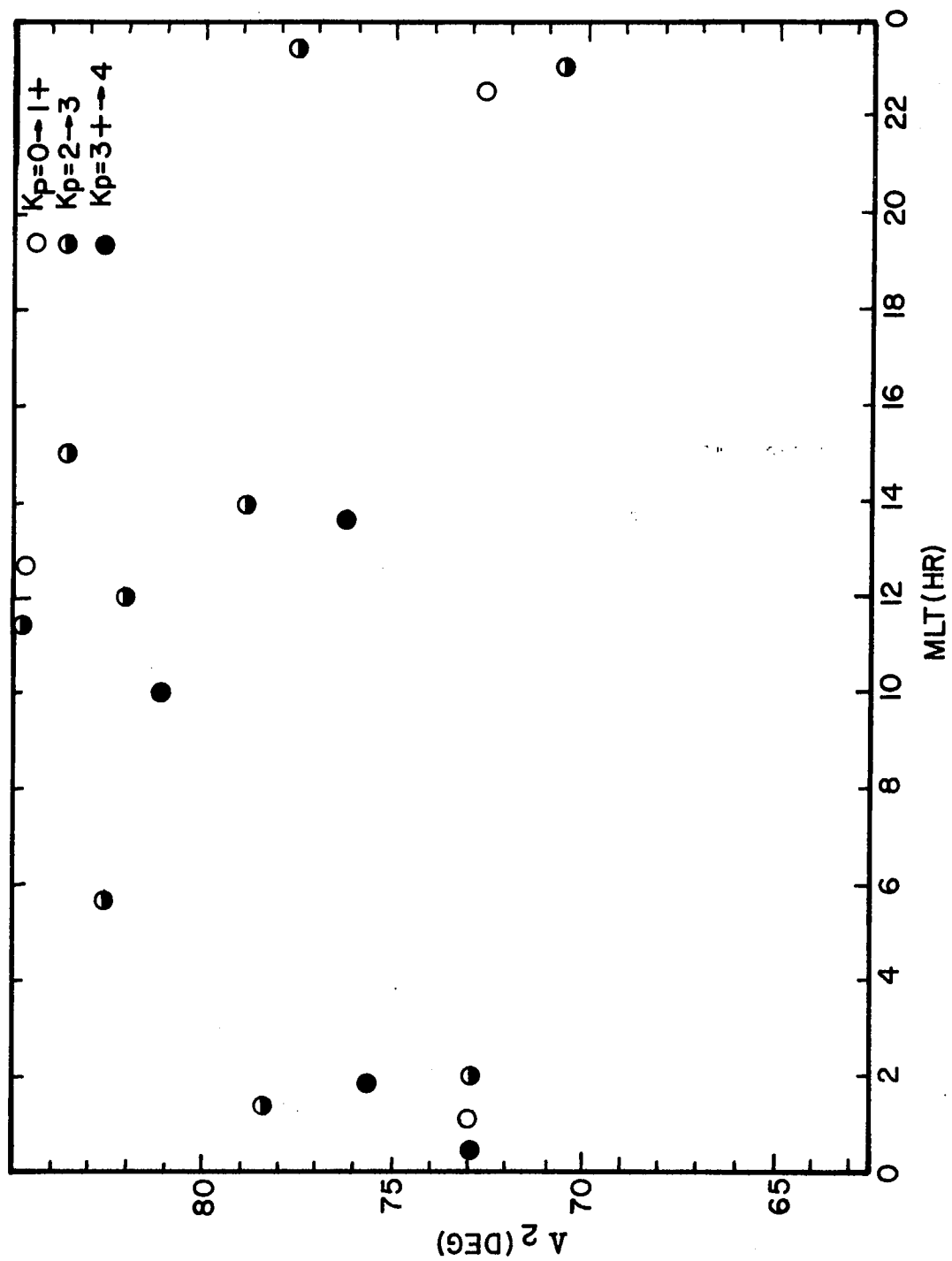


FIGURE 33

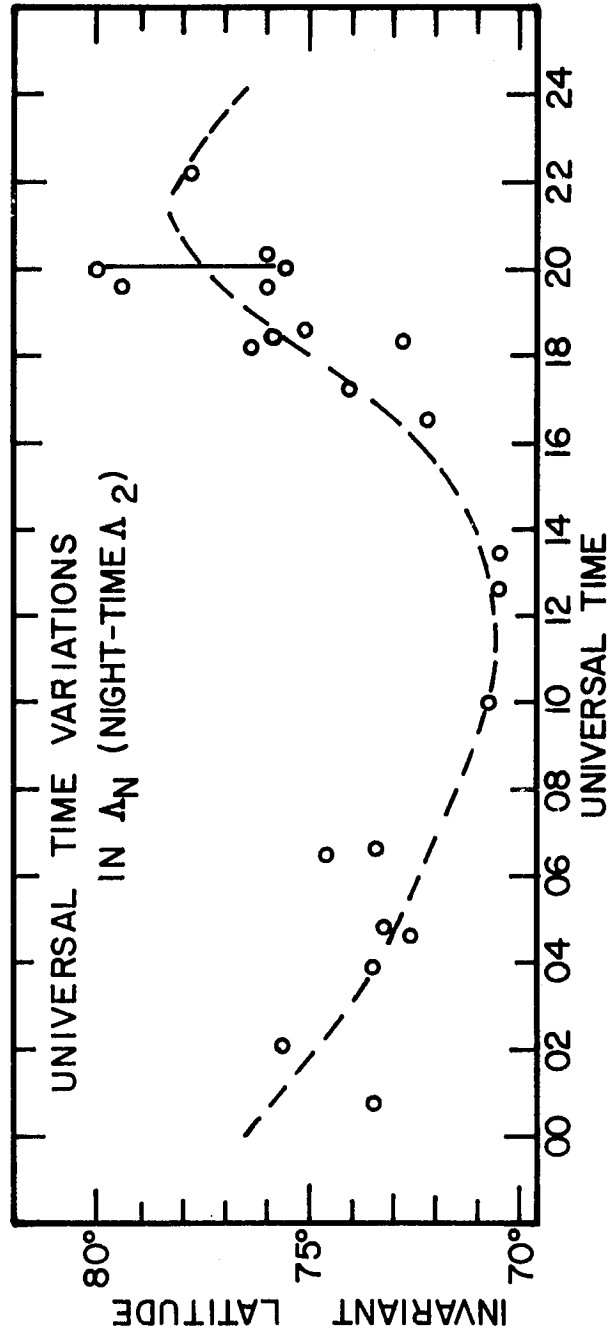


FIGURE 34

# PRECIPITATED ELECTRONS

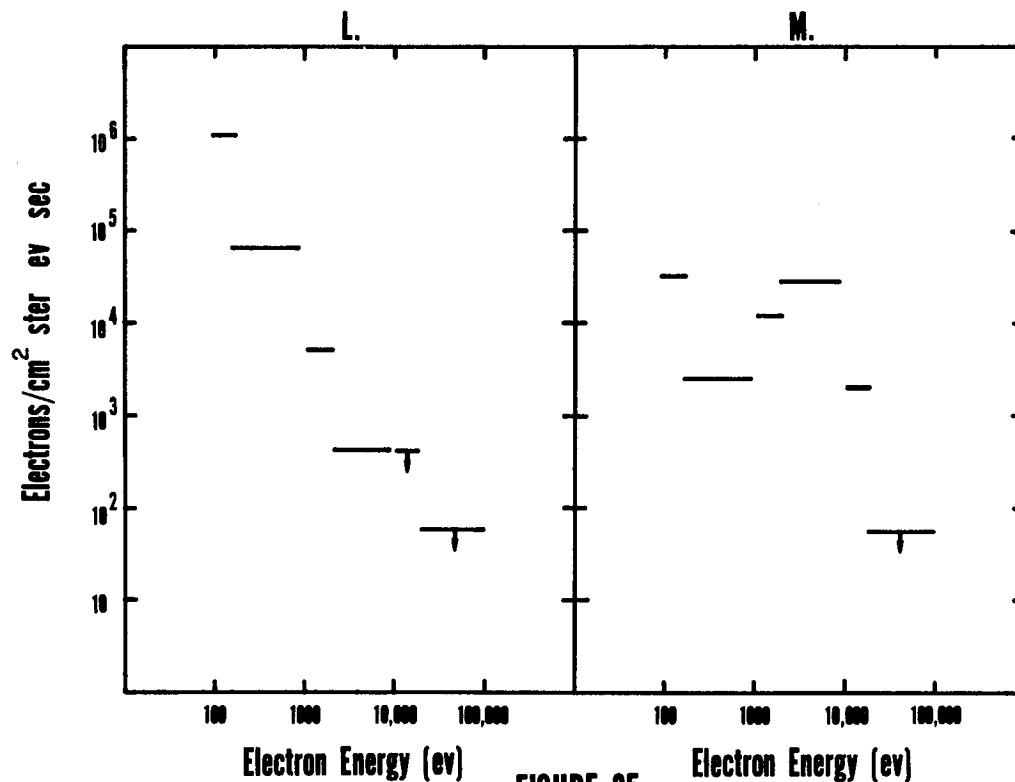
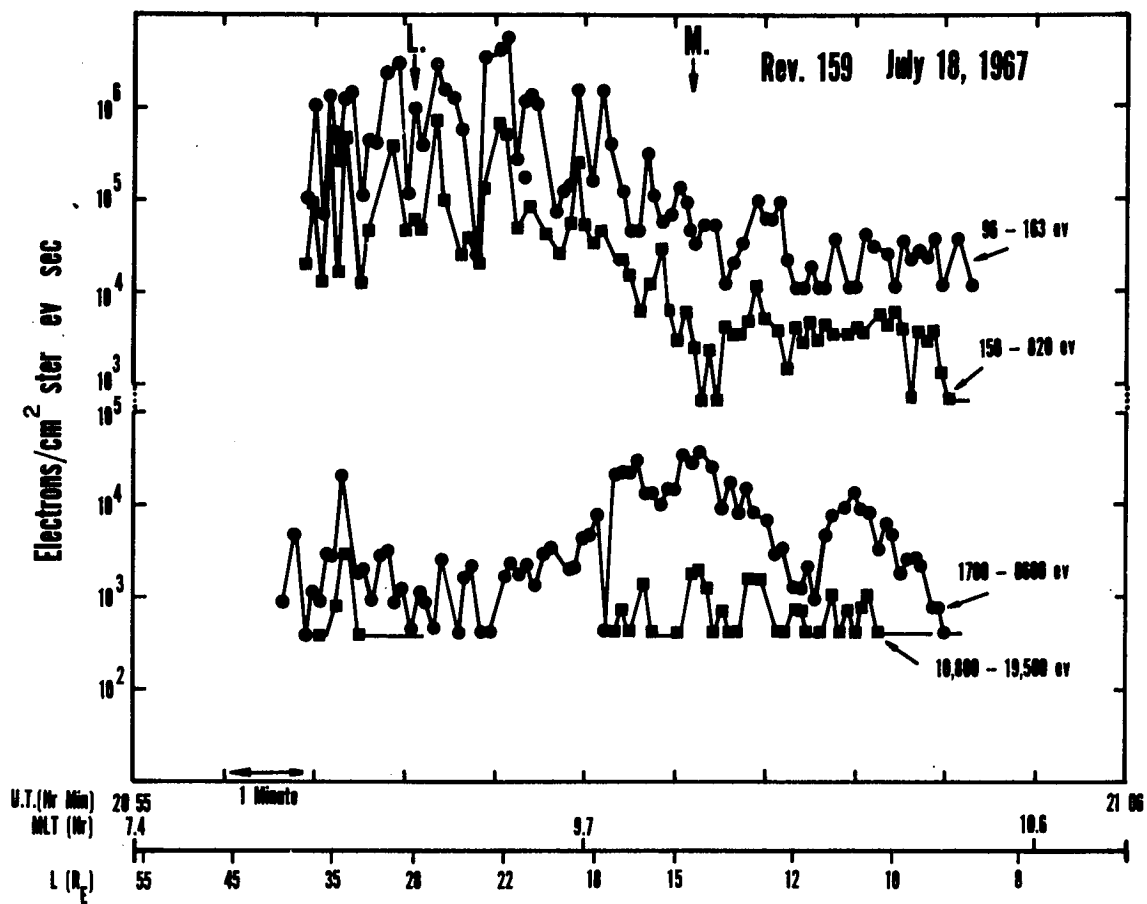
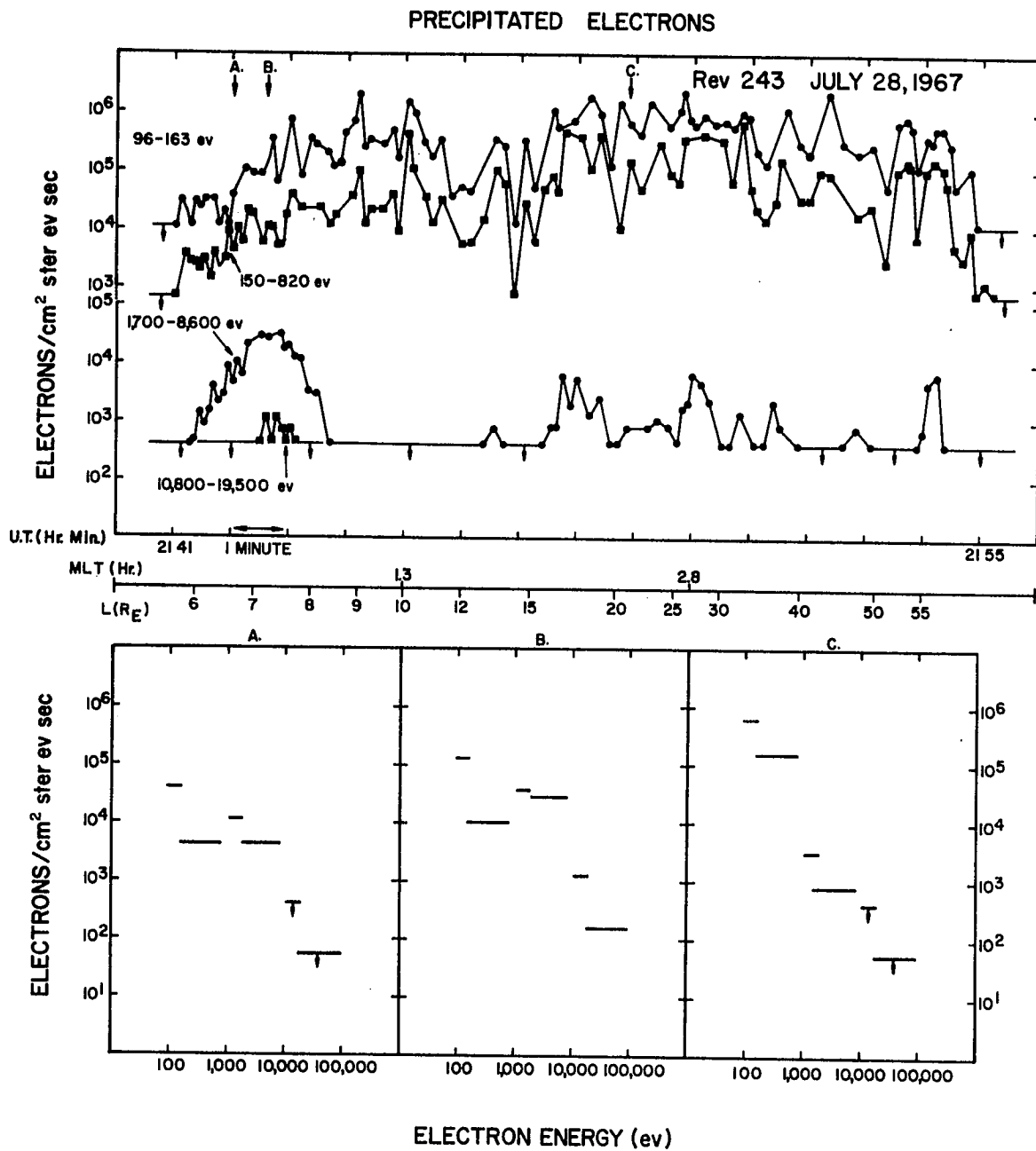
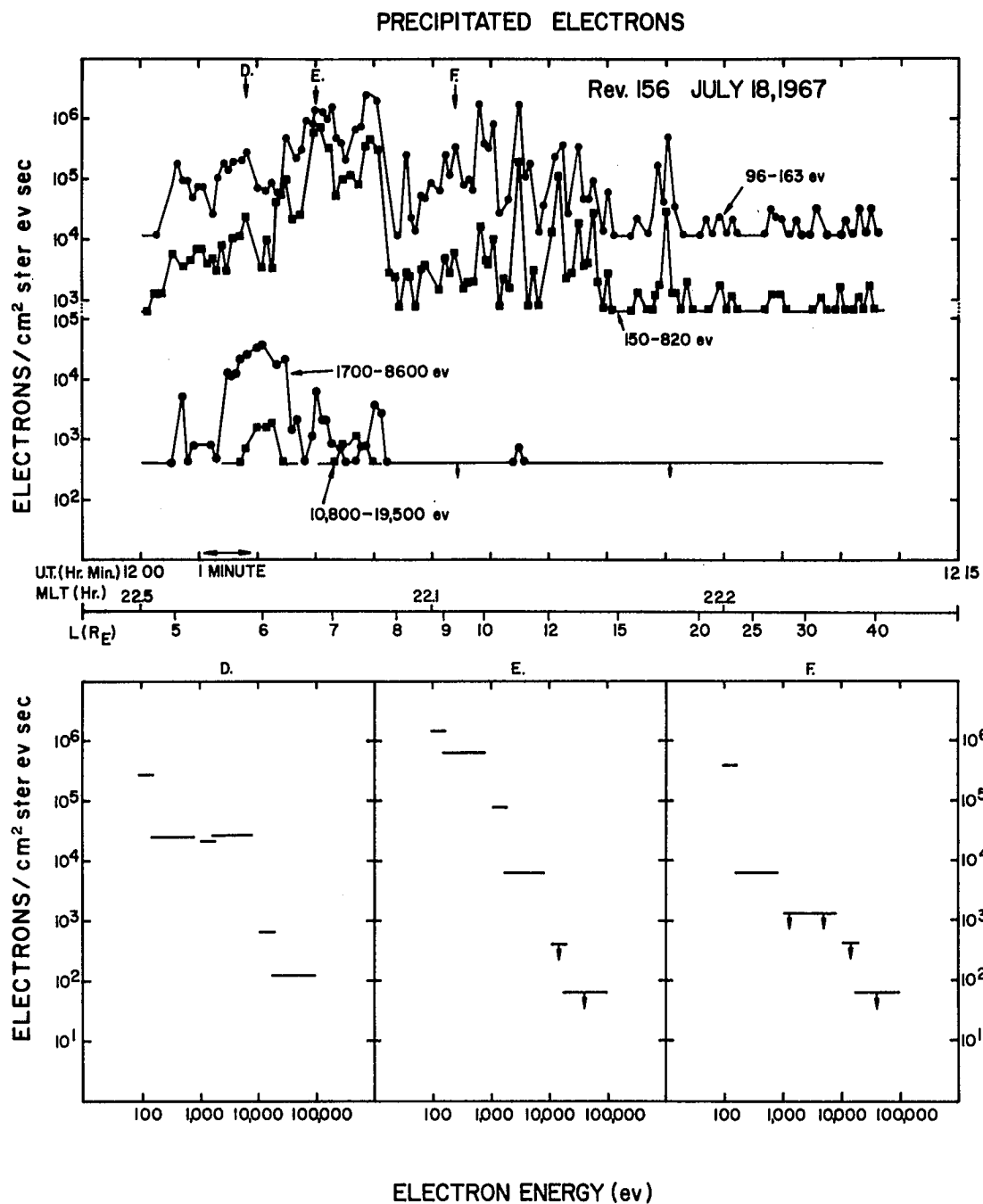


FIGURE 35



**FIGURE 36**



**FIGURE 37**

# PRECIPITATED ELECTRONS

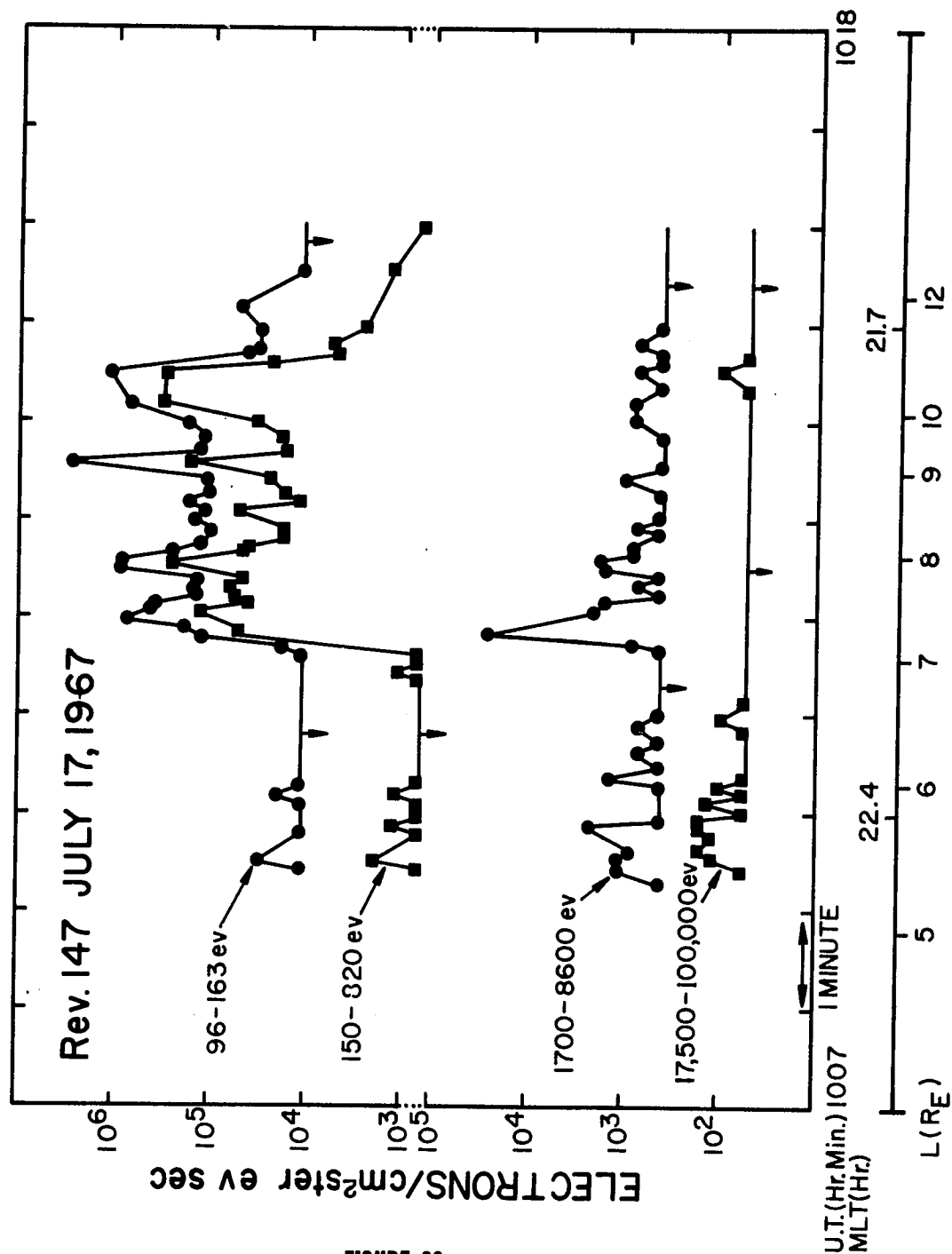


FIGURE 38

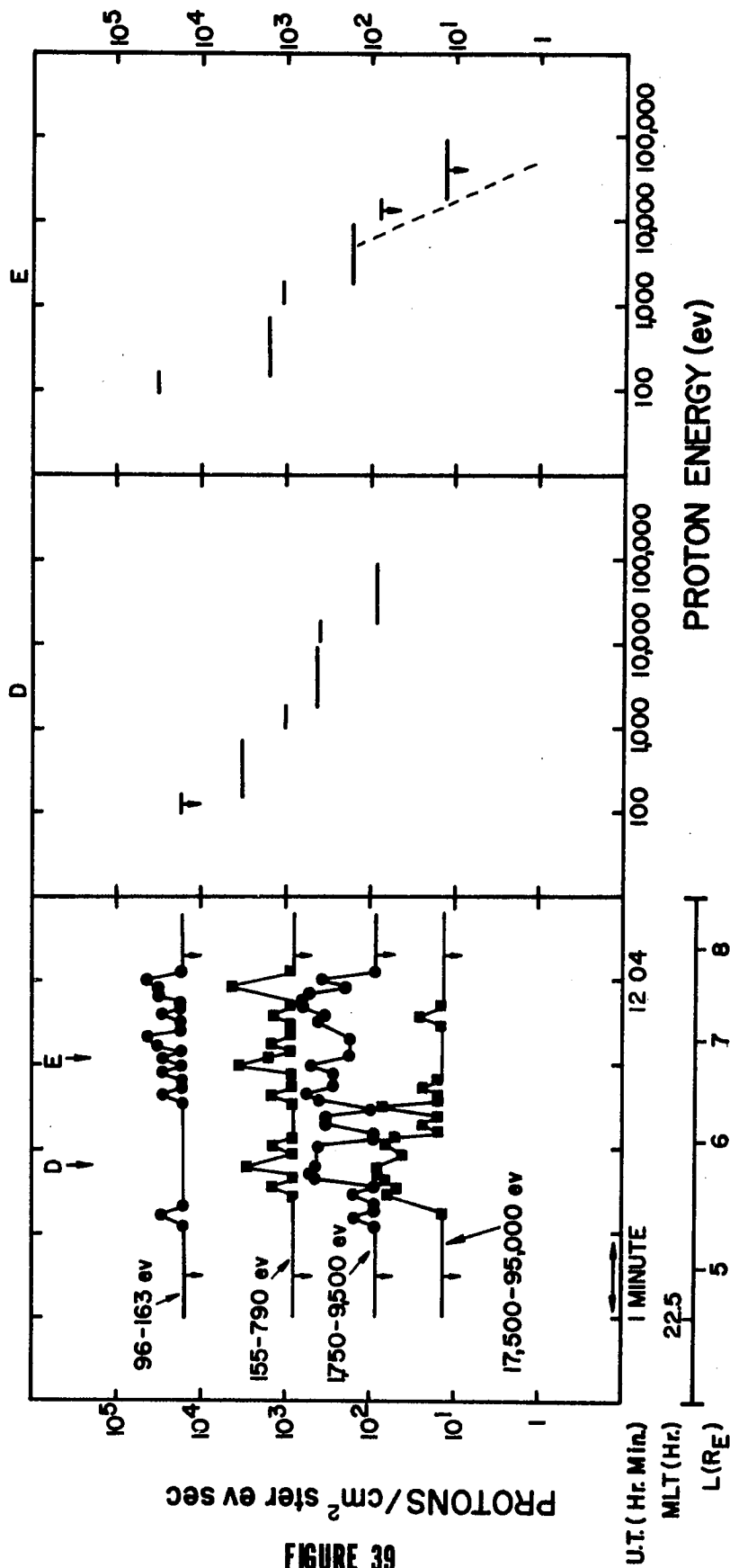


FIGURE 39

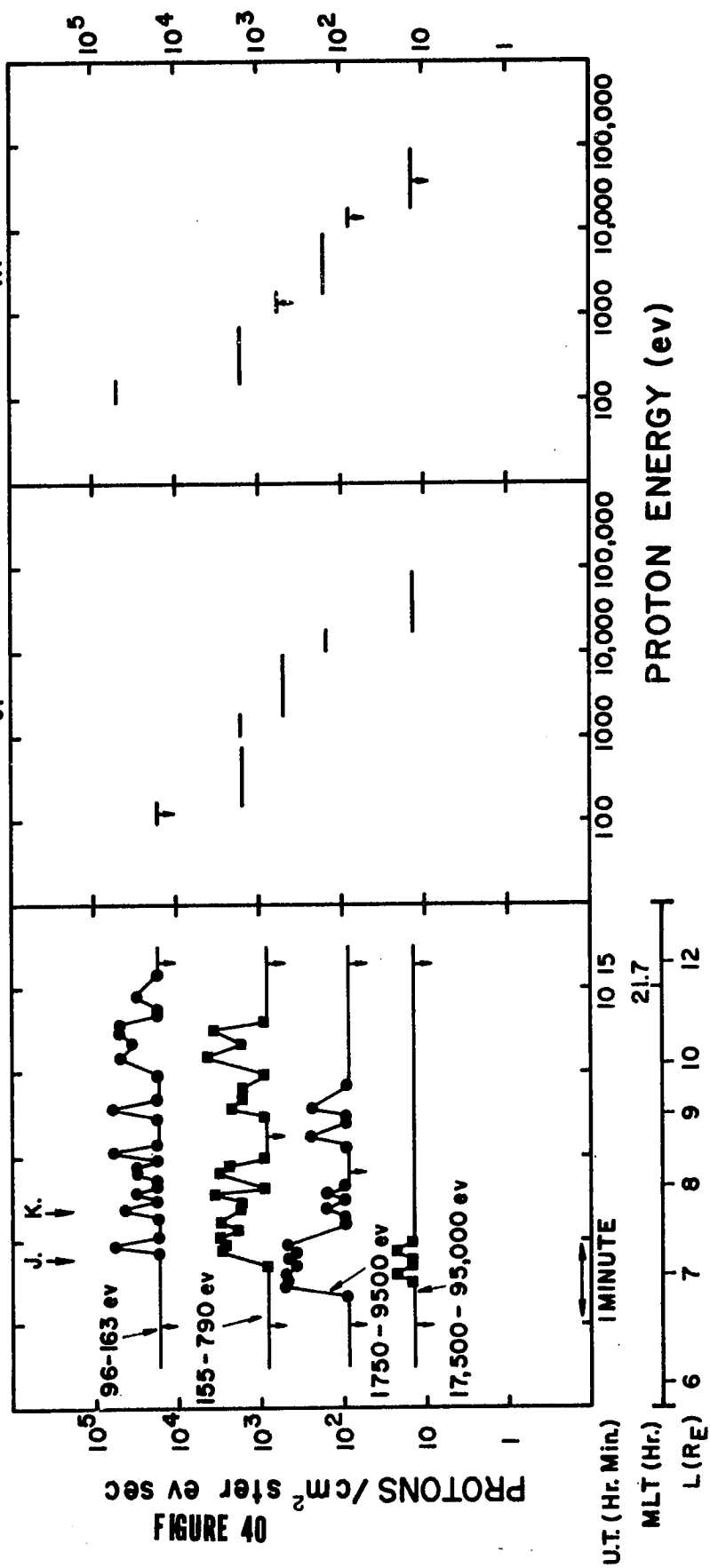
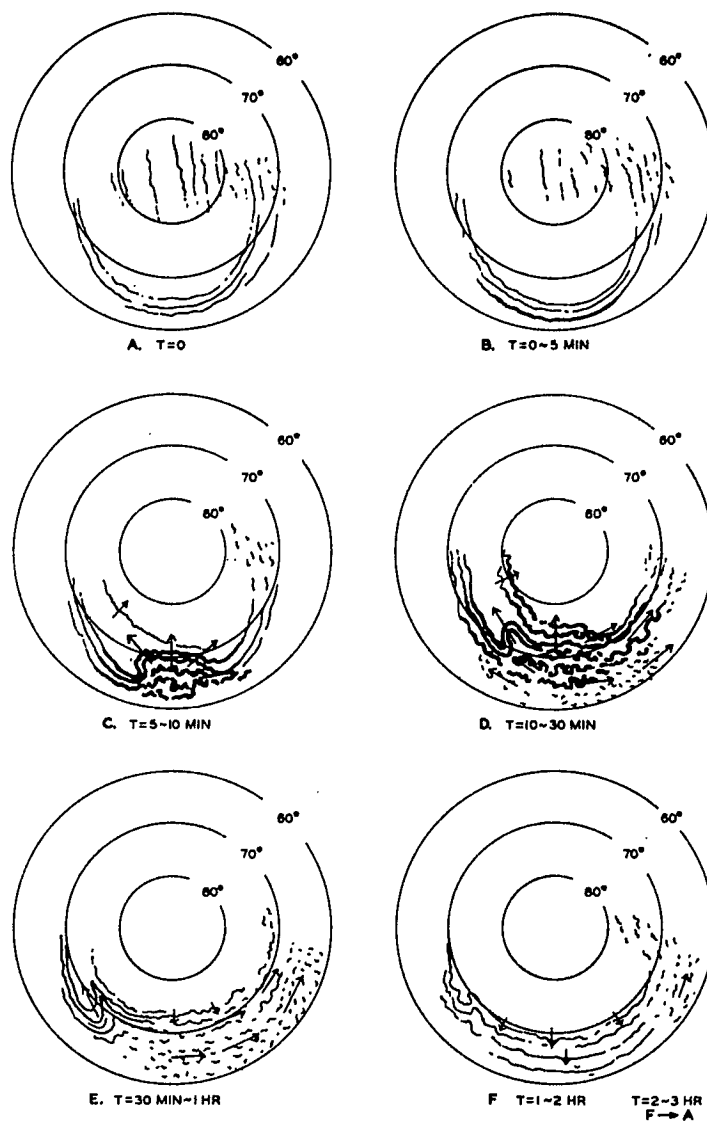
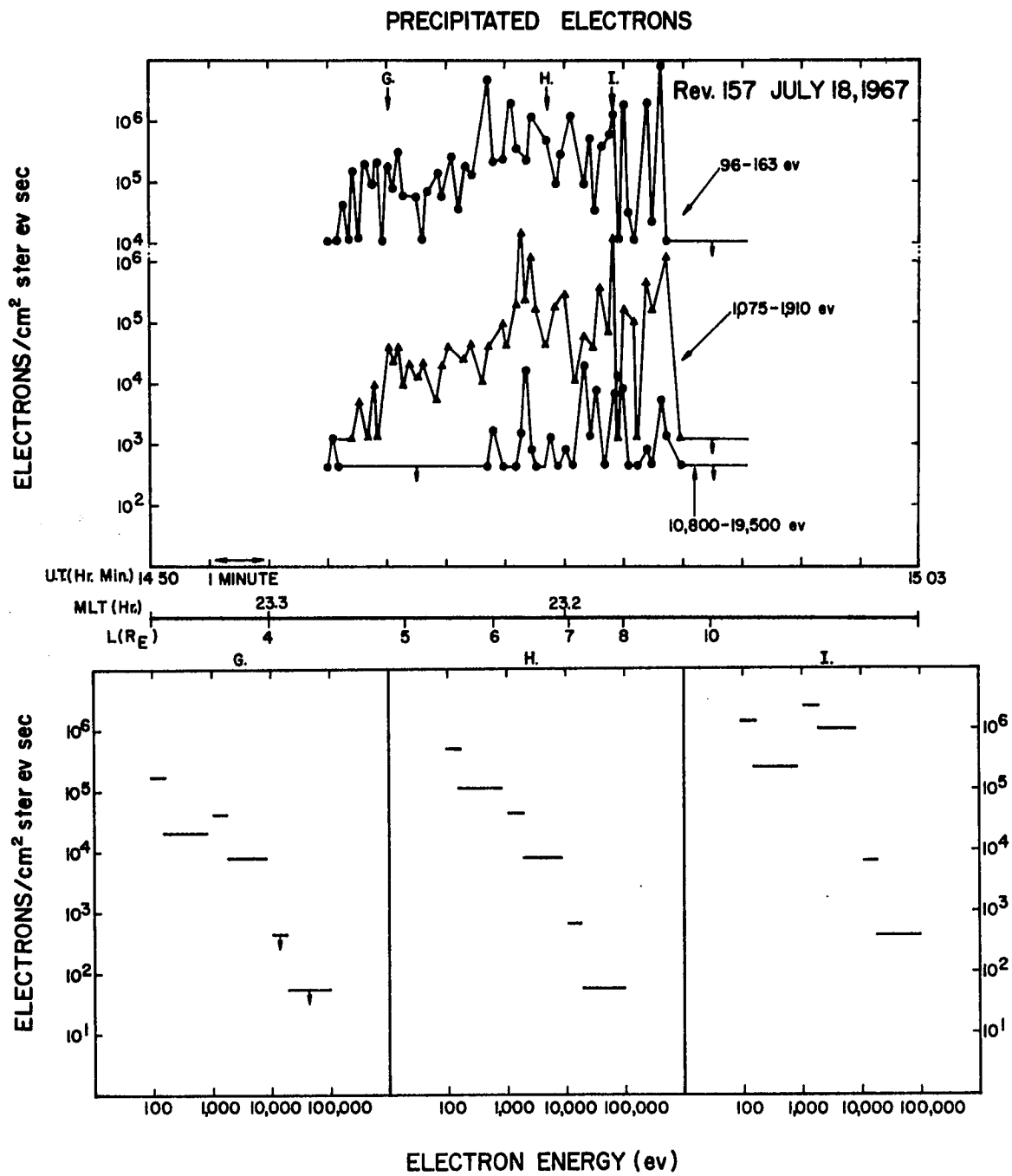


FIGURE 40





**FIGURE 41**



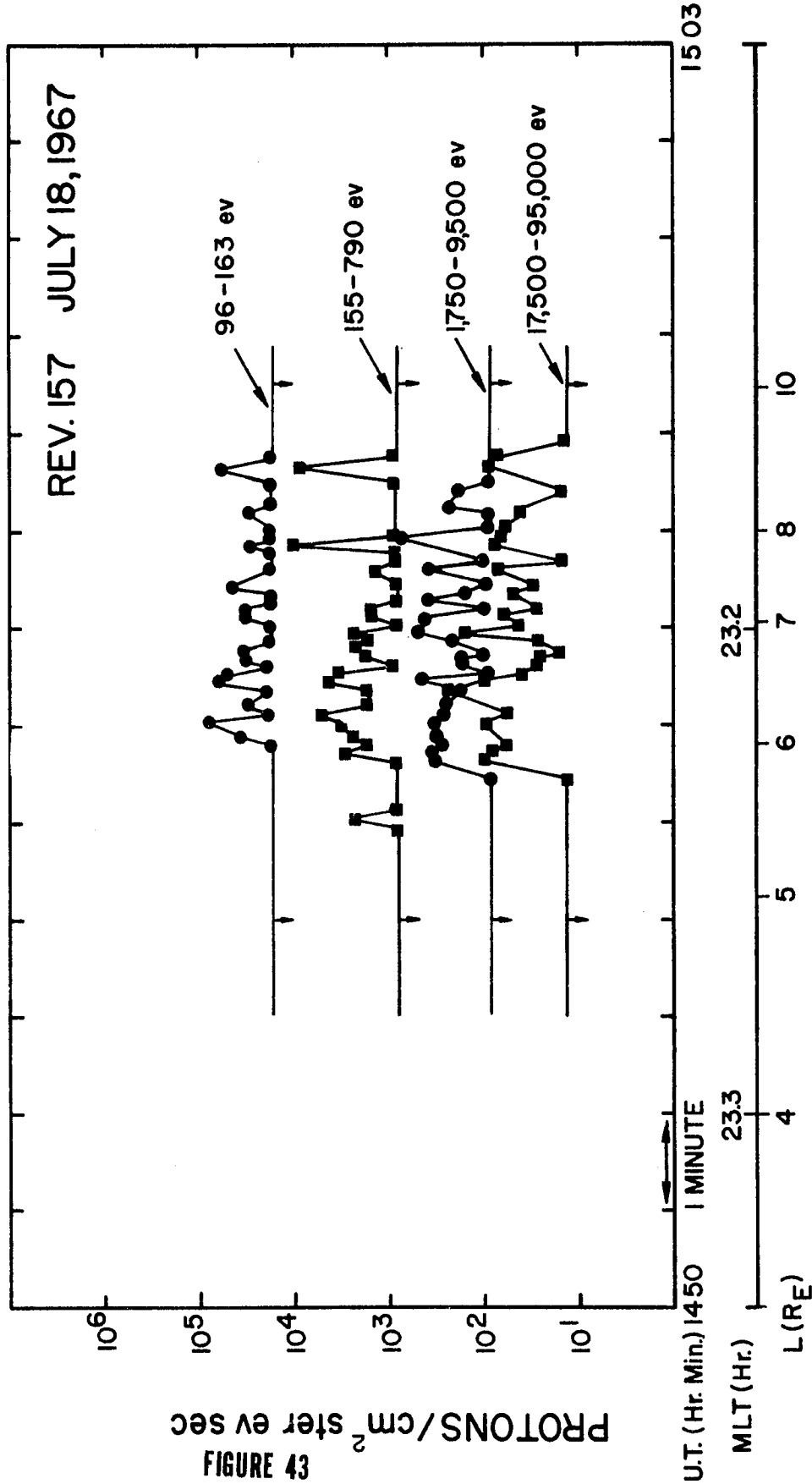
**FIGURE 42**

# PRECIPITATED PROTONS

REV. 157 JULY 18, 1967

FIGURE 43

PROTONS/cm<sup>2</sup> ster ev sec



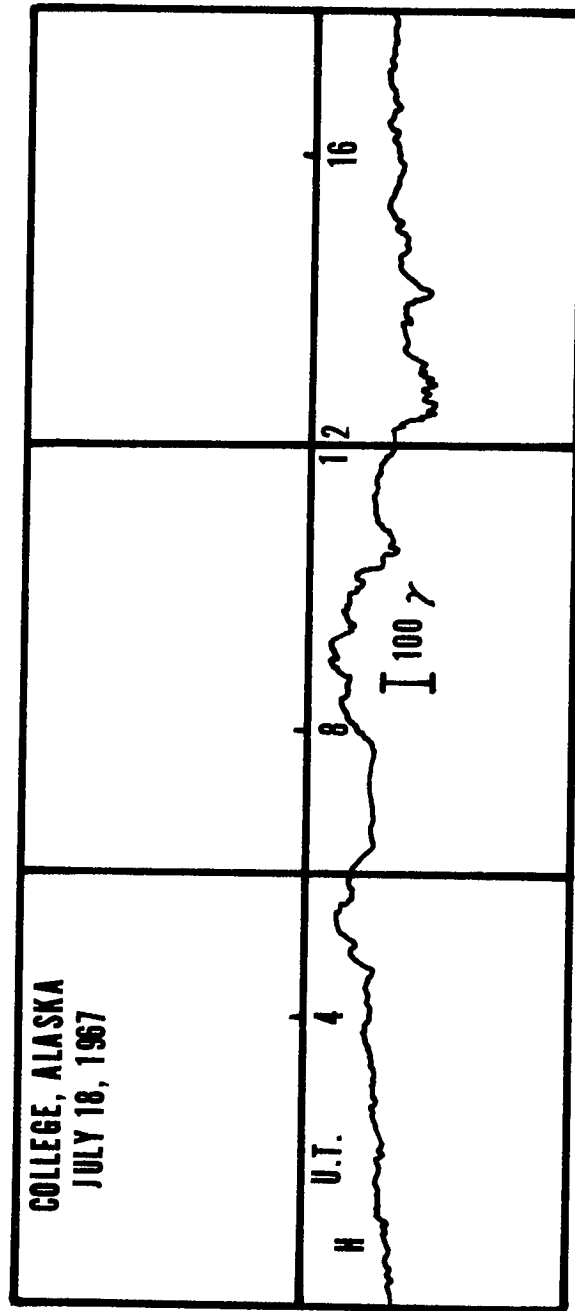


FIGURE 44

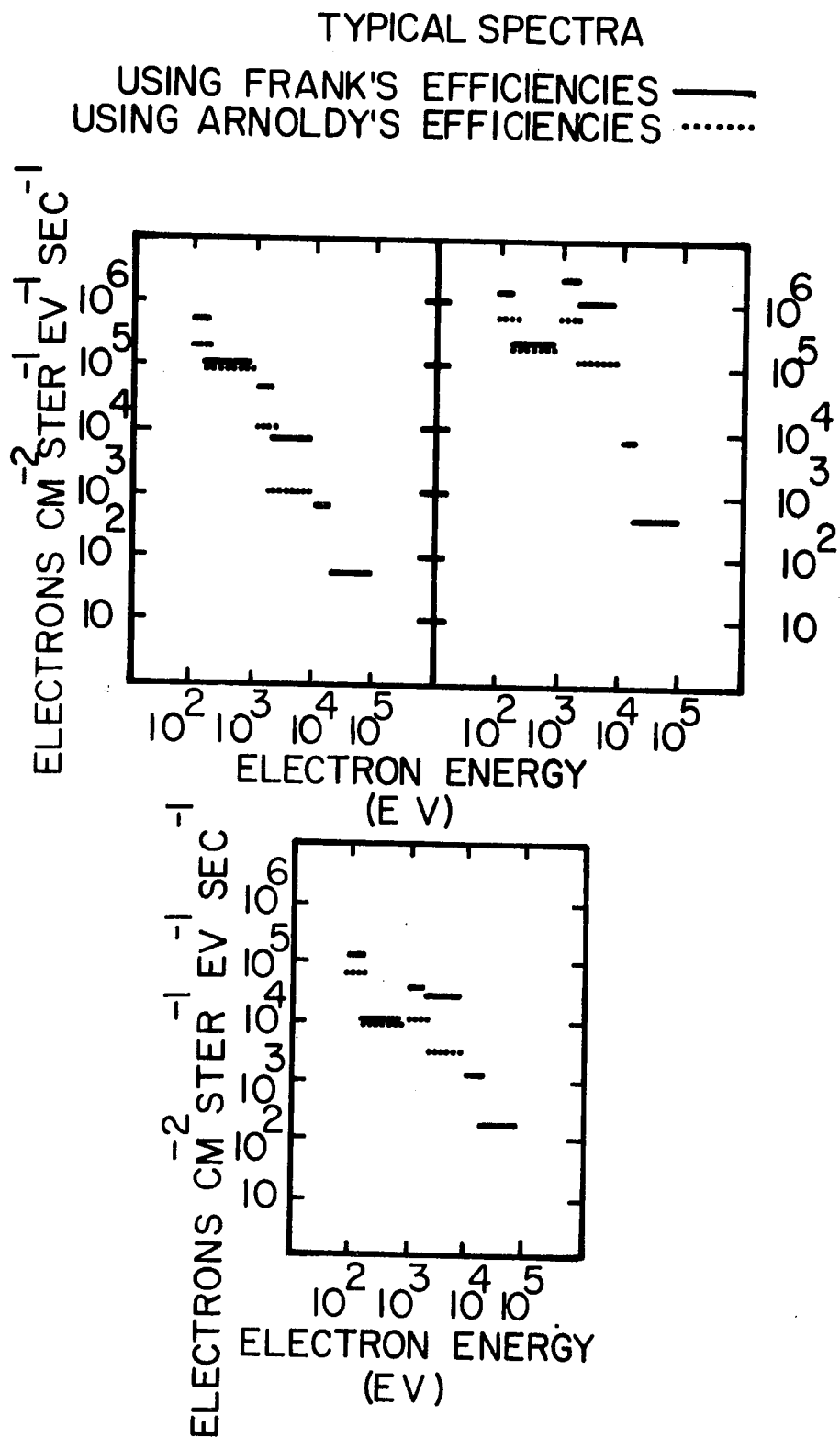


FIGURE 45

# TYPICAL ENERGY SPECTRA

LOCKHEED DAY SOFT ZONE ● LOCKHEED NIGHT PROTONS ▴  
 AURORA I DAY SOFT ZONE — AURORA I NIGHT PROTONS —

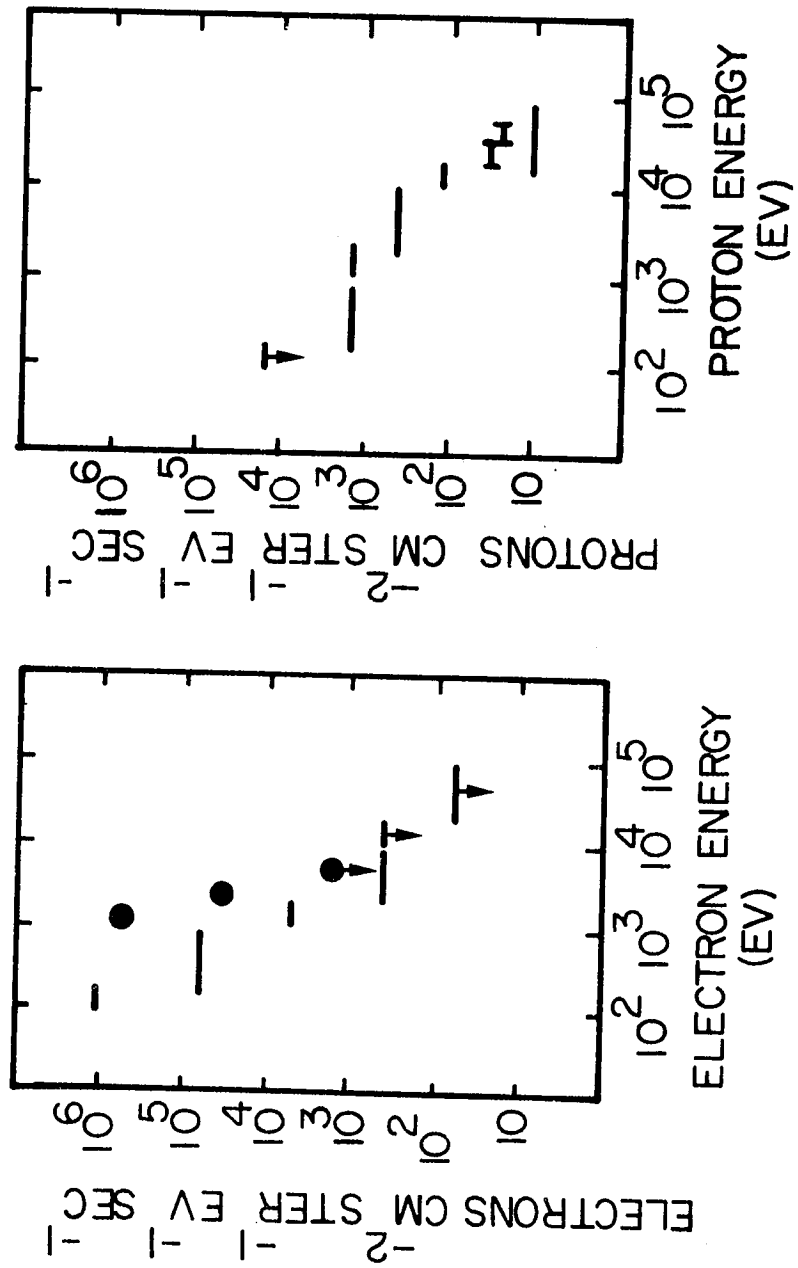


FIGURE 46

# ELECTRON SPECTRA DURING SUBSTORMS

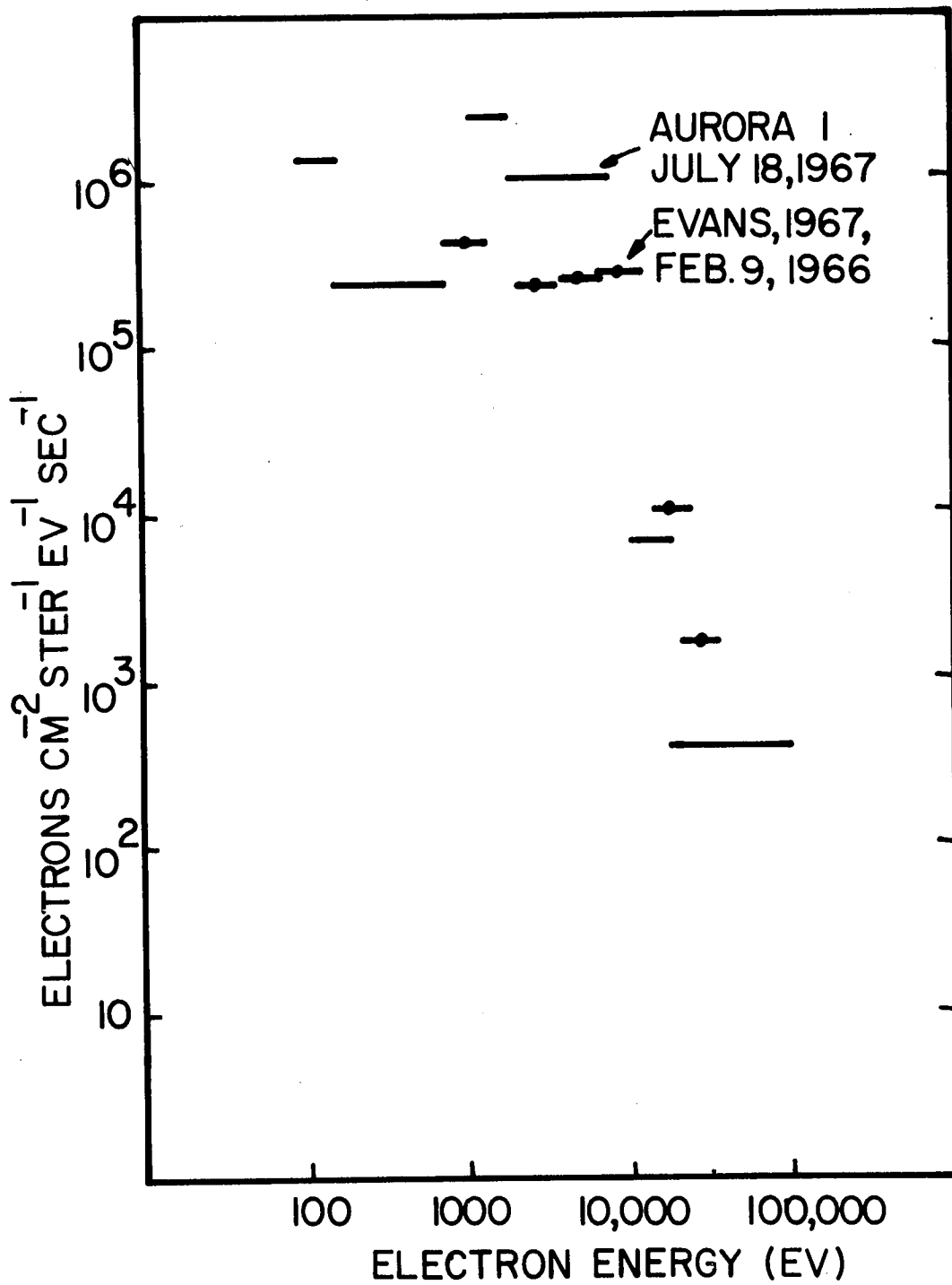


FIGURE 47

# PERTURBED NEUTRAL SHEET $\bar{B}$ FIELD

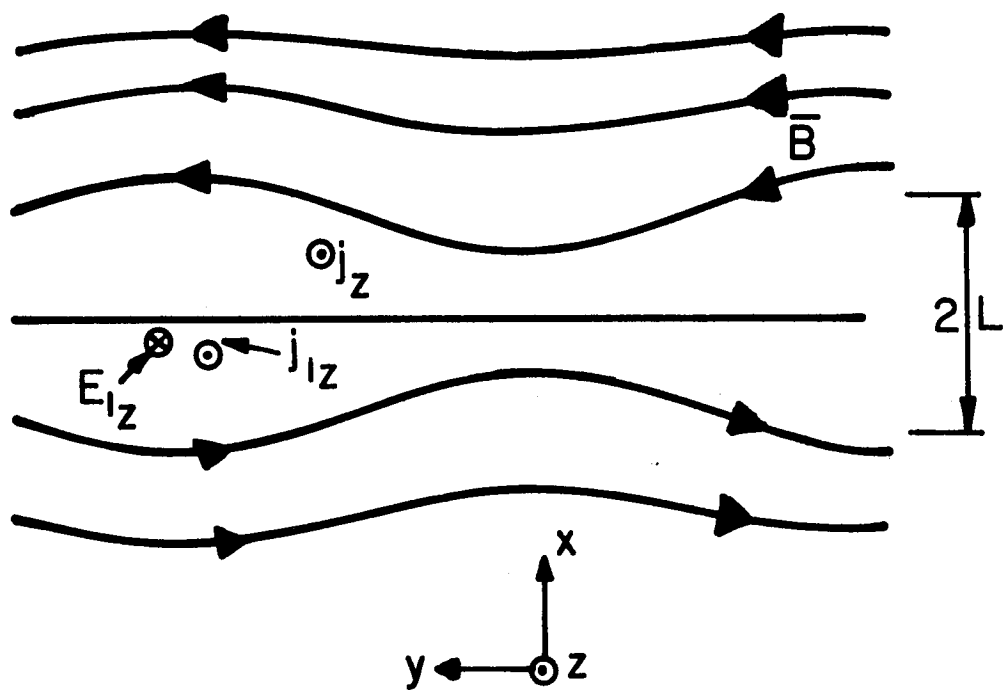


FIGURE 48



## NEUTRAL SHEET ELECTRON TRAJECTORIES

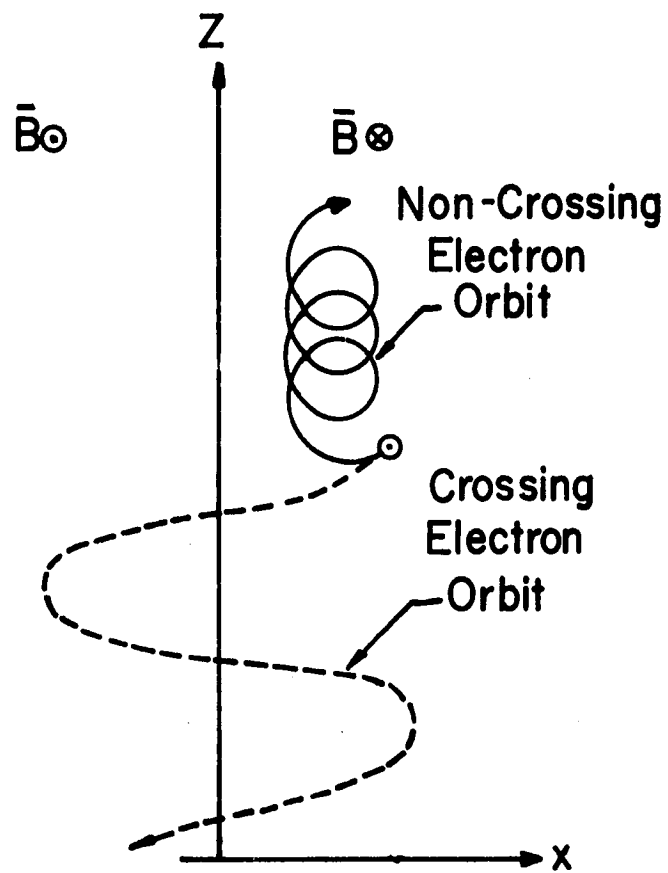
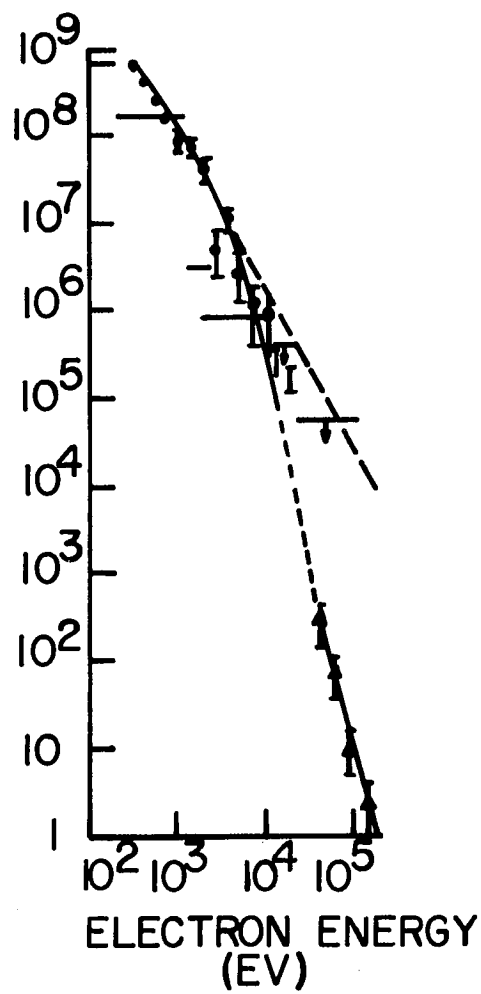


FIGURE 49

ELECTRONS/CM<sup>2</sup> KEV SEC (MONTGOMERY)  
 ELECTRONS/CM<sup>2</sup> STER KEV SEC (AURORA I)



AURORA I    - , -  
 MONTGOMERY    , • , ▲

FIGURE 50